Automated Objective Identification of Occluded Sectors in Midlatitude Cyclones: Method and Some Climatological Applications

Poushali Ghosh

A Thesis submitted in partial fulfillment of

the requirements for the degree of

Master of Science

(Atmospheric and Oceanic Sciences)

at the

University of Wisconsin-Madison

May 2023

Abstract

Automated Objective Identification of Occluded Sectors in Midlatitude Cyclones: Method and Some Climatological Applications

by Poushali Ghosh

A novel automated scheme for identifying occluded mid-latitude cyclones from gridded data sets is described and employed to construct a limited climatology of such storms as well as composites of their thermodynamic and kinematic structures. This scheme is also utilized to construct composite cross-sections of the cloud and precipitation distributions characteristic of occluded mid-latitude cyclones. The climatologies are derived from 11 years of MERRA-2 data and hydrometeor retrievals provided by CloudSat and CALIPSO. Differences between Northern Hemisphere (NH) occlusions and Southern Hemisphere (SH) were revealed in each composite category. Northern Hemisphere occlusions are most frequent in boreal winter (DJF) and are found poleward of the mean tropopause-level jets in both the Atlantic and Pacific basins. In the Southern Hemisphere, however, occlusions are most frequent during austral autumn (MAM) and are almost never found equatorward of 40°S. NH occluded sectors also exhibited wider and deeper hydrometeor structures than their SH counterparts, but with lesser hydrometeor frequency magnitudes than the SH structures. When compositing the hydrometeor structures across all occluded thermal ridges globally and comparing them to the distributions across associated frontal boundaries, the maximum in hydrometeors falls indubitably within the occluded sector, divorced from the surface occluded front.

Using the identification scheme, occlusions are stratified based on the maximum value of equivalent potential temperature (θ_e) at 700 hPa in their characteristic occluded thermal ridges. Composites of six groups of occlusions, based upon this distinction, are constructed for each hemisphere. The composites reveal notable differences in the thermodynamic structures among these 6 groups with more poleward (lower θ_e) storms exhibiting shallower, less developed thermal structures as compared to their lower-latitude (higher θ_e) counterparts. These differences are attended by contrasts in the intensity of upward vertical motions in the occluded sectors of the various composite storms, implying that "warmer" storms are associated with greater latent heat release than "colder" storms. This claim is reinforced by the positive correlation between hydrometeor frequency and 700 hPa maximum θ_e, until a threshold is reached. For very large values of 700 hPa maximum θ_e, hydrometeors tend to occur less frequently in NH occluded sectors and reach in asymptote in SH occluded sectors. Despite this contradiction, the coincident differences between "cold" and "warm" storms provide further evidence of the fundamental importance of latent heat release to the development of occluded thermal structures. The inconsistency seen between the supposed latent heat release trends in the composites and climatological hydrometeor frequency of occurrence suggests a nonlinear relationship between the two, which warrants further investigation.

Acknowledgements

First and foremost, I would like to express immense gratitude to my advisor and great friend, Jon Martin. Thank you for the endless support and encouragement in all realms of life. You are a fountain of knowledge (though, sometimes random and useless) and a profound example of what it means to love your science and have excitement for your profession, but only within the context of a well-balanced life. You are always ready to be a sounding board, a listening ear, a (metaphorical) punching bag or whatever resource your students may need. Whether it's professional discourse, a deep philosophical discussion, or constantly teasing each other about any and everything, a conversation with you is always time well spent. Also, thank you for going out on a limb and giving me the opportunity to join your lab after meeting for 20 minutes in Boston. I could not have imagined a better research position and place to grow as a scientist than in this department under your tutelage. I am looking forward to the many conversations, professional work and Arnold Palmers that are undoubtedly in our future!

To my great friend, Fuadh – I would not have gotten through these three years of graduate school without your support and companionship. Thank you for sticking by my side (even through the hangry moments), cheering me on, and always reminding me that I can do anything, even when I wanted to quit. Even from 1000 miles away, you were my support system. The countless late-night fast food runs, COVID movie/game nights, and vent sessions were my sustenance to get through an MS degree during such a rough time. Also, thank you for being my secret proofreader. I probably owe a lot of my grades to your keen eye and intelligent mind. I know it wasn't easy, but I am grateful for your patience and continued friendship.

To the Martonian lab (Patrick, Libby, Jessi and Ian), peers and pals – Thank you for making these past three years such a great experience. Though grad school is crazy stressful, we went through the trials and tribulations together and for that I am grateful. Our laughs, inside jokes, and lunch dates made coming to work every day so much fun.

To Patrick, especially, I genuinely don't think I could have gotten to this point without your friendship. I do mean this literally, because I would still be stuck at Meineke with no brakes or on Google scholar trying to find half of my sources for this thesis without you.

To the members of my committee, Dr. Angela Rowe and Dr. Tristan L'Ecuyer, thank you for your wise guidance through the AP and thesis writing process! Also, I can't be more grateful for your patience with me constantly moving deadlines further and being too optimistic because I kept forgetting how much TA-ing takes over your life during the semester. Also, thank you to the faculty and staff of the AOS department for all they did to make my experience here as great as it was, even through a tough 2 years in COVID lockdown.

And finally, to my parents, Asim and Chhanda – Your continued support throughout my academic endeavours is the foundational reason why I was able to make it to this point in my career. Working towards not only the first college degree, but also the first graduate degree in our family has been a privilege and an honor that I will never take for granted. I am incredibly grateful for the sacrifices that you've made in immigrating to this country and trying to ensure Dada and I could succeed to the best of our ability. Thank you.

Funding for this project was provided by the NASA CloudSat – CALIPSO recompete grant #80NSSC20K0085

Contents

List of Figures

List of Tables

Abbreviations

NCM	**N**orwegian **C**yclone **M**odel
OTR	**O**ccluded **T**hermal **R**idge
TROWAL	**TRO**ugh of **W**arm air **AL**oft
ETCs	**E**xtra**T**ropical **C**yclones
PV	**P**otential **V**orticity
SLP	**S**ea **L**evel **P**ressure
LHR	**L**atent **H**eat **R**elease
CPR	**C**loud **P**rofiling **R**adar
CALIPSO	**C**loud**A**erosol **L**idar **I**nfrared **P**athfinder **S**atellite **O**bservations

Chapter 1

Introduction

In their conceptual model of the mid-latitude cyclone, Bjerknes and Solberg (1922) were the first to suggest a relationship between the three-dimensional (3-D) thermal structure of the storm and its associated distribution of clouds and precipitation. The model, which has come to be known as the Norwegian Cyclone Model (NCM), described how the amplification of the nascent cyclone distorted the polar front, the globe-girdling boundary separating polar air to the north from the tropical air to the south into the cold and warm fronts of the storm structure. The so-called warm sector, a region of homogeneously warm air between the two fronts, extended downward to the surface. The thermal evolution of such cyclones involves changes in both the vigor of the individual frontal zones and in their orientation with respect to one another. The dynamical processes that control this evolution are also responsible for producing the secondary circulations to which the characteristic cloud and precipitation distribution in cyclones - linear bands of varying

widths along the cold and warm fronts and a cloud head poleward and westward of the storm center - can be accurately attributed.

Namias (1939) was among the first to examine the 3D airflow through cyclones and relate it to the attendant distribution of clouds and precipitation. He identified an ascending airstream, originating in the warm sector boundary layer, that bifurcated into two separate streams – one turning cyclonically to the west and the other turning anticyclonically to the east. More recent studies by Browning and Harrold (1969), Harrold(1973), Carlson (1980), Young et al. (1987) and Browning (1990) have christened the latter as the warm conveyor belt. This feature has garnered considerable research attention in the ensuing 30 years (e.g., Wernli, 1997; Wernli and Davies, 1997; Eckhardt et al., 2004; Madonna et al., 2014; Martinez-Alvarado, 2014;Schäfler and Harnisch, 2015;Berman et al., 2019). The cyclonically turning airstream has also been noted by Atkinson and Smithson (1974) as well as Iskendarian (1988), Kurz (1988), Mass and Schultz (1993), Schultz and Mass (1993) and Reed et al. (1994).

A notable element of the post-mature phase of the cyclone life cycle, with a bearing on these various airstreams, is the process of occlusion first conceived by Tor Bergeron (Jewell 1981). Among the structural changes that characterize the occluded stage are the adoption of an increasingly equivalent barotropic structure in the vertical as well as the development of a lower tropospheric thermal ridge connecting the sea level pressure (SLP) minimum to the peak of the warm sector (Saucier, 1955; Wallace and Hobbs, 1977; Schultz and Mass, 1993; Martin, 1998a,b; 1999a,b; Posselt and Martin, 2004; Schultz and

Vaughan,2011). According to the NCM, the air occupying the thermal ridge originated in the surface warm sector and was forced to ascend by the intersection of the cold and warm fronts as the cyclone occludes. The resulting structure consists of an axis of maximum potential (θ) or equivalent potential (θ_e) temperature, in both horizontal and vertical cross sections, embedded within a region of reduced static stability between two significant baroclinic zones, as depicted in Fig. 1.1. Despite the sometimes fierce debate regarding the mechanisms that might operate to produce it (e.g. Schultz and Mass, 1993; Stoelinga et al., 2002; Schultz and Vaughan, 2011), there is little disagreement that such a configuration represents the canonical thermal structure of a warm-occluded cyclone.

A more fully 3-D representation of the warm-occluded thermal structure was developed in a series of papers over the course of more than a decade by scientists at the Canadian Meteorological Service (Crocker et al., 1947; Godson, 1951; Penner, 1955; Galloway, 1958,1960). These studies noted the ubiquity of a westward slope to the crests of the thermal wave at successive heights in occluded cyclones. Penner (1955) referred to this "sloping valley of tropical air", as it had been previously described by Godson (1951), as the TROWAL (TROugh of Warm air ALoft). Borrowing terminology from the NCM, the TROWAL essentially marks the 3-D sloping intersection of the upper cold frontal portion of the warm occlusion with the warm frontal zone. The observation that the cloudiness and precipitation characteristic of the occluded sector of the cyclone bore a closer correspondence to the TROWAL position than to the weak surface warm-occluded front led the Canadians to regard the TROWAL as the essential structural feature of a warm-occluded cyclone. Consistent with the definition given by Penner (1955) and the

description given by Godson (1951), the TROWAL can be approximately located either as a ridge of high θ, θ_e or 1000:500 hPa thickness on a horizontal cross section, and more precisely as a 3-D sloping canyon in an isosurface of θ_e as shown in Martin (1998a, 1999a). In fact, unlike cold and warm frontal analyses that are drawn as lines on a single isobaric or geometric height surface, because occlusions are so strongly tied to the position of the sloping TROWAL, identifying them is inherently a 3D problem. A schematic illustrating the TROWAL conceptual model is given in Fig. 1.2.

Compelling evidence supporting these earlier observational findings comes from a number of a more recent fine scale numerical modeling studies of occluded cyclones (Schultz and Mass, 1993; Reed et al., 1994; Martin, 1998 a,b) that have illustrated the structure and thermal evolution of, and airflow through, the occluded sector. These studies have identified a coherent airstream, originating in the warm sector boundary layer, that ascends cyclonically in the occluded sector of the cyclone. Martin (1998b,1999a), noting a spatial relationship between the path taken by this airstream and the TROWAL in various cases, referred to this airflow as the "trowal airstream". By considering the insightful along- and across-isentrope partition of the Hoskins et al. (1978) Q-vector first described by Keyser et al. (1992), Martin (1999a,b) provided a dynamical explanation of the relationship between the development of the characteristic thermal structure in the occluded sector of cyclones and the associated ascent that supports this airstream. Consistent with forced ascent in a nearly saturated environment, the developing occluded thermal ridge is often associated with substantial latent heat release (LHR).

Martin (1998a) noted that some occluded cyclones are associated with a characteristic tropopause-level potential vorticity (PV) structure consisting of an isolated, low-latitude high-PV feature that is connected to a high-latitude reservoir of high PV by a thin filament of high PV - a structure he termed the "treble clef" (Fig. 1.3). Given the relationship between tropopause-level PV and the thermal structure in the underlying troposphere (Hoskins et al., 1985), the horizontal juxtaposition of two upper-level positive PV anomalies of unequal magnitude, separated by a relative minimum in PV (such as along line A-A' in Fig. 1.3a) depicts the canonical warm-occluded thermal structure (Fig. 1.3b). From the perspective of the NCM, the sloping warm column beneath the upper-tropospheric PV minimum in Fig. 1.3b represents warm sector boundary layer air that has been lifted during the occlusion process. In three dimensions, the warm axis identifies the position of the TROWAL which, as mentioned earlier, tends to be a focus for precipitation production in the occluded sector of cyclones. Thus, the clouds and precipitation in that portion of the storm are often nearly coincident with an upper-tropospheric PV minimum. The strong connection between the morphology of the upper-tropospheric PV and the underlying occluded thermal structure, coupled with the known diabatic influence on vertical PV redistribution (e.g., Eliassen and Kleinschmidt, 1957; Hoskins et al., 1985; Raymond, 1992), provided a convenient framework for Posselt and Martin (2004) to investigate the influence of LHR on the formation of an occluded thermal structure.

Comparing full physics and "no LHR" MM5 simulations of a major winter storm, Posselt

and Martin (2004) found that the former depicted the canonical, troposphere-deep, warm-occluded structure while the latter produced only a shallow, poorly developed one. Their analysis showed that direct dilution of a local, upper-tropospheric PV maximum by mid-tropospheric LHR initiated formation of a local, upper-tropospheric PV minimum, or low PV tongue, to the northwest of the surface cyclone center. The production of this PV minimum initiated a cutting off of the upper-tropospheric PV anomaly associated with the surface development. The associated upper-tropospheric circulation then forced the advection of low ($<$ 1 PVU) values of PV into the developing PV trough. This combination of kinematic and diabatic processes acted to produce both the tropopause PV treble clef as well as the underlying warm-occluded thermal structure in the full physics simulation. In contrast, though an adiabatic kinematic tendency for production of a treble clef PV morphology also operated in the "no LHR" simulation, the resulting PV and thermal structures were weaker and slower to evolve than those produced in the full physics simulation. Thus, the authors suggested that LHR plays an important role in the production of the characteristic occluded thermal structures observed in nature.

A number of methods have been proposed for objective identification of cold and warm fronts (e.g. Hewson, 1998; Hewson and Titley, 2010; Berry et al., 2011; Simmonds et al., 2012; Schemm et al., 2018 ; Thomas and Schultz, 2019a,b and references therein). Naud et al. (2012;2015;2018; Schultz, 2018) employed satellite-based radar and lidar profiles (CloudSat, Stephens et al., 2002; CALIPSO, Winker et al.,2009) to explore the cloud and precipitation distributions associated with objectively identified cold and warm fronts and how these distributions relate to the larger scale environment. Although

occlusions are a well-studied meteorological phenomenon (e.g. Schultz and Mass, 1993; Martin, 1998a,b, 1999a,b; Stoelinga et al., 2002; Posselt and Martin, 2004; Schultz and Vaughan, 2011), there is no automated method of occlusion detection. Consequently, it has not been possible to consider the global distribution of occluded cyclones, their composite thermodynamic and kinematic structures or explore the cloud and precipitation distributions of a very large number of occluded sectors observed in a wide range of locations and environmental conditions.

Extratropical cyclones are responsible for the largest share of the global redistribution of heat required to offset latitudinal differences in radiative transfer. Since the occluded sectors of these storms are known to be regions of significant moisture convergence and attendant LHR, occluded cyclones provide a key physical link in the global energy and water cycles. As we peer into the future with sophisticated global climate models, it is essential that these models faithfully reproduce increasingly detailed aspects of the life cycles of the individual weather systems involved in these global cycles. This thesis will lay the foundation for assessment of the climatological characteristics of occluded mid-latitude cyclones and attendant evaluation of the skill with which a global climate model can reproduce the canonical occluded structure and precipitation characteristics.

Central to the present study will be the description of an automated scheme that identifies the occluded sectors of cyclones from gridded reanalyses and/or climate model output. The method will then be employed to construct the first global survey of occluded cyclones. In Chapter 2, we describe details of the objective identification scheme. Some

results of its application to eleven years of MERRA-2 reanalysis data are presented in Chapter 3. Included in this presentation are a limited global climatology as well as composites of the thermal structure and vertical motion distributions of wintertime occluded cyclones observed in both the Northern (NH) and Southern Hemispheres (SH) over 11 recent winters. Also included in the present study is the application of the objective identification scheme outlined in Chapter 2 to CloudSat-CALIPSO retrievals to explore the cloud and precipitation distributions across the TROWAL region and associated frontal boundaries. The results of this analysis are presented in Chapter 6. A discussion of the results and an outline of future work to be undertaken are offered in Chapter 6.

Chapter 2

Data and Methods

2.1 Data

In the automated methodology to be described, the analysis uses 11 years of data from the second iteration of NASA's Modern-Era Retrospective analysis for Research and Application (MERRA-2) gridded reanalysis output (Gelaro et al., 2017) spanning September 2006 – August 2017. In particular, air temperature along with SLP, geopotential height (Φ), specific humidity and vertical velocity (ω) are utilized to identify occluded extratropical cyclones and subsequently portray aspects of their structure and evolution. The MERRA-2 data is available on a $0.625^\circ \times 0.5^\circ$ horizontal grid with 42 vertical levels spanning from 1000 hPa to 3 hPa. For purposes of evaluation of the automated identification method to be described later, and to ensure it is reliable across different data sets and grid resolutions, the study also employed the NCEP Climate Forecast System Reanalysis

(CFSR) (Saha et al., 2010) data set, from which the same variables were available at 64 vertical levels with 38 km spatial resolution.

2.2 Objective Identification Parameter

Since occlusion represents the beginning of the post-mature phase of a cyclone's life cycle, many (though not all) storms that occlude do so near their peak intensities. This study utilizes the methodology and parameters of Naud et al. (2023), which considers the time of peak intensity as the time at which either the central SLP reaches a minimum or when the pressure depth has reached a maximum, then choosing whichever phenomenon occurs first. Pressure depth is defined as the difference between the outermost closed SLP contour and the central pressure in Polly and Rossow (2016).

An occluded thermal ridge serves as a two-dimensional (2-D) proxy for the 3-D TROWAL, the essential structural feature of the occluded sector. Therefore, it can be identified using any of several thermodynamic variables, including potential temperature (θ), equivalent potential temperature (θ_e) and 1000-500 hPa thickness, according to Naud et al. (2023). Since the occluded thermal ridge routinely extends through a substantial depth of the troposphere, 1000-500 hPa thickness, denoted as Φ', was chosen as the focal variable for the objective identification scheme as it best captures the full 3-D structure of the feature. Naud et al. (2023) found that elements of the analysis method were found to be occasionally noisy at the high native resolution of the MERRA-2 data. This fact, coupled with a desire to construct an automated detection method that could eventually

be applied to lower resolution output from global climate models, compelled coarsening the native resolution of the MERRA-2 data by a factor of 2. Hence, the thickness fields were processed on a $1.25^\circ \times 1^\circ$ horizontal grid. Objective identification of the occluded thickness ridge (OTR) is based upon examination of the functional form of the divergence of the unit vector in the direction of $\nabla\Phi'$, given by,

$$\hat{n} = \frac{\nabla\Phi'}{|\nabla\Phi'|} \tag{2.1}$$

An example field of Φ' and $\hat{n}$ for an occluded cyclone over the British Isles at 0600 UTC 7 January 2008 is shown in Fig. 2.1a. The divergence of 2.1, $(\nabla \cdot \hat{n})$, takes the form,

$$\nabla \cdot \hat{n} = \nabla \cdot \frac{\nabla\Phi'}{|\nabla\Phi'|} = \frac{\nabla^2\Phi'|\nabla\Phi'| - \nabla\Phi' \cdot \nabla|\nabla\Phi'|}{|\nabla\Phi'|^2} \tag{2.2}$$

using the quotient rule. The sign of the resulting expression is negative in the presence of a thickness ridge but, as shown in Fig. 2.1b, it is also negative in many other locations unrelated to the OTR. In order to highlight those areas of $(\nabla \cdot \hat{n}\ )$ that are also associated with the largest thermal contrasts, the final form of the finding function (referred to as $\boldsymbol{F}$) is weighted by the magnitude of the thickness gradient.

$$\mathbf{F} = (\nabla \cdot \hat{\mathbf{n}})|\nabla\boldsymbol{\Phi}'| = \boldsymbol{\nabla^2\Phi'} - \hat{\mathbf{n}} \cdot \nabla|\nabla\boldsymbol{\Phi}'| \tag{2.3}$$

From this expression it is clear that $\boldsymbol{F}$ highlights regions where the Laplacian (i.e., divergence of the gradient) of the thickness field is substantial and/or where there is substantial advection of thickness gradient magnitude by the unit vector. In the vicinity of a thickness ridge, bounded by thickness contrasts on either flank, both of these terms contribute to $\boldsymbol{F} < 0$. Unfiltered fields of $\boldsymbol{F}$ contain small-scale features that can cloud the intended thickness ridge identification results. To avoid such obfuscation, only values of $\boldsymbol{F} < -1 \times 10^{-9}$ m-1 ($\boldsymbol{F}_{max}$) are considered and a 9-point smoother is applied to avoid excessive noise in the output. The example shown in Fig. 2.1c is illustrative of the efficacy of $\boldsymbol{F}$ as the noisiness of the raw ($\nabla \cdot \hat{n}$) field in Fig. 2.1b is rendered considerably more coherent and interpretable. The main feature is an extended region of $\boldsymbol{F} < \boldsymbol{F}_{max}$, some of which clearly coincides with the axis of the 1000-500 hPa thickness ridge, while the other portion stretching from southern Germany across eastern France appears just ahead of the cold frontal thickness gradient. The vertical cross-section along B-B' in Fig. 2.1c cuts through the section of the $\boldsymbol{F}$ field that elongates along the thickness ridge from the low-pressure center into the warm sector.

That cross-section (Fig. 2.1d) illustrates the canonical warm occluded thermal structure with an axis of maximum θ_e between two baroclinic zones, the warm and cold fronts, sloping poleward with height. Martin (2006) characterizes the location at which the axis of maximum θ_e intersects with the ground as the position of the surface warm occluded front. As is generally the case, a plume of maximum vertical motion associated with the main updraft of the storm appears to be better collocated with the TROWAL than with the surface occluded front. The isobaric topography of the 300 K moist isentrope

from this case is shown in Fig. 2.1e. This particular isentrope was chosen as it lies near the warm edge of both the cold and warm fronts in the occluded thermal structure. The TROWAL, indicated by the bold dashed line, clearly coincides with the northern portion of the $\boldsymbol{F} < \boldsymbol{F}_{max}$ region. However, by its nature as the 3D sloping intersection of the cold and warm fronts of the occluded thermal structure, the TROWAL is never perfectly represented by analysis at a single level or in a single layer. Despite the fact that there is no objective standard against which the automated identification method could be checked, elements of the canonical occluded thermal structure are easy to identify in gridded reanalysis data sets, as demonstrated in the example illustrated in Fig. 2.1. Therefore, the evaluation of $\boldsymbol{F}$ consisted of interrogating every feature the parameter flagged as occluded in the north Atlantic (20°N - 80°N, 90°W - 40°E) and north Pacific basins (10°N – 80°N, 130°E - 110°W) during the winter seasons of 2007-08 and 2008-09 against those canonical elements. This process was conducted using Unidata's GEneral Meteorology PAcKage (GEMPAK) visualization software suite (Unidata, 2019). Table 1 tabulates the relevant GEMPAK input variables used to display each field. Once an OTR was recognized, the analysis steps depicted in Fig. 2.1a-e were reconstructed at each 6h time step at which the feature was identified to assess $\boldsymbol{F}$'s efficacy throughout the full OTR life cycle. In order to develop a robust, data set-independent technique, an element of this testing was employment of a collection of input data sets including NCEP-CFSR as well as NCEP-NCAR reanalysis data (Kalnay et al., 1996). An example of a direct comparison of the depiction of an occlusion identification by both the MERRA-2 and CFSR data sets (of which many were considered) is shown in Fig. 2.1f. Although the fine

spatial resolution of CFSR data allowed for the detection of a greater number of grid cells where $\boldsymbol{F} < \boldsymbol{F}_{max}$ than the coarser MERRA-2 data, it can be seen that the identification parameter clearly highlights the position and orientation of an occluded thermal ridge.

2.3 The cluster tracking method

Automating the use of the $\boldsymbol{F}$ parameter presents the unique opportunity to identify all extratropical cyclones undergoing occlusion as well as construct composites of elements of the thermodynamic and kinematic structure of the occluded sector. Given its versatility, $\boldsymbol{F}$ can be employed using output from any gridded data set, such as those produced by standard numerical weather prediction (NWP) forecast models and/or GCMs. Naud et al. (2010) used GISS Model E (Schmidt et al., 2006) and NCEP-DOE (Kanamitsu et al., 2002) data to track and identify storms with a method similar to Bauer and Del Genio (2006) and Bauer et al. (2016)'s NASA Modeling, Analysis, and Prediction (MAP) Climatology of Mid-Latitude Storm area (MCMS) algorithm. The MCMS algorithm searches for local minima in SLP and tracks them through time. Qualifying cyclones must not travel more than 720 km in any 6h interval of their life cycles but must travel at least 700 km, exist for at least 24 hours, and reach a minimum SLP of less than 1010 hPa during their life cycles. However, Naud et al. (2010) only utilized this technique for observing the properties of the cold and warm fronts associated with detected cyclones, and subsequently warm frontal (Naud et al., 2012) and cold frontal precipitation structures (Naud et al., 2015). The latter studies upgraded the spatial and temporal resolution used to construct the cyclone database to MERRA (Rienecker et al., 2011) at

0.5°×0.667° for 4 years from the coarser 2.5°×2.5° 2-year NCEP-DOE reanalysis used in (2010). In response to a critique from Schultz (2018) that requested the removal of "contaminating" occluded fronts from Naud et al. (2015), Naud et al. (2018) expanded the use of their 2010;2012;2015 cyclone database to focus on non-frontal properties of their identified cyclones. The present study utilizes this most recently updated cyclone database for the automated detection of OTRs.

The full track of each identified storm in the cyclone database was considered and divided into individual snapshots, depicting the instantaneous state of the cyclone every 6 hours. Automating the use of the OTR finding function,$\boldsymbol{F}$, to identify cyclones that are occluded involves several assessments at each 6h snapshot for candidate cyclones. First, the individual cyclone tracks have to be identified. Figure 2.2a provides an example of the track of a sample cyclone that occurred over the northeast Atlantic in early January 2008 (the analysis in Fig. 2.1 represents one 6h snapshot of this storm). The cyclone's time of peak intensity is clearly indicated as is its position every 6h from 0600 UTC 6 January to 1800 UTC 8 January. To ensure computational efficiency, a limited area stretching from -10° to +20° longitude and ±20° latitude from the storm center, is then considered at each 6h analysis time. MERRA-2 temperature, SLP, 1000:500 hPa thickness, θ_e and vertical velocity fields were collected within this limited area and $\boldsymbol{F}$ was calculated at each grid point.

The finding function is then applied within this area, flagging grid points at which $\boldsymbol{F} < \boldsymbol{F}_{max}$. Corresponding points for the example time previously considered (Fig. 2.1) are

shown as the red crosses in Fig. 2.1f. The collection of such points, in the prescribed limited area, for 1200 UTC 6 January 2008 are indicated by the black and red crosses in Fig. 2.2b (and similarly for other times in Figs. 2.2c-e). These points are referred to as qualifying grid points. Any such grid points are given no further consideration if the standard deviation of the surface elevation at the object grid point, and its 4 adjacent points is greater than 300 m, $\mathrm{STDSurf}_{max}$. Such points in the example storm are indicated with a blue triangle in Figs. 2.2b-e. Remaining grid points meeting the threshold in $\boldsymbol{F}$ qualify for further consideration only when at least 8 (N_{min}) contiguous neighbors constitute a cluster and the mean longitude of that cluster is located to the east of the SLP minimum (note 12 such grid points in Fig. 2.2b). Such qualifying clusters have a black diamond surrounding a black cross in Figs. 2.2b-e. When a 6h snapshot possesses a qualifying cluster, it is said to be an occlusion identification. In order to have identified an occluded ETC, qualifying clusters must at least partially overlap in a cyclone-relative grid at no less than two consecutive 6h times as illustrated in Fig. 2.3 for the 6-7 January 2008 cyclone. This confirms that the cyclone center and the qualifying cluster are moving in tandem. Additionally, the first appearance of a qualifying cluster in a cyclone's track history (e.g., the cluster at 1200 UTC 6 January in Fig. 2.2b) must have been located within a distance of 300 km (D_{max}) of the cyclone center in order for the cyclone to qualify as an occluded ETC and be included in the subsequent composite analyses. Finally, if a cluster is identified (1) only once during a cyclone's life cycle, (2) at several non-consecutive 6h time steps, or (3) in a consecutive series that ends before the cyclone reaches its peak intensity, that storm and its cluster are not considered

in any subsequent analyses. These various empirically-derived disqualifications reflect the intentionally conservative nature of the scheme which is designed to minimize false identification. Though such a design may overlook some weak occlusions, given the large number of candidate storms, the slightly conservative approach adopted here is unlikely to lead to mischaracterization of the global climatology or composite structures. This detection method identified 26,351 6h snapshots of cyclones classified as occluded throughout the 2006-2017 analysis period across the globe and all seasons.

This procedure can be applied to any gridded data sets with only slight modifications made based upon horizontal grid spacing. Resolution-based adjustment made to several of the parameters involved in the method are summarized in Table 2.1. The parameters $\boldsymbol{F}_{max}$, N_{min}, and $STDSurf_{max}$ were determined to exhibit a linear dependence on grid resolution. D_{max} is an absolute distance and, therefore, its magnitude remains the same for all three grid spacings. Use of $\boldsymbol{F}$ paired with these synoptically-informed qualifications has proven to be satisfactory as the composite results in Chapter 3 will unambiguously testify.

2.4 Constructing composite vertical cross-sections

Employing each 6h occlusion identification, the following procedure was employed to build composite vertical cross-sections through these features. The procedure is best described using a schematic version (Fig. 2.4) of a single 6h identification period (such as those shown in Figs. 2.2b-e). The procedure takes advantage of the fact that the occluded

thermal ridge can be accurately portrayed by a number of alternatives to 1000-500 hPa thickness, including 700 hPa θ_e . It proceeds by first calculating a regression line (in latitude and longitude) through the cluster of the grid points constituting a qualifying cluster (blue crosses in Fig. 2.4). That line, the solid gray line in Fig. 2.4, represents the thickness ridge axis and its longitudinal range is bounded by the dashed red lines. At the median longitude of the thickness ridge axis, a transect is drawn perpendicular to the axis. Finally, the thickness ridge axis line is slid along the transect line until it reaches the coincident 700 hPa θ_e maximum. Synoptic experience suggests that the OTR rarely extends above 350 hPa. Consequently, though a number of other choices might also serve the purpose, 700 hPa represents a mid-tropospheric level (free from excessive boundary layer influences) by which to normalize the position of the axis of the thermal ridge. The intersection of the transect line and the adjusted thickness ridge axis is then the midpoint of a 3000 km long transect line along which any variable (θ_e ,ω, T, etc.) may be obtained. In order to produce composites of the vertical structure through the OTR, each such transect is preserved and then they are all averaged together to produce the composite vertical cross-section of the given variable. Because the middle of each transect is, by construction, coincident with the maximum 700 hPa θ_e for that particular cross-section, it is possible to create separate composite occluded structures based upon ranges of their maximum 700 hPa θ_e values.

Chapter 3

Some Climatological Applications

Because subsequent work will employ observations made with CloudSat/CALIPSO data, application of the automated method just described has been applied to 11 years (1 September 2006 – 31 August 2017) of MERRA-2 reanalyses, corresponding to the CloudSat/CALIPSO era. In that period 6,147 individual cyclone tracks (2,529 in the NH and 3,618 in the SH) have been identified from which 26,351 6-hrly snapshots (as described in Section 2.3) have resulted in occlusion identifications. Given the standard deviation of surface elevation criteria previously described (STDSurf_{max}), the analysis focused only on those identifications that were made over the oceans. Thus, a total of 22,329 identifications (8,741 in the NH and 13,588 in the SH) were included in the analysis. In the next section descriptions of some elements of these occlusion identifications are presented.

3.1 Global distribution of occluded cyclones

Employing the automated identification method just described, a global distribution of occluded identifications can be constructed. Figure 3.1a shows the NH winter (DJF) cumulative distribution of 6h occluded identifications over the eleven year period and reveals that, in the north Pacific, occluded cyclones populate the basin poleward of the mean jet with distinct maxima in the southern Sea of Okhotsk, east of the Kamchatka peninsula, and in the Gulf of Alaska. Wintertime occlusions in the north Atlantic basin are concentrated in a strip running from the mouth of the Labrador Sea to the southeast coast of Greenland. Further analysis (not shown) revealed that the robust maximum in occluded identifications near the tip of Greenland in Fig. 3.1a is a function of a larger overall number of storms there and not an unusually large proportion of those storms occluding in that location. The two winter maxima regions harbor smaller numbers of occlusion identifications during the NH spring (MAM) (Fig. 3.1c). It is no surprise that identifications are considerably less common during the NH summer (JJA) while frequenting the same general locations (Fig. 3.1e). The number of occluded identifications quickly rebounds in NH autumn (SON) (Fig. 3.1g).

The distribution in the SH is different in many respects. The wintertime (JJA) distribution shows almost no occlusion identifications equatorward of 40°S (Fig. 3.1b). Despite the fact that a noted cyclogenesis maximum exists in the lee of the Andes during austral winter (Hoskins and Hodges, 2005), there is no coincident maximum in occluded identifications in the region in that season. Instead, cyclones in the lee of the Andes appear

to occlude more frequently in spring (Fig. 3.1d) and autumn (Fig 3.1f). Dual frequency maxima during winter appear along the Wilkes Land (120 °E) and Enderby Land (45°E) coasts of Antarctica. By spring (SON), occluded identifications are less common everywhere with the greatest decreases observed in the longitudes straddling South America (Fig. 3.1d). The distribution thins further by austral summer (DJF) (Fig. 3.1f). With a resurgence of occluded identifications at the locations of the winter maxima and a general increase elsewhere, autumn (MAM) is the season with the greatest number of identifications in the SH (Fig. 3.1h). Thus, the hemispheres have notably different seasonal cycles in occluded identifications.

3.2 Structure of composite wintertime occlusions

3.2.1 Composite Northern Hemisphere wintertime occlusions

Further detail regarding the wintertime distribution of NH occlusion identifications is afforded by stratifying them by the value of the 700 hPa θ_e maximum along the thickness ridge axis. The goal was to partition the total number of identifications into as many groups as possible whose composite structures were meaningfully different from one another while keeping the number of identifications in each group large enough to ensure statistical robustness. Such a compromise was achieved by considering 6 groups each containing 372 occluded ETCs. Figure 3.2 shows the number of occluded identifications in 6 bins constructed such that each bin contains the same fraction of the total number of identifications in the 2006-2017 analysis period. Two-thirds of all the identifications

had 700 hPa θ_e maxima in the range of ∼293K to 313 K. The geographic distribution from each of these 6 bins is shown in Fig. 3.3. Not surprisingly, stratification by 700 hPa θ_e maxima effectively separates sub-populations of identifications by latitude, with the lowest θ_e maxima occurring at high latitudes and vice versa. Bins II-IV (Figs. 3.3b-d) exhibit distributions of occluded identifications that are broadly consistent with the climatological positions of the Aleutian Low in the Pacific basin and the Icelandic Low in the Atlantic basin. In the two "warmest " bins (Figs. 3.3e-f), however, the occluded identifications in both basins notably recede equatorward from these centers.

Figure 3.4 presents the results of constructing composite vertical cross-sections of θ_e through each of these 6 groups of occlusion identifications. Recall from Fig. 3.4 that the 700 hPa θ_e maxima of those comprising Bin I range from 275K to 293 K. In this "coldest" bin, the OTR notably does not exhibit any vertical tilt (Fig. 3.4a), suggesting that these storms have a shallower and less developed occluded thermal structure than those occurring at lower latitudes. These identifications are associated with cyclones that appear to cluster near coastlines - especially around Kamchatka and southeast Greenland (Fig. 3.4a). This circumstance may influence their composite structure compared to those cyclones found farther out at sea. Both the cold and warm frontal portions of the composite occluded structure in Bin II (Fig. 3.4b) are better developed that those in Fig. 3.4a. The successively "warmer" composite occlusions (Fig. 3.4 c-f) exhibit increasingly robust cold and warm frontal structures as well as axes of maximum θ_e that tilt increasingly poleward, as in the canonical occluded thermal structure. Also notable in these last 4 composites is the burgeoning couplet of lower tropospheric cyclonic PV

(at the center of the cross-sections) along with its companion upper-tropospheric PV minimum. These features are physically linked to each other through the substantial mid-tropospheric LHR that characterizes the TROWAL in these "warmer" storms.

Further evidence of this connection is evident in the composite vertical motions in the vicinity of the OTRs of these different collections of occlusion identifications shown in Fig. 3.5. It is immediately apparent that the "warmer" identifications have stronger upward vertical motions within their OTRs and that their composite vertical motion plumes share the poleward tilt of their respective axes of maximum θ_e . The magnitude of ω is a function of the forcing for ascent modulated by the local static stability. As noted in reference to Fig.3.3, stratifying the identifications by 700 hPa θ_e maxima in their OTRs amounts to a sorting by latitude. Thus, the "warmer" (i.e., lower latitude) ones are consistently farther south over warmer SSTs and are therefore likely characterized by weaker stratification in their warm sectors prior to occlusion. Martin (1999a) showed that synoptic-scale forcing during the process of occlusion (namely, positive vorticity advection (PVA) by the thermal wind (Sutcliffe, 1947)) thrusts some portion of this warm sector air aloft into the TROWAL. Nearly all the occluded identifications shown in Fig. 3.3 occur in proximity to the Northern Hemisphere storm tracks (see Fig. 3.1a) which, by definition, are regions of maximum frequency of surface development. Since a fundamental synoptic-scale forcing for ascent in mid-latitude cyclogenetic environments is provided by PVA by the thermal wind (e.g. Sutcliffe, 1947; Trenberth, 1978; Hoskins et al. 1978; Hoskins, 1999; Martin 1999a,b), it is reasonable to conclude that the vast majority of occluded identifications shown in Fig. 3.3 occurred in regions where PVA by the thermal wind

was involved in development. We suggest that the robust differences in response to such forcing, as manifested in the notable differences in vertical motion, are at least partly, and perhaps largely, a function of the decreasingly stable stratification at lower latitudes.

3.2.2 Composite Southern Hemisphere wintertime occlusions

As in the preceding section, the wintertime distribution of occlusion identifications is divided into 6 groups with equal populations of 605 occluded SH ETCs based upon the value of the 700 hPa θ_e maximum along the thickness ridge axis. Figure 3.6 shows the number of occluded identifications in each of those 6 groups. Two-thirds of all the identifications had 700 hPa θ_e maxima in the range of ∼288K to 304 K, notably lower than the θ_e range of the equivalent fraction of NH occlusion identifications (Fig. 3.2). It should also be noted that the number of wintertime occluded identifications in the SH is nearly twice that of the NH during the same 11-year period (note the ordinate axis in Fig. 3.6 versus Fig. 3.2) and that the peak occurs at much lower θ_e in the SH. The geographic distribution of occlusions from each of these 6 bins is shown in Fig 3.7. As in the NH, the stratification by 700 hPa θ_e maximum primarily separates subpopulations of identifications by latitude. An exception to this general rule is suggested by the notable maxima of occlusion identifications east of Argentina that appears in Bin VI (Fig. 3.7f). This regional concentration of occluded ETCs suggests that the "warmest" events in the wintertime cyclogenesis maximum identified by Hoskins and Hodges (2005) are more likely to occlude than all others in that same region.

Figure 3.8 presents the composite vertical cross-sections of θ_e through each of the 6 groups

of SH occlusion identifications. As in the NH population, the "coldest" composite does not exhibit any vertical tilt (Fig. 3.8a). In fact, such a vertical tilt does not appear until the composites of Bin III (Fig. 3.8c) and then becomes more exaggerated in the successively "warmer" bins (Figs. 3.8d-f), as was the case for the NH composites. As in the "warmest" NH identifications, a relationship between expanding lower tropospheric cyclonic (negative) PV features and a companion upper-tropospheric PV maxima is clearly evident in Figs. 3.8c-f. Interestingly, even the "coldest" identifications are characterized by a lower tropospheric cyclonic PV maxima in the SH (Figs. 3.8 a-b). Another notable difference between the "warmest" SH composite occluded structures as compared to their NH counterparts is that the axis of maximum θ_e does not penetrate to the surface in the SH composites (e.g., θ_e = 288K in Fig. 3.8e and θ_e = 297K in Fig. 3.8f). Instead, it appears that their occluded thermal structures are found atop a shallow, potentially unstable boundary layer in which θ_e decreases with height to $\sim$ 950 hPa.

Finally, the composite vertical motions in the vicinity of the SH OTRs are shown in Fig. 3.9. Again, as in the NH, the "warmer" occlusions are associated with stronger upward vertical motions within their OTRs as well as gradually increasing poleward tilt. The same conjunction of synoptic-scale forcing and stratification presumed to be involved in shaping the NH composites likely also determines the characteristics of the SH vertical motion composites. In the face of this probable similarity, it is interesting to note that both the horizontal and vertical scales of the ascent in the SH composites are larger. Alternatively, the composite NH occluded sector vertical motions are both more

concentrated and more vigorous. Identification of the underlying physical factors that might account for this difference is the subject of ongoing research.

Chapter 4

CloudSat-CALIPSO Hydrometeor Retrievals

In April 2006, NASA's Jet Propulsion Laboratory launched and maneuvered CloudSat and Cloud Aerosol Lidar and Infrared Pathfinder Satellite Observations (CALIPSO) to join the Afternoon Constellation ("A-Train") in an effort to advance the understanding of cloud abundance, distribution, structure, and radiative properties through spaceborne observations. The troop of satellites that constitute the A-Train follows a helio-synchronous orbit approximately 705 km above the surface. The orbital mechanics of the A-Train allow for each of the satellites to view a location at 1:30 pm local time, providing plenty of sunlight to illuminate the scene. The Cloud Profiling Radar (CPR) aboard CloudSat provides radar products at millimeter-wavelengths (95 GHz), allowing it to observe smaller particles at a higher level of precision than ground-based centimeter-wavelength (3 GHz)

weather radars. Since a sizeable portion of the cloudiness and precipitation associated with the post-mature phase of midlatitude cyclones is found within the occluded sector, retrievals from the CPR and the Cloud-Aerosol Lidar with Orthogonal Polarization (CALIOP) aboard CALIPSO offer the unique opportunity to observe the hydrometeor structure within this region. An additional aspect of the detected cyclones in the Naud et al. (2018) database discussed in Chapter 2 is the established association of a CloudSat-CALIPSO orbit with each identification. The detection scheme ascertains if a CloudSat orbit could be found within 2500 km of the center of the identified cyclone and $\pm$ 3 hours of its detection. The CloudSat platform exited the A-Train in February 2018. Therefore, OTRs were detected throughout the 5-year analysis period from 2006-2011 and then further extended to 11 years from 2006-2017 to supplement the results with more data. During its operational term, CloudSat experienced a battery failure which led to a gap in data from April 2011 - June 2012. After this time frame, CloudSat was restricted to Daylight-Only operations (DO-Op) for the remainder of the analysis period. The cloud shield and frontal analysis for an example case on 01 December 2006 at 06 UTC is shown in Fig. 4.1a. The satellite path is seen cutting through the thermal ridge at nearly a right angle to its axis in Fig. 4.1b. Each grid column along the satellite path is associated with a vertical profile taken by the active sensors aboard the spacecraft, giving a top-down point of view of the hydrometeors in the column.

4.1 Individual Hydrometeor Profiles

Retrievals along these vertical profiles provide a wealth of information about the 3-D cloud and precipitation distribution at those locations. The CPR collects reflectivity profiles across a horizontal footprint of 1.4 km x 1.7 km at a vertical resolution of 240 m. An example of the reflectivity information taken along the satellite path through the 06 UTC 1 December 2006 occluded identification is shown in Fig. 4.1c. Marchand et al. (2008) developed a hydrometeor detection algorithm based upon these reflectivity returns and constructed a geometric profile (i.e., "a cloud mask") by differentiating between those CPR returns that were likely to have been scattered by hydrometeors and those that could represent noise or radar clutter. The final product, called 2B-GEOPROF, generates a more refined "cloud mask" depicting a spatial distribution of hydrometeor layers in each profile, as well as reflectivity values from the measured radar return power. CPR operates with wavelengths that are an order of magnitude smaller than most weather radars, meaning that it's able to penetrate optically thick layers and "see" cloud particles. However, it is still incapable of accurately detecting non-precipitating liquid clouds and thin cirrus, such as those with reflectivity values less than -30 dBZ (Mace and Zhang, 2014). The Vertical Feature Mask (VFM) developed by Vaughan (2009) can differentiate between aerosols and clouds and detect optically thin layers that have reflectivity values below CPR's sensitivity (Mace and Zhang, 2014), creating another "cloud mask" that fills in the gaps of Marchand et al. (2008)'s mask. Mace et al. (2009) further advanced 2B-GEOPROF by combining the capabilities of the CPR and CALIOP to create

a radar-lidar geometric profile (RL-Geoprof). CloudSat and CALIPSO shared a compact configuration within the A-Train during this study's analysis period, one that supports the assumption that both instruments simultaneously observe the same volume of the atmosphere. RL-Geoprof is provided regularly with each retrieval under the name "2B-GEOPROF-LIDAR".

The present study utilized 2B-GEOPROF-LIDAR to observe the hydrometeor structure along every CloudSat-CALIPSO orbit in the database. Cloud top and cloud base heights are given at the precise altitude at which the first and last pulses are scattered by cloud particles, respectively. A joint hydrometeor mask can be created using these heights. The use of "hydrometeor" rather than cloud or precipitation particles hereafter is deliberate as the instruments cannot distinguish between actively falling particles and those that are suspended. A boolean condition, "cloudy" (if between a cloud base and top) or "clear" (if between cloudy layers), was applied to the 250 m thick grid cells constituting each vertical profile. 2B-GEOPROF-LIDAR will only define a new layer if 960 meters of free space exists between the top of a previous layer and the bottom of the new layer (Mace and Zhang, 2014). Using this condition, the product constructs a hydrometeor mask consisting of a maximum of 5 distinct layers in each column. This limiting factor does not pose a problem for the mostly deep and continuous clouds found within the TROWAL region. Figure 4.1d demonstrates the produced hydrometeor mask for the 06 UTC 01 December 2006 identification.

While 2B-GEOPROF-LIDAR can detect the presence of suspended and actively falling

hydrometeors within the TROWAL precisely, it cannot offer any information about the surface precipitation type or rate. The 2C-PRECIP-COLUMN product, described in Haynes et al. (2009), utilizes path integrated attenuation (PIA) and strength of surface backscatter to gather information about precipitating particles in the column. The group claims that CPR's high sensitivity to smaller particles renders the sensor well-suited to identify where precipitation might be occurring, especially over open water as the reduced ground clutter provides a clearer return. Since the present study only considers maritime cyclones, this particular strength would seem to offer a perfect fit. Ice particles complicate the dependence of the product on attenuation as it will not scatter or absorb surface backscatter. Since ice is the predominant cloud phase at middle and higher latitudes (Field and Heymsfield, 2015), the geographic location of a majority of the occluded identifications in the database limits the viability of precipitation rate retrievals. Haynes et al. (2009) also stresses that the quality of the rate of retrieval can be gravely affected by multiple scattering effects in areas of intense precipitation, such as the trowal region of an occluded midlatitude cyclone. The integrated effect of these various limitations is exemplified in Fig. 4.1e for the same identification as in Figs. 4.1a-d. Meaningful surface precipitation rates are only registered for the southernmost portion of the orbit, despite the frozen and mixed precipitation most certainly occurring at higher latitudes as well as the higher reflectivities coinciding with those locations. This result may arise from the absence of a reflectivity bright band in Fig. 4.1c, which suggests that the freezing level is at the ground and all surface precipitation rate contains ice. As a result, 2C-PRECIP-COLUMN would not register any surface precipitation rate in the vicinity of the wide

reflectivity tower at 58°N shown in Fig. 4.1c. Therefore, results showing characteristic surface precipitation rates within the TROWAL is not included in this study and will be considered in future work using other resources.

4.2 Constructing composite cross-sections of CloudSat-CALIPSO products

Constructing composite cross-sections of the 2B-GEOPROF-LIDAR hydrometeor structure and 2C-PRECIP-COLUMN surface precipitation rates within the identified OTRs involves the challenge of standardizing the derivation of information from satellite profiles taken across a wide range of orientations that individual orbit patterns might take through the OTR. The construction proceeds via a methodology similar to that used for the thermodynamic and kinematic composites of Chapter 2. This method is best described using a schematic of a single analysis time, shown in Fig. 4.2 for the previously analyzed 06 UTC 1 December 2006 occluded identification. The construction of the thermodynamic and kinematic composites in Chapter 2 proceeded from identification of a cross-section transect at the median longitude of a qualifying cluster. MERRA-2 data from all occluded identifications were then averaged along that transect line to construct those composites. Since the CloudSat-CALIPSO orbit paths traverse the OTR at a variety of orientations, a variation of the previous compositing methodology is required in each MERRA-2 grid column (gray lines in Fig. 4.2a). Since the challenge is to collapse the information from a curved cross-section through a 3-D volume onto a line (like the cross-section transect

line in Fig. 4.2a), we adopt the following strategy. First, the precise position of the OTR axis is determined at the degraded resolution of the MERRA-2 data used in construction of the composite transects in Chapter 2. Starting at the intersection of the regressed OTR axis (black line in Fig. 4.2a) with each MERRA-2 grid column, the maximum 700 hPa θ_e in each column is identified. The line connecting each of these identifications is the 700 hPa θ_e ridge (pink curve in 4.2a). By construction, in every grid column, the distance from this curve to the adjusted OTR axis is zero, therefore it will be referred to as the D0 (Distance = 0) line. Secondly, only the portion of an orbit path that falls within the longitudinal range of the qualifying cluster and within ±1500 km of the D0 line is considered. This area is enclosed by the rectangular box ("transect area") drawn in Fig. 4.2b. These restrictions facilitate the automated selection of qualifying satellite orbits since any profile that does not lie within the prescribed area will be disregarded. Out of the 22,329 6-hourly analysis times identified globally (2006-2017) in the occluded identification database described in Chapter 2, this detection scheme determined 4,828 cases to also have a CloudSat-CALIPSO overpass traverse through the "transect area" in this manner.

Along with a set of lines parallel to the cross-section transect line in Figs. 4.2a,b (referred to as "width" lines), the equidistant lines parallel to D0 (referred to as "distance" lines) form an irregular grid over the transect area (Fig. 4.2c). As illustrated in Fig. 4.2d, it is the distance from the OTR measured along a width line that determines where the CloudSat-CALIPSO profile information taken at any column on the grid is placed along the composite cross-section line.

Constructing composites of the hydrometeor structure through the OTR requires collecting information from each of the CloudSat-CALIPSO orbits comprising the desired composite. For each such orbit, the first analysis step is to determine how many profiles fall within each 100 km distance increment delineated by the distance lines in Fig. 4.2d. The profiles are organized into a histogram centered on the D0 line with "distance bins" representing each 100 km increment based on their distance value, as shown in Fig. 4.3a for the 06 UTC 1 December 2006 case. By visualizing each of the 250 m thick grid cells in Fig. 4.1b as "altitude bins", the second analysis step determines the quantity of cells at various altitudes marked as "cloudy" (maroon "+"'s in Fig. 4.1b) and "clear" in each distance bin from Fig. 4. For example, Fig. 4.3b shows that the most "cloudy" cells found along the orbit through the identified OTR on 1 December 2006 at 06 UTC are found at 400 km to the northeast of the D0 line and about 8 km above the surface. This methodology was applied to CloudSat-CALIPSO orbits traversing the "transect area" in all occluded identifications and the results of the previously described sub steps were preserved in preparation for constructing what we will refer to as the "grand composite".

When constructing the grand composite, the results of the previously described analysis steps are considered first. The histograms dissecting the number of profiles in each distance bin (e.g., Fig. 4.3a) from each occluded identification in the analysis period were summed together. Figure 4.4a shows the composite histogram resulting from this step for all NH occluded identifications from 2006 – 2017. Secondly, all histograms for accumulated "cloudy"/"clear" grid cells per distance and altitude bin (e.g., Fig. 4.3b) were then summed together. Figure 4.4b shows the consequent composite for all NH cases. Finally,

as was done with the singular case shown in Fig. 4.3, the full composite of hydrometeor frequency across all orbits through all occluded identifications is constructed by dividing the composite histogram in Fig. 4.4b by that in Fig. 4.4a. The resulting grand composite of hydrometeor frequency of occurrence across all identified NH OTRs is shown in Fig. 4.4c.

Chapter 5

CloudSat-CALIPSO Climatological Applications

As explained in the methodology described in the previous chapter, a subset of the occluded cyclone database used in Chapter 2 is constructed by finding those identifications with a CloudSat-CALIPSO orbit that is coincident in time and space with the structure. This database was derived using the method described in Naud et al. (2018), which used 5 years of MERRA-2 data from 2006-2011. During this time period, 13,185 occluded snapshots were objectively identified using the methodology described in Chapter 2. It should be noted that this stark reduction in occluded identifications from Chapter 3 is mostly a result of the shorter span of time considered for this initial analysis. To further reduce the sample size, only 2,595 cases of the 13,185 total occluded identifications were found to have CloudSat-CALIPSO observations available within the transect area of the

OTR. The hydrometeor information derived from the vertical profiles along the orbit within this region was collapsed onto a single cross-section traversing through the OTR at the same angle as the cross-section transect in Fig. 2.4. This cross-section begins on the western edge of the OTR and cuts through the structure poleward with the D0 line at the center (vertical dashed line) in each of the composites presented in this chapter.

5.1 Verification of hydrometeor compositing method

Figure 5.1a shows the composite vertical θ_e structure for all identifications with a co-incident CloudSat-CALIPSO transect constructed from the boreal winter (DJF) cases during the 5-year analysis period. An occluded thermal structure can be observed in this cross-section with a slightly poleward-tilting axis of maximum θ_e at the intersection of the warm and cold fronts. Due to the Earth's curvature and the resultant convergence of meridians near the poles, polar orbiters such as CloudSat and CALIPSO tend to "see" more storms close to the poles than at lower latitudes. As a result, Fig. 5.1a is more likely to be influenced by "colder" occlusions, thereby limiting the tilt of the axis of maximum θ_e – consistent with the relationship found in Chapter 3 between 700 hPa maximum θ_e and the tilt of the TROWAL axis. When compared with a composite θ_e cross-section that includes all the identified OTRs in the occluded cyclone database (not shown), Fig. 5.1b demonstrates that the decrease in sample size from the Naud et al. (2023) database resulted in negligible variations from the canonical occluded thermal structure.

Also described in the previous methodology section was the notion that all portions of

CloudSat-CALIPSO orbits that fell within the transect area of each identified OTR were considered in the compositing process. Figure 5.1c exhibits the vertical thermal structure generated by using the "nearest neighbor approach" outlined in Chapter 4 to composite MERRA-2 grid point values from the NH winters during 2006-2011. Employing the aforementioned compositing method, where all available observations along each satellite path were taken into account, results in a robust occluded thermal structure similar to the "colder" identifications depicted in Fig. 3.4, as demonstrated by the comparable tilt and stratification in the axis of maximum θ_e. While the warm front resembles the warm-frontal portion of the canonical TROWAL structure, the bundle of moist isentropes representing the cold front contrasts with those shown in Fig. 3.4. Given the larger number of occlusions "seen" by CloudSat-CALIPSO at higher latitudes, orbits are more likely to observe the poleward edge of the OTR than the equatorward edge. This would lead to more profiles taken through the warm front than the cold front of NH cyclones, producing the more robust warm frontal structure in Fig. 5.1c.

In addition to describing the inclusion of all orbits within the transect area, Chapter 4 also noted that the satellite paths rarely crossed through the median point of the associated OTR structure at a right angle. In fact, a nonnegligible number of paths observed no part of the qualifying cluster itself, only the hydrometeors on either flank of the structure. It may therefore seem that there might be an imbalance of information provided by the satellite profiles depending on the quantity and orientation of orbits travelling through each region of the transect. However, the composite difference in Fig. 5.1d indicates that only modest disparities exist between a composite constructed

using all CloudSat-CALIPSO profiles within the "transect area" and one created by only using information along the cross-section transect through the median point (not shown). Specifically, the largest magnitude differences lie 500+ km poleward of the transect midpoint with an absolute value of 3 K at most. The minor contrast found in the center of the OTR ($< |1|$ K) is present in a shallow layer right above the boundary layer. The lack of significant discrepancies between the two verify that using every vertical profile along the orbit segment produces similar results to just using those few orbits that intersect the OTR through the median point at a right angle. As a result, either method can be used somewhat interchangeably. Employing the larger collection of data allows more information about the hydrometeor structure within the occluded quadrant to be highlighted instead of focusing on the very few profiles that intersect the OTR at a nearly perpendicular angle.

5.2 Structure of composite hydrometeor frequency of occurrence from 2006-2011

5.2.1 Northern Hemisphere composites

Figures 5.2a-b depict the hydrometeor frequency of occurrence across all satellite-observed OTRs in the NH during boreal winter from 2006-2011. A distinct tower of hydrometeors most frequently forms at the center of the OTR and extends poleward with increasing height. This robust tower is connected to a thin band of hydrometeors in the lower cold sector that is present in 40-50% of cases in the analysis period. Within the tower,

hydrometeors tend to be present most often with a frequency of 90% of the time at the surface, at the midpoint of the composite cross section and within 100 km on the poleward side. The overlaid composite vertical θ_e profile in Fig. 5.2a demonstrates that the hydrometeor tower follows the tilt of the axis of maximum θ_e characteristic of the occluded thermal structures in the database. The horizontal extent of the updraft shown in the ω contours in Fig. 5.2b also follows the tilt of the axis of maximum θ_e. These simultaneous results corroborate a connection between the trajectory of the upward moving air within the TROWAL and the lofting or creation of hydrometeors by this same vertical motion. This is especially true at the center of the cross-section where the maximum in hydrometeor frequency is collocated with the most intense values of ω.

Expanding the NH composites to average all seasons throughout the 5-year analysis period forges the hydrometeor structures displayed in Fig. 5.3. A tower similar to that in Fig. 5.2 still remains, however averaging all seasons diminishes the overall magnitude of hydrometeor frequency. The particles observed in the cold sector of the NH winter composite (Fig. 5.2) are less frequent in both spatial extent and magnitude, stopping short of 1200 km southwest from the ridge with a frequency of only 40%. The hydrometeor maximum finds itself localized to the layer closest to the surface throughout all seasons as it does in boreal winter, which is immediately in the center of the OTR axis and extending 200 km to the northeast. Hydrometeors were present in this location in $\sim$60% of cases and 50% of the time in the layer immediately above it. The tilt of the TROWAL axis deepens and steepens in the θ_e composite cross-section on Fig. 5.3a, becoming more comparable to the canonical occluded thermal structure described in Chapter 1 and shown

in the "warmest" occluded identifications in Chapter 3. The exaggerated tilt of the axis of maximum θ_e is accompanied by the same steepening of the updraft at the center of the OTR axis in Fig. 5.3b, with a slight displacement of the maximum vertical motions toward the pole. The magnitudes of both the θ_e and ω distributions are relatively the same as those in Fig. 5.2, despite expanding the sample size of cases in the composites.

Similar to the composite results found in Chapter 3, further detail regarding the NH hydrometeor structures during the 2006-2011 analysis period is afforded by stratifying them by maximum value of θ_e at 700 hPa in the OTR. Using the same distribution as in Fig. 3.2, the hydrometeor masks along each of the median cross-section transects for each identification in Bin I-VI is composited to create the structures shown in Fig. 5.4. The 3 core contours of MERRA-2 θ_e data (solid black) in each composite demonstrates the warm-occluded thermal structure for all cases in each bin. Figure 3.4 demonstrates the steepening of the TROWAL axis with warmer 700 hPa maximum θ_e. The warm frontal portion in the "coldest" bin (Bin I; Fig. 5.4a) appears intact, however the dilapidated cold front is discordant with the canonical occluded thermal structure. As discussed earlier in Chapter 3, cataloguing occluded identifications by their 700 hPa maximum θ_e effectively results in a sorting by latitude. Figure 3.3a showed that the OTRs in Bin I formed at higher latitudes. Due to the orientation of occluded cyclones and the angle at which polar orbiters intersect with the structure at those latitudes, it is likely that the satellites are mostly viewing the warm frontal portion of the occluded thermal structure and very little of the cold front within the OTR. This latitudinal bias that accompanies a polar orbit likely compromises the amount of data used to construct that portion of the structure in

Bin I. It is also possible that the 3 moist isentropes that capture the TROWAL on the warm frontal side of the OTR are confined to the surface in the cold sector. The poleward tilt of the axis of maximum θ_e is at its most intense in the "warmest" bin (Bin VI; Fig. 5.4f), akin to the Bin VI in Fig.3.4f.

Similar to the NH structure in Fig. 5.3a, the orientation of the hydrometeor tower also follows the general tilt of the canonical axis of maximum θ_e in all bins of Fig. 5.4. Unlike the updrafts in Fig. 3.5 that adhere to the changing slopes of the TROWAL axis that vary with the 700 hPa maximum θ_e values found in each bin of Fig. 3.2; the incline of the hydrometeor tower remains constant for each bin in Fig. 5.4. However, the vertical development of the hydrometeors within the tower, increases with warmer 700 hPa θ_e values. This can be seen by comparing the "cloud top" in the Bin I composite (Fig. 5.4a) at 400 hPa or 8 km, with the "cloud top" in Bin VI (Fig. 5.4f) at 220 mb or 11 km. The magnitude of hydrometeor occurrence does not share this seemingly monotonic relationship between vertical growth and 700 hPa θ_e values. Whereas a majority of the hydrometeors were generally observed near the surface, the intensity of their frequencies of occurrence and the spatial expanse of the low-level maximum fluctuated between each bin. This could be a result of the unequal and minimal sample size of identified OTRs in each bin. Although magnitudes varied inconsistently across all the composites, the "warmest" tower consists of the lowest frequency of hydrometeors overall throughout the full structure. Figure 3.2 showed that the most intense vertical motions and highest θ_e in the TROWAL for identifications in Bin VI provided evidence to support the suggestion that LHR exerts a substantial influence in producing a canonical occluded thermal

structure. The relatively low magnitudes in Fig. 5.4f contradict this hypothesis as the large upward vertical motions and attendant LHR that are likely to be occurring in Bin VI OTRs would be associated with greater occurrences of hydrometeors.

5.2.2 Southern Hemisphere composites

Similar hydrometeor frequency structures form when compositing all SH cases from 2006-2011 (Fig. 5.5). The tilt of the hydrometeor tower present in the center of the cross-section is comparable to that in the NH composites, though the vertical and horizontal extent is different from the structures seen in Fig. 5.3. Hydrometeors extend farther poleward than seen in the NH composites with greater frequencies in general throughout the structure. Hydrometeor formation also maximizes within the layer closest to the surface at the center of the TROWAL in the SH, but with larger magnitudes and greater vertical extent. Hydrometeors were present at this location in ∼80% of cases from 2006-2011, which is 20% more than in the NH. This departure from the NH continues aloft, where the frequency gradually diminishes from 70% to 40% at the top of the tower. The same thin band of hydrometeors present in NH winter occluded identifications (Fig. 5.2) also occurs in the SH and with a more robust structure than the all-inclusive NH composite (Fig. 5.3). On the other hand, the vertical motion structure within the OTR does not vary greatly between hemispheres. The updraft shown in Fig. 5.5b exhibits a similar tilt and magnitude of ω to that in Fig.5.3b, despite the stronger stratification on the warm frontal side as compared to that in Fig. 5.3. As explained in Chapter 3, synoptic-scale vertical motions within the TROWAL are primarily driven by PVA by the

thermal wind (Sutcliffe, 1947), a mid-tropospheric forcing. Regions of high local static stability, such as the layer between 900-650 mb in Fig. 5.5, should dampen the vertical motions at that level in the column. Therefore, the wave-scale forcings below and at the level of the warm front must be stronger in the SH occluded identifications than the NH. Since PVA by the thermal wind is often most robust above this layer, another synoptic forcing may play a role.

The discrepancies in hydrometeor presence between hemispheres presents a curious result. A majority of the SH is open water with fewer land masses than the NH. Such a maritime landscape would likely be characterized by fewer cloud condensation nuclei and therefore, a lower number of larger cloud droplets than their continental counterparts. A larger initial droplet size encourages the collision-coalescence process to produce precipitation-sized droplets faster, increasing the chances of hydrometeors precipitating out of the cloud. While this enhanced precipitation could lead to the broader area of high frequencies of occurrence seen in the SH hydrometeor tower, it would also lead to shorter residence times for precipitation-sized droplets in the lower atmosphere. Also, a majority of the OTRs identified in the SH were in Bin II of Fig. 3.6 (i.e., the second "coldest" bin) and therefore have "colder" 700 hPa θ_e values than most of the ridges identified in the NH (Fig. 3.2). This speculation is corroborated by the minimal tilt in the TROWAL axis in Fig. 5.5a. Due to the colder nature of SH occlusions, the attendant precipitation is most likely confined to the near-surface layer with clouds dominating most of the upper levels. Therefore, the low-level hydrometeor maximum observed in Fig. 5.5 can be reasonably assumed to be precipitation particles and the SH structures are precipitating in $\sim$80%

of the 6h analysis times recorded. Continuous drizzle is characteristic of the stratiform clouds often observed along and ahead of the warm front and on the warm side of an OTR axis (Mason, 1952; Tracton, 1969; Hobbs, 1978; Nicholls, 1987; Wood, 2005). A low-level maximum in cloud cover is most likely tied to widespread stratiform clouds that get trapped in the marine boundary layer (Verlinden, et al., 2011; Mace and Protat, 2018), which has been commonly observed in other studies (Klein and Hartmann, 1993; Mace et al., 2009; Verlinden et al., 2011; Haynes et al., 2011; Mace and Protat, 2018 and others). The area of 70% hydrometeor occurrence present directly above the precipitating surface layer and to the north-east of the OTR axis in Fig. 5.5 points to the long-term occupancy of the such stratiform structures associated with this region of a cyclone. This distribution of hydrometeors suggests a diabatic explanation of the agreement in vertical motions between hemispheres, despite the difference in stratification within their respective TROWAL structures. With the precipitation sequestered to the lowest layer, very little evaporative cooling remains to offset latent heat release of condensation when clouds form throughout the remainder of the column. This excess diabatic heating could fuel stronger upward vertical motions above the marine boundary layer in addition to the stronger synoptic forcing to explain the vigorous ω values observed in Fig. 5.5b.

5.3 Structure of composite hydrometeor frequency of occurrence from 2006-2017

The reduced number of occluded identifications with available CloudSat-CALIPSO observations likely increased the sensitivity of the composites to outliers and small deviations from the true average hydrometeor structure within an OTR. Dividing this smaller quantity into 6 bins in Fig. 5.5 seemingly exacerbated this issue. In order to enhance the robustness of the hydrometeor composites, the compositing process outlined in Chapter 4 was conducted for an 11-year analysis period from 2006-2017, similar to Naud et al. (2023) and Chapter 2. Out of 22,329 occluded 6h snapshots identified in the Naud et al. (2023) database, 4,828 coincided with a CloudSat-CALIPSO orbit within the transect area from 2006-2017. The composite structures constructed from these cases showed that the NH lacked the quantity of identifications detected in the SH (not shown). This discrepancy between the hemispheres forced the use of fewer 700 hPa maximum θ_e bins to allow any detectable signal to emerge. Fewer bins would also alleviate the sensitivity demonstrated by the composite structures in Fig. 5.5. Figure 5.6 shows the cumulative distribution function of frequency of occurrence for each value of 700 hPa maximum θ_e in occluded identifications throughout 2006-2017 (solid). Using this global distribution for all transects, thresholds were determined to separate the population into terciles. The "coldest" bin (240 – 293 K) contains the least frequent cases, whereas the most identifications had a 700 hPa maximum θ_e within the range of 294 – 304 K. The frequency of occurrence then began to diminish once again in the "warmest" bin (305 – 360 K).

Histograms of NH (dashed) and SH transects (dot-dashed) were also constructed with the same thresholds in Fig. 5.6. NH cases are shifted towards warmer values of 700 hPa maximum θ_e, with the most frequent cases having a maximum θ_e of ∼306 K at 700 hPa. The SH distribution is "colder" in general, where OTRs were identified to have a maximum θ_e of ∼295 K most frequently. Since there are more cases observed by CloudSat-CALIPSO in the SH than the NH, the overall distribution (solid) resembles the SH distribution (dot-dashed). In order to examine this difference further, each hemisphere's population is partitioned into terciles separately, resulting in unique 700 hPa maximum θ_e bins for both.

Partitioning the NH cases in the 11-year database into terciles required θ_e values of 298 K and 312 K for the thresholds, following the clear shift towards warmer 700 hPa maximum θ_e from the global population shown in Fig. 5.6. Figure 5.7 depicts the composite hydrometeor structures of the identifications in each bin. The gray lines in Fig. 5.7a-c indicate the MERRA-2 vertical θ_e structure along the cross-section, which shows the canonical occluded thermal structure and more increasingly so with warmer θ_e values. Similar to Fig. 5.4, the extent of the hydrometeor structure expands upward and poleward with higher θ_e, according to the 50%+ contour in 5.7d-f. The magnitude of overall frequency of occurrence throughout the tower maximizes in the center bin (298K< θ_e <312 K), where the surface layer (<2 km) contains magnitudes up to 85-90% and the 50%+ contour extends to 10 km (Fig. 5.7e). It was shown in Fig. 3.5 and Chapter 3 that the most vigorous upward vertical motions and supposed attendant LHR were located within the TROWAL region of the "warmest" occluded identifications. With the superimposition of these two

related phenomena, greater magnitudes of hydrometeors occurring at higher frequencies should be observed. However, while the vertical extent of the tower continues to increase into the "warmest" bin, there is a significant decrease in hydrometeors mainly above 5 km, mimicking the result found in Fig. 5.4f and contradicting the expected hypothesis.

This contradiction may well be confined to NH occluded structures because the same discrepancy does not appear in the SH composites constructed over the same time period (Fig. 5.8). The MERRA-2 vertical θ_e structure contains similar characteristics to the 2006-2011 composite in Fig. 5.5a, with less tilt in the axis of maximum θ_e and higher stratification within the TROWAL region than the NH composite. The SH terciles are bound by 700 hPa maximum θ_e values of 291 K and 301 K, which are substantially colder than the thresholds that similarly stratify the NH identifications. Magnitudes of hydrometeor frequency within the overall structure continue to increase with "warmer" θ_e values, as one would expect, with the 50%+ and 75%+ contour extending vertically through the tower. While a greater number of hydrometeors are present at higher altitudes in occluded identifications with "warmer" 700 hPa maximum θ_e values, the top of the hydrometeor tower remains at the same height with only a slight ascent from 10 km to 11 km in the "warmest" bin. Similar to the 5-year composite in Fig. 5.5, adding 6 years of observations confirms that there are generally greater frequencies of hydrometeor occurrence within the TROWAL of SH occluded cyclones than in their counterparts in the NH. The absolute maximum of 85-90% frequency present in the lower-levels of the NH composite (Fig. 5.7) is also present in all 3 SH bins with a vertical extension up to 3 km in Fig. 5.8e and as high as 6 km in the "warmest" composite (Fig. 5.8f).

The curious differences between the NH and SH composite hydrometeor structures seen in the 2006-2011 analysis resurfaces here, despite almost doubling the sample size of cases considered between 2006-2017. The SH composite hydrometeor structures generally lean towards "colder" 700 hPa maximum θ_e values for both the 5-year and 11-year analysis periods. Other disparities that could lead to a difference in hydrometeor presence within the TROWAL of occluded cyclones include terrain, land cover, climatological jet intensity and location as well as the presence of the Southern Ocean, a vigorous band of cold water circulating around Antarctica that dampens heat release from the ocean surface to the atmosphere (Cai et al., 2023). On the other hand, sharp decreases in hydrometeor frequencies at upper-levels may not be specific to NH occluded structures. If such a phenomenon were to occur in SH occluded cyclones, but at lower frequencies, its occurrences might be lost in a climatological average. One could restrict the histogram bin thresholds to remain consistent for each hemisphere's hydrometeor composite to evaluate whether or not the sharp decrease in the "warmest" category is truly sequestered to the NH. This peculiar asymmetry warrants further investigation that is not included in this study.

It was shown in Fig. 5.6 that the global distribution of hydrometeor frequency of occurrence closely followed the SH distribution as a result of the bias in sample size since the number of SH occluded identifications observed by CloudSat-CALIPSO was far greater than in the NH. Figure 5.9 shows the composite hydrometeor frequencies of occurrence when combining all cases across the globe, which demonstrates the partiality towards the SH hydrometeor tower and occluded thermal structures (Fig. 5.9a-c) in Fig. 5.8. However, the influence of the NH hydrometeor structure is not completely absent as the

distribution of frequencies in Fig. 5.9d is similar to Fig. 5.9e, with a notable decrease throughout the tower in the "warmest" bin. The maximum frequency remains within the layer closest to the surface, with the magnitudes increasing from 75-80% in the "coldest" bin (Fig. 5.9d) to 85-90% in Fig. 5.9e, then decreasing down to 80% in the "warmest" bin (Fig. 5.9f). The hydrometeor top also exhibits the same vertical expansion with increasing 700 hPa maximum θ_e as the NH composites, growing from 8 km in Fig. 5.9d to 10.5 km in Fig. 5.9f. The vertical growth in the tower, which can be clearly seen by the 50%+ contour in Fig. 5.9d-f, is consistent with the vertical motion and θ_e composites constructed in Naud et al. (2023).

Unsurprisingly, the full hydrometeor frequency composite averaging all identified NH cases from all seasons throughout the 11 years (Fig. 4.4c) incorporates most of the characteristics in each of the bins in Fig. 5.7. The composite hydrometeor tower tilts poleward with height, reaching $\sim$ 9.5 km at the top. Hydrometeors occur just north of the OTR axis at 2 km in 85-90% of cases. The notable drop in hydrometeors above 5 km depicted in Fig. 5.7f appears in this global composite with the next largest magnitude of 70-75% frequency concluding at 5 km, and then decreasing with height within the structure. Although the 25%+ contour extends as far as 700 km poleward of the OTR, the hydrometeors within the 50%+ contour remains proximal to the OTR axis and fairly erect, similar to the structure in the "coldest" NH bin (Fig. 5.7d). CloudSat-CALIPSO observed hydrometeors more frequently in the SH, according to the grand composite in Fig. 5.10, which shows an absolute maximum of 85-90% frequency of occurrence in the first 3 km within the core of the tower, a full 5-10% greater than the absolute maximum

in the NH (Fig. 4.4c). Similar to the 2006-2011 composite in Fig. 5.5, the vertical extent of the hydrometeor tower maximizes around ∼8.5-9 km. Despite the shallower top height, the 50%+ contour extends to higher altitudes within the SH tower (8 km) than in the NH structure, similar to the results found during the 2006-2011 period. Unlike the 5-year composite, however, Fig. 5.10 demonstrates a more dramatic tilt than was shown in Fig. 5.3 and Fig. 5.5, which showed relatively consistent slopes in both structures. Another difference of note between the hemispheres is the horizontal expansion of the main hydrometeor tower, specifically the 25%+ contour, does not penetrate as far poleward in the SH as the same contour in the NH. Therefore, cloud/precipitation structures within OTRs in the SH are shallower, but substantially cloudier than their NH counterparts.

The composited global cloud distribution across OTRs from 2006-2017 (Fig. 5.11a) is consistent with the distribution of both θ_e (also shown in Fig. 5.11a) and the vigorous upward vertical motions shown in Naud et al. (2023). The understanding that the largest portion of cloudiness and precipitation within an occluded cyclone is strongly linked to the TROWAL and not the surface fronts is corroborated by the stark maximum of hydrometeors present at the center of the OTR axis in Fig. 5.11a. Based on the vertical θ_e structure, the surface occluded front is most likely located between 100 and 200 km equatorward of the 700 hPa ridge line, where the hydrometeor presence does not extend beyond 5 km in altitude and only in 50-65% of cases. Whereas at the center of the OTR axis, hydrometeors were present in 85-90% of all cases throughout the 11-year period, decreasing in even intervals with height until the top of the tower at ∼10 km with a magnitude of 40%.

Using the same CloudSat-CALIPSO observation dataset, Naud et al. (2010; 2012) constructed hydrometeor composites across warm fronts and Naud et al. (2015;2016; 2018) did the same across cold fronts. The latter were identified at 850 hPa using a combination of the thermal gradient method from Hewson (1998) applied to MERRA-2 and the wind direction change method of Simmonds et al. (2012) applied to MERRA-2 winds. The warm fronts were also obtained using Hewson (1998)'s method applied to MERRA-2 data at 1 km above mean sea level. Figure 5.11b and Fig. 5.11c shows the frequency of occurrence across cold and warm fronts, respectively, from 2006-2017 across the globe. The canonical occluded thermal structure shown in the MERRA-2 θ_e cross-section in Fig. 5.11a is completely unique and does not share any resemblance to the θ_e structure in either frontal region. In Fig. 5.11b, moist isentropes maintain a relatively stable configuration in the cold sector and only slightly bow down towards the low-level hydrometeor maximum (40%) within 100 km into the warm sector. The moist isentropes in Fig. 5.11c slope upwards across the warm front and above the surface cold air ahead of the warm front. The hydrometeors across the cold front do not exceed a magnitude of 40% and are mostly concentrated in the warm sector out ahead of the front. On the other hand, hydrometeors are more frequent across the warm front with a maximum of 60% frequency occurring immediately ahead of the frontal boundary. However, it is clear that hydrometeor frequencies are considerably larger in occluded quadrants than they are in warm frontal regions and even more so in the case of cold fronts. This is partially caused by a lower variability in hydrometeor distribution across OTRs compared to warm fronts. But overall, Fig. 5.11a provides observational evidence that during the years 2006-2017, the

lion's share of cloudiness and precipitation associated with occluded identifications falls within the occluded quadrant, separate from the surface occluded front, by a generous margin irrespective of location on the globe.

Chapter 6

Discussion and Conclusions

The post-mature phase structure of a mid-latitude cyclone is characterized by a 3-D, sloping thermal ridge, that scientists at the Canadian Meteorological Service termed the TROugh of Warm air ALoft (TROWAL). The TROWAL is the essential structural feature of a warm-occluded cyclone, and its development not only links to cyclone dynamics, but also influences the distribution and intensity of precipitation. Though a number of studies (e.g., Wallace and Hobbs, 1977; Schultz and Mass, 1993; Martin, 1998a,b; 1999a,b; Posselt and Martin, 2004; Schultz and Vaughan, 2011) have considered the aspects of the structure, evolution and dynamics of occluded cyclones, there has been no attempt to develop an automated scheme to identify occlusions in gridded data sets. In fact, the present study represents the first contribution that constructs a climatology of occluded cyclones based upon identification of their canonical 3-D thermal structure. Consequently, current

understanding of the structural evolution, dynamics and cloud and precipitation distribution associated with occluded cyclones is derived predominantly from the analyses of individual case studies and/or model simulations. In order to expand this rather limited perspective on investigations of the occluded stage of the cyclone life cycle, this study describes an automated method to identify such occluded thermal structures and illustrates its applications. Such applications include the analysis of the global distribution of occluded identifications, as well as the construction of thermodynamic, kinematic, and hydrometeor composite cross-sections through the occluded thermal ridge (OTR) to learn more about the structure within occluded extratropical cyclones.

The detection method, quantified using the F-parameter derived in Chapter 2, arises from the evaluation of the divergence of the unit vector in the direction of the 1000-500 hPa thickness gradient. Regions of convergence of the unit vector identify thickness ridges while regions of divergence detect thickness troughs. With only minor empirical adjustments, the F-parameter was found to consistently and accurately identify the OTR, and therefore, occluded cyclones, in any gridded data set. Though it is possible to usefully employ the F-parameter without a priori knowledge of cyclone positions and tracks, our experience suggests that doing so invites a level of uncertainty that can compromise the results. Coupled with a cyclone tracking algorithm involving synoptically-informed parameters , however, F can be used to identify the position and track of occluded cyclones around the globe. Using this methodology, Naud et al. (2023) compiled a collection of all occluded cyclones from the Naud et al. (2018) cyclone database during the operational time frame of CloudSat and CALIPSO (2006-2017). This new database

allowed for the exploration of the composite characteristics of 22,329 6-hourly occluded identifications throughout the analysis period.

The composites revealed that Northern Hemisphere (NH) occlusions occur most frequently during the winter season (DJF) and most often poleward of the mean jet in the Pacific basin and in a strip from the Labrador Sea to the Greenland coast in the Atlantic Ocean. On the other hand, occluded identifications tend to occur poleward of 40°S throughout most of the year in the Southern Hemisphere (SH), and maximize in frequency in SH autumn (MAM). Binning winter occluded identifications according to the value of their respective 700 hPa θ_e maximum along the thickness ridge axis allows for further categorization of these features, as well as new insights regarding the influence of the temperature and moisture of mid-troposphere warm sector air on the robustness of the resulting occluded thermal structures. Two-thirds of all NH occluded identifications had a maximum 700 hPa θ_e in the range of 293-313 K, while the extremes ranged from as low as 275 K to as high as 335 K. In the SH, two-thirds of wintertime occlusion identifications had a lower maximum 700 hPa θ_e in the range of 288 – 304 K. Perhaps unsurprisingly, the analysis found that in both hemispheres the intensity of the composite vertical motion in the TROWAL was generally inversely proportional to the latitude at which the occlusion was identified, presumably as a result of the weakly stratified air found in occluded sectors of "warmer" storms. The "colder" composites in both hemispheres also suggested that such high-latitude cyclones tend to have a shallower version of the canonical occluded thermal structure and also exhibit less tilt to the axis of maximum θ_e.

The variability in occluded thermal structures and in the intensity of the vertical motion characterizing the 6 groups of occlusions in each hemisphere are almost certainly physically related. Martin (1999a) found that the convergence of the along-isentrope ($\vec{Q}_s$) component of the $\vec{Q}$-vector (Hoskins et al., 1978), closely related to PVA by the thermal wind (Sutcliffe, 1947; Trenberth, 1978), simultaneously accounts for the production of the OTR and provides the predominant dynamical forcing for ascent in the occluded quadrant of cyclones. The TROWAL air stream, a cyclonically ascending air stream, that originates in the warm sector boundary layer and flows through the TROWAL is supported by this quasi-geostrophic forcing. The fact that the "warmer" occlusion in the present analysis have both higher θ_e feeding the TROWAL air stream and larger vertical motion within the TROWAL leads them to also produce larger amounts of LHR in the occluded quadrant. Consequently, a couplet of lower tropospheric cyclonic PV production and upper-tropospheric PV erosion is clearly evident in these composite cross-sections. Additionally, as the maximum 700 hPa θ_e in the TROWAL increases, so does the robustness of the associated occluded thermal structure (Fig. 3.8 and Fig.3.4). The coincidence of these structural characteristics in the composites depicted here offers new evidence for the suggestion made by Posselt and Martin (2004) that LHR plays an important role in the production of the canonical occluded thermal structure. The more concentrated and vigorous composite vertical motions of the NH wintertime occlusions revealed in the analysis, however, remains in need of explanation.

The automated objective identification method described here permits the quantitative exploration of many other aspects of occluded cyclones, including the distribution of

clouds and precipitation across occluded sectors. CloudSat and CALIPSO observations were utilized to construct composite cross-sections of hydrometeor frequency of occurrence. In addition to the full duration of the satellites' residence time in the A-Train constellation (2006-2017), a composite analysis during a subset of the time period (2006-2011) was conducted. Out of 13,185 occluded cyclone identifications identified during 2006-2011, only 2,595 had concurrent CloudSat-CALIPSO observations available. Extending the database out to 11 years added 2,233 daytime-only snapshots with available CloudSat observations into the composite structures.

The analysis relied on the construction of composite cross-sections of hydrometeor frequency along a transect line perpendicular to the occluded thermal ridge (OTR), anchored at the point of maximum 700 hPa θ_e at each point along the OTR axis. In order to arm this 2D composite with the greatest number of observations available, the full 3D data volume provided along the CloudSat-CALIPSO transect was used. This proved to be sufficient for reconstructing the hydrometeor distribution along a hypothetical cross-section parallel to the cross-section transect (see Chapter 2) that cuts through the OTR at the same angle as the cross-section transect. Figure 5.1d showed the differences between a composite constructed in this way (Fig. 5.1d) and one created using the methodology in Chapter 2 (Fig. 5.1a), which proved to be negligible ($< |3|$ K).

Consistent with the results of prior case studies (e.g., Crocker et al, 1947; Godson, 1951; Penner, 1955; Martin, 1998a, b), the majority of hydrometeors in the composites presented here is found at the center of the OTR axis and within the area poleward of the

OTR, i.e., the TROWAL region, and not at the surface occluded front. Additionally, the main hydrometeor tower follows the tilt of the TROWAL axis, similar to the updrafts discussed in Chapter 3. Overall, hydrometeor structures across NH OTRs are more horizontally extensive, deeper, and displaced farther poleward than SH structures; while the maximum magnitude in frequency throughout the hydrometeor tower is larger in the SH than the NH. To better understand these differences, the hydrometeor cross-sections across all OTRs in the database were stratified by 700 hPa maximum θ_e.

Stratifying cases in this way revealed a tendency for hydrometeor coverage to expand vertically with increasing θ_e across all OTRs. The reduced sample size of occluded identifications used in this analysis compelled employment of terciles to divide the cases evenly, instead of the 6 categories used in Chapter 3. Doing so unveiled a θ_e threshold in the NH that, when surpassed, results in a decline of the hydrometeor maximum in the TROWAL. Such a result is unexpected for a region characterized by strong synoptic-scale ascent (Fig. 3.9). This phenomenon was not present in the SH composites, despite a similar distribution of ω. A decrease in hydrometeor frequency in regions of vigorous upward vertical motion may be the signature of high-frequency embedded convection. Such convection has been observed in or near the comma head of extratropical cyclones (Rosenow et al., 2014; Plummer et al., 2015; Rauber et al., 2015), and in warm conveyor belts (Crespo and Posselt, 2016; Binder et al., 2016; Oertel et al., 2019; Binder et al., 2021). The SH showed comparable updraft intensities to the vertical motions in the NH without the decrease in upper-level hydrometeors in the "warmest" bin. The local static stability on the warm frontal side of the SH OTR (Fig. 5.5a) was found to be stronger than the same region

in the NH composite (Fig. 5.3a). Therefore, the synoptic-scale forcings (i.e., PVA by the thermal wind) must be greater in the SH at the level of the axis of maximum θ_e or below to overcome the relatively stable stratification present in the SH TROWAL environment.

The observations presented here suggest that hydrometeors are more frequently observed in OTRs in the SH than in the NH. Aside from differences in sample size between the hemispheres, any number of physical processes or variables and their combinations might underlie this contrast such as variations in static stability, frequency of convection, or the type of hydrometeors. The mechanisms driving this discrepancy warrant further investigation. Future exploration into the ice and liquid water content profiles within the hydrometeor structures could shed light on the type of hydrometeors present within the column. For the hypothesis offering convection frequency as a reason for the disparity between hemispheres, future work will explore the diabatic heating distribution across OTRs using Global Precipitation Measurement profiles.

Using an automated identification scheme, this study set out to observe the hydrometeor distribution within occluded quadrants and lay the ground work for new insights about the microphysics that occur within that region of the ubiquitous extratropical cyclone. The same scheme can be applied to the evaluation of the global distribution of occlusions as portrayed in a free-running integration of different versions of the Goddard Institute for Space Studies global climate model (GCM) (Kelley et al., 2020). Preliminary results of that analysis suggest that model extratropical cyclones tend to form farther poleward than those in the reanalysis data. And, though the model produces occlusions that

appear realistic, it does so nearly twice as frequently as the reanalysis data. These and other questions regarding the nature of occluded cyclones in a warmer climate can now be considered quantitatively through application of the objective identification method outlined in this thesis. Future efforts to build upon this foundation will no doubt yield fruitful and new insights regarding the late stages of the extratropical cyclone life cycle.

Chapter 7

References

Atkinson, B.W. and Smithson, P.A. (1974). Mesoscale circulations and rainfall patterns in an occluding depression. *Quart.J. Royal Meteor. Soc.*, **100**(423, 3-22.

Bauer, M. and Del Genio (2006). Composite analysis of winter cyclones in a GCM: Influence on climatological humidity. *J. Climate*. **19**(9).1652-1672.

Bauer, M. Tselioudis, G. and Rossow, W.B. (2016). A new climatology for investigating storm influences in and on the extratropics. *J.Appl.Meteor.Clim.*. **55**(5),1287-1303. https://doi.org/10.1175/JAMC-D-15-0245.1

Berman, J.D. and Torn, R.D. (2019) The impact of initial condition and warm conveyor belt forecast uncertainty on variability in the downstream waveguide in an EXMWF case study. *Mon. Wea. Rev*, **147**(11). 4072-4089.

Berry,G., Jakob, C. and Reeder, M. (2011). Recent global trends in atmospheric fronts. *GeophysicalResearchLetters*, **38**(21), L21812,1-6.

Binder, H., Boettcher, M., Joos, H., and Wernli, H. (2016). The role of warm conveyor belts for the intensification of extratropical cyclones in Northern Hemisphere winter. *J.Atmos.Sci.*, **73**(10), 3997-4020.

Binder, H., Rivière, G., Arbogast, P., Maynard, K., Bosser, P., Joly, B., et al. (2021) Dynamics of forecast-error growth along cut-off and its consequence for the prediction of a high-impact weather event over southern France. *Q.J.Roy.Meteor.Soc.*, 147(739), 3263–3285. Available from: https://doi.org/10.1002/qj.4127

Bjerknes, J., and H. Solberg, 1922: Life cycle of cyclones and the polar front theory of atmospheric circulation. *Geofys. Publ.*, **3**(1), 1–18.

Browning, K. A., 1990: Organization of clouds and precipitation in extratropical cyclones. *Extratropical Cyclones: The Erik Palmén Memorial Volume*, C. W. Newton and E. O. Holopainen, Eds., Amer. Meteor. Soc., 129–153

Browning and Harrold, K.A. and Harrold, T.W., 1969. Air motion and precipitation growth in a wave depression. *Quart.J. Royal Meteor. Soc.*, **95**, 288-309.

Wenju Cai, Libao Gao, Yiyong Luo, Xichen Li, Xiaotong Zheng, Xuebin Zhang, Xuhua Cheng, Fan Jia, Ariaan Purich, Agus Santoso, Yan Du, David M. Holland, Jia-Rui Shi,

Baoqiang Xiang, Shang-Ping Xie, 2023. Southern Ocean warming and its climatic impacts. *ScienceBulletin*. **68**(9),946-960. ISSN: 2095-9273, https://doi.org/10.1016/j.scib.2023.03.049.

Carlson, T.N., 1980. Airflow through midlatitude cyclones and the comma cloud pattern. Mon. Wea. Rev., **108**, 1498-1509.

Crespo, J. A., Posselt, D. J., 2016. A-Train-based case study of stratiform–convective transition within a warm conveyor belt. *Mon.Wea.Rev.*, **144**(6), 2069-2084.

Crocker, A., W. L. Godson, and C. M. Penner, 1947: Frontal contour charts. *J.Atmos.Sci.*, **4** (3), 95–99.

Eckhardt, S., A. Stohl, H. Wernli, P. James, C. Forster, and N. Spichtinger, 2004: A 15-year climatology of warm conveyor belts. *J. Climate*, $bf17$, 218–237.

Eliassen, A., Kleinschmidt, E. (1957). *Dynamic meteorology* (pp. 1-154). Springer Berlin Heidelberg.

Field, P. R., Heymsfield, A. J. (2015). Importance of snow to global precipitation. *Geophys.Res.Letters*, **42**(21), 9512-9520.

Galloway, J. L., 1958: The three-front model: Its philosophy, nature, construction and use. *Weather*, **13** (1), 3–10.

Galloway, J. L., 1960: The three-front model, the developing depression and the occluding process. *Weather*, **15**, (9), 293–309.

Gelaro, R., McCarty, W., Suarez, M. J., Todling, R., Molod, A., Takacs, L., ... Zhao, B. (2017). The Modern-Era Retrospective Analysis for Research and Applications, Version 2 (MERRA-2). *J.Climate*, **30**(14), 5419–5454.

Godson, W. L., 1951: Synoptic properties of frontal surfaces. *Quart.J.Roy.Meteor.Soc.*, *77*,(334), 633–653.

Harrold, T.W., 1973. Mechanisms influencing the distribution of precipitation within baroclinic disturbances. *Quart.J.Roy.Meteor.Soc.* **99**. 232-251.

Haynes, J. M., T. S. L'Ecuyer, G. L. Stephens, S. D. Miller, C. Mitrescu, N. B. Wood, and S. Tanelli, (2009) Rainfall retrieval over the ocean with spaceborne W-band radar, *J.Geophys.Res.*, **114**, D00A22, doi:10.1029/2008JD009973.

Haynes, J. M., Jakob, C., Rossow, W. B., Tselioudis, G., and Brown, J.(2011) Major characteristics of Southern Ocean cloud regimes and their effects on the energy budget, *J.Climate*, **24**, 5061–5080.

Hewson, T. D., 1998: Objective fronts. *Meteor.Appl.*, **5**, (1), 37–65.

Hewson, T. D., and H. A. Titley, 2010: Objective identification, typing and tracking of the complete life-cycles of cyclonic features at high spatial resolution. *Meteor.Appl.*, **17**, (3), 355–381.

Hobbs, P. V. (1978). Organization and structure of clouds and precipitation on the mesoscale and microscale in cyclonic storms. *Rev.Geophys.*, **16**(4), 741-755.https://doi.org/10.1029/F

Hoskins, B.J., 1999. Sutcliffe and His Development Theory. In: Shapiro, M.A., Grønås, S. (eds) *TheLifeCyclesofExtratropicalCyclones*. Boston, MA. American Meteorological Society, 81-86. https://doi.org/10.1007/978-1-935704-09-68

Hoskins, B. J., I. Draghici, and H. Davies, 1978: A new look at the ω-equation. *Quart.J.Roy.Meteor.S* **104**, (439), 31–38.

Hoskins, B. J., M. E. McIntyre, and A. W. Robertson, 1985: On the use and significance of isentropic potential vorticity maps. *Quart.J.Roy.Meteor.Soc.*, **111**, (470), 877–946.

Hoskins, B. J., and K. I. Hodges, 2005: A new perspective on southern hemisphere storm tracks. *J.Climate*, **18** (20), 4108–4129.

Iskenderian, H. (1988). Three-dimensional airflow and precipitation structure in a non-deepening cyclone. *Weatherandforecasting*, **3**(1), 18-32.

Jewell, R., 1981: Tor Bergeron's first year in the Bergen school: Towards an historical appreciation. Weather and Weather Maps, *Springer*, 474–490.

Kalnay, E., and Coauthors, 1996: The NCEP/NCAR 40-year reanalysis project. *Bull.Amer.Meteor.S* **77** (3), 437–472.

Kanamitsu, M., Ebisuzaki, W., Woollen, J., Yang, S. K., Hnilo, J. J., Fiorino, M., and Potter, G. L. (2002). Ncep–doe amip-ii reanalysis (r-2). *Bull.Amer.Meteor.Soc.*, **83**(11), 1631-1644. https://doi.org/10.1175/BAMS-83-11-1631

Kelley, M., and Coauthors, 2020: GISS-e2. 1: Configurations and climatology.*J. Adv. Model. Earth S* **12** (8), e2019MS002 025.

Keyser, D., B. D. Schmidt, and D. G. Duffy, 1992: Quasigeostrophic vertical motions diagnosed from along-and cross-isentrope components of the q vector. *Mon.Wea.Rev.*, **120**(5), 731–741.

Klein, S. A., Hartmann, D. L. (1993). The seasonal cycle of low stratiform clouds. *J.Climate*, **6**(8), 1587-1606. https://doi.org/10.1175/1520-0442(1993)006¡1587:TSCOLS¿2.0.CO;2

Kurz, M., 1988: Development of cloud distribution and relative motions during the mature and occlusion stage of a typical cyclone development. Preprints, *PalmenMemorialSymp.onExtrat* Helsinki, Finland. Boston, MA. Amer. Meteor. Soc., 201–204.

Mace, G. G., Q. Zhang, M. Vaughan, R. Marchand, G. Stephens, C. Trepte, and D. Winker (2009), A description of hydrometeor layer occurrence statistics derived from the first year of merged Cloudsat and CALIPSO data, *J.Geophys.Res.*, **114**, D00A26, doi:10.1029/2007JD009755.

Mace, G. G., and Q. Zhang (2014). The CloudSat radar-lidar geometrical profile product (RL-GeoProf): Updates, improvements, and selected results. *J.Geophys.Res.Atmos.*, **119**, doi:10.1002/ 2013JD021374.

Mace, G. G., Protat, A. The Occurrence Frequency and Properties of Geometrically Thin Stratiform Clouds Associated with Precipitating Shallow Convection over the Southern

Ocean. https://aerosol-soc.com/wp-content/uploads/2017/06/4-GeraldMace.FM9.2017.Poster.pdf

Madonna E., H. Wernli, H. Joos, and O. Martius, 2014: Warm conveyor belts in the ERA-Interim dataset (1979-2010). Part I: Climatology and potential vorticity evolution. *J.Climate*, **27**, 3-26, doi:10.1175/JCLI-D-12-00720.1.

Marchand, R., G.G. Mace, T. Ackerman, and G. Stephens (2008), Hydrometeor Detection Using Cloudsat—An Earth-Orbiting 94-GHz Cloud Radar. *J.Atmos.OceanicTechnol.*, **25**, 519–533.

Martin, J. E., 1998a: The structure and evolution of a continental winter cyclone. Part I:Frontal structure and the occlusion process. *Mon. Wea. Rev.*, 126 (2), 303–328.

Martin, J.E., 1998b: The structure and evolution of a continental winter cyclone. Part II:Frontal forcing of an extreme snow event. *Mon.Wea.Rev.*, **126**(2), 329–348.

Martin, J.E., 1999a: Quasi-geostrophic forcing of ascent in the occluded sector of cyclones 700 and the trowal airstream. *Mon. Wea. Rev.*, **127**, 70–88.

Martin, J.E., 1999b: The separate roles of geostrophic vorticity and deformation in the mid-latitude occlusion process. *Mon. Wea. Rev.*, **127**, 2404–2418.

Martin, J.E., 2006: *Mid-Latitude Atmospheric Dynamics: A First Course*. West Sussex, England: John Wiley Sons, Ltd.

Martínez-Alvarado, O., Joos, H., Chagnon, J., Boettcher, M., Gray, S. L., Plant, R. S., and coauthors(2014). The dichotomous structure of the warm conveyor belt. *Quart. J. Roy. Meteor.* **140**(683), 1809-1824.

Mason, B. J. (1952). Production of rain and drizzle by coalescence in stratiform clouds. *Quart.J.Roy.Meteor.Soc.*, **78**(337), 377-386.

Mass, C. F., and D. M. Schultz, 1993: The structure and evolution of a simulated mid-latitude cyclone over land. *Mon. Wea. Rev.*, **121**, 889–917.

Namias, J. (1939). The use of isentropic analysis in short term forecasting. *J.Aeronaut.Sci.*, **6**(7), 295-298.

Naud, C. M., Posselt, D.J., and van den Heever, S.C., 2012: Observational analysis of cloud and precipitation in midlatitude cyclones: Northern versus southern hemisphere warm fronts. *J.Clim.*, **25**(14), 5135–5151

Naud, C.M., Posselt. D. J., van den Heever, S.C, 2015: A CloudSat-CALIPSO view of cloud and precipitation properties across cold fronts over the global oceans. *J.Climate*, **28**, 6743– 6762.

Naud, C. M., Booth, J. F., Del Genio, A. D. (2016). The relationship between boundary layer stability and cloud cover in the post-cold-frontal region. *J.Climate*, **29**(22), 8129-8149.

Naud, C.M., Posselt, D.J., and van den Heever, S.C., 2018: Reply to comments on 'A CloudSat-CALIPSO view of cloud and precipitation properties across cold fronts over the global oceans'. *J.Clim.*, **31**(7), 2969-2975, doi:10.1175/JCLI-D-17-0777.1.

Naud, C.M., Martin, J.E., Ghosh, P., Elsaesser, G. Posselt, D.(2023) Automated identification of occluded sectors in midlatitude cyclones: Method and some climatological applications. *Quart.J.Roy.Meteor.Soc.*, 1–21. https://doi.org/10.1002/qj.4491

Nicholls, S. (1987). A model of drizzle growth in warm, turbulent, stratiform clouds. *Quart.J.Roy.Meteor.Soc.*, **113**(478), 1141-1170.

Oertel, A., Boettcher, M., Joos, H., Sprenger, M., Konow, H., Hagen, M., Wernli, H. (2019). Convective activity in an extratropical cyclone and its warm conveyor belt–a case-study combining observations and a convection-permitting model simulation. *Quart.J.Roy.Meteor.Sc* **145**(721), 1406-1426.

Penner, C., 1955: A three-front model for synoptic analyses. *Quart.J.Roy.Meteor.Soc.*, **81**(347), 89–91.

Plummer, D. M., McFarquhar, G. M., Rauber, R. M., Jewett, B. F., Leon, D. C. (2015). Microphysical properties of convectively generated fall streaks within the stratiform comma head region of continental winter cyclones. *J.Atmos.Sci.*, **72**(6), 2465-2483.

Polly, J. B., and W. B. Rossow, 2016: Cloud radiative effects and precipitation in extratropical cyclones. *J.Climate*, **29** (18), 6483–6507.

Posselt, D. J., and J. E. Martin, 2004: The effect of latent heat release on the evolution of a warm occluded thermal structure. *Mon.Wea.Rev.*, **132** (2), 578–599.

Rauber, R. M., and Coauthors, 2015: The Role of Cloud-Top Generating Cells and Boundary Layer Circulations in the Finescale Radar Structure of a Winter Cyclone over the Great Lakes. *Mon.Wea.Rev.*, **143**, 2291–2318, https://doi.org/10.1175/MWR-D-14-00350.1.

Raymond, D., 1992: Nonlinear balance and potential-vorticity thinking at large Rossby number. *Quart.J.Roy.Meteor.Soc.*, **118**(507), 987–1015.

Reed, R. J., Y.-H. Kuo, and S. Low-Nam, 1994: An adiabatic simulation of the erica iop 4storm: An example of quasi-ideal frontal cyclone development. *Mon.Wea.Rev.*, **122** (12),2688–2708.

Rienecker, M. M., Suarez, M. J., Gelaro, R., Todling, R., Bacmeister, J., Liu, E., ... Woollen, J. (2011). MERRA: NASA's modern-era retrospective analysis for research and applications. *J.Climate*, **24**(14), 3624-3648.

Rosenow, A. A., Plummer, D. M., Rauber, R. M., McFarquhar, G. M., Jewett, B. F., Leon, D. (2014). Vertical velocity and physical structure of generating cells and convection in the comma head region of continental winter cyclones. *J.Atmos.Sci.*, **71**(5), 1538-1558.

Saha, S., and Coauthors, 2010: The NCEP climate forecast system reanalysis. BAMS, **91** (8),1015–1058.

Saucier, W. J. (1955).*Principles of meteorological analysis* (Vol. 438). Chicago, Ill.: University of Chicago Press.

Schäfler, A., Harnisch, F. (2015). Impact of the inflow moisture on the evolution of a warm conveyor belt. *Quart.J.Roy.Meteor.Soc.*, **141**(686), 299-310.

Schemm, S., M. Sprenger, and H. Wernli, 2018: When during their life cycle are extratropical cyclones attended by fronts? *itBull.Amer.Meteor.Soc.*, **99**(1), 149–165.

Schmidt, G. A., and Coauthors, 2006: Present-Day Atmospheric Simulations Using GISS ModelE: Comparison to In Situ, Satellite, and Reanalysis Data. *J.Climate*, **19**, 153–192, https://doi.org/10.1175/JCLI3612.1.

Schultz, D. M., and C. F. Mass, 1993: The occlusion process in a midlatitude cyclone over land. *Mon.Wea.Rev.*, **121**(4), 918–940.

Schultz, D.M., and G. Vaughan, 2011: Occluded fronts and the occlusion process: A fresh look at conventional wisdom. *Bull.Amer.Meteor.Soc.*, **92**(4), 443–466.

Schultz, D. M., 2018: Comments on "A CloudSat–CALIPSO view of cloud and precipitation properties across cold fronts over the global oceans." *J.Climate*, *31*, 2965–2967. https://doi.org/10.1175/JCLI-D-17-0619.1

Simmonds, I., K. Keay, and J. A. Tristram Bye, 2012: Identification and climatology of southern hemisphere mobile fronts in a modern reanalysis. *J.Climate*, **25** (6), 1945–1962.

Stephens, G. L., and Coauthors, 2002: The CloudSat mission and the A-train: A new dimension of space-based observations of clouds and precipitation. *Bull.Amer.Meteor.Soc.*,**83**(12), 1771–1790

Stoelinga, M. T., J. D. Locatelli, and P. V. Hobbs, 2002: Warm occlusions, cold occlusions, and forward-tilting cold fronts. *Bull.Amer.Meteor.Soc.*, **83** (5), 709–722.

Sutcliffe, R., 1947: A contribution to the problem of development. *Quart.J.Roy.Meteor.Soc.*,**73** (317-318), 370–383.

Thomas, C. M., and D. M. Schultz, 2019(a): Global climatologies of fronts, airmass boundaries, and airstream boundaries: Why the definition of "front" matters. *Mon.Wea.Rev.*, **147**, 691–717, doi: 10.1175/MWR-D-18-0289.1.

Thomas, C. M., and D. M. Schultz, 2019(b): What are the best thermodynamic quantity and function to define a front in gridded model output? *Bull.Amer.Meteor.Soc.*, **100**, 873–895, doi: 10.1175/BAMS-D- 18-0137.1.

Tracton, M. S. (1969). The role of cellular convection within an extratropical cyclone (Doctoral dissertation, Massachusetts Institute of Technology).

Trenberth, K. E., 1978: On the interpretation of the diagnostic quasi-geostrophic omega equation. *Mon.Wea.Rev.*, **106**(1), 131–137.

Unidata. (2019). *GEneral Meteorology PAcKage*. (7.5.1). Unidata. https://unidata.github.io/gemp

Vaughan, M., K. Powell, R. Kuehn, S. Young, D. Winker, C. Hostetler, W. Hunt, Z. Liu, M. McGill, and B. Getzewich (2009). Fully automated detection of cloud and aerosol layers in the CALIPSO lidar measurements, *J.Atmos.OceanicTechnol.*, **26**, 2034– 2050.

Wallace, J. M.,and Hobbs, P. V. (1977). Atmosphere science-an introductory survey. *Atmosphere science − an introductory survey*. V.

Wernli, H., 1997: A Lagrangian-based analysis of extratropical cyclones. II: A detailed case-study. *Quart. J. Roy. Meteor. Soc.*, **23**, 1677–1706.

Wernli, H., Davies, H. C. (1997). A Lagrangian-based analysis of extratropical cyclones. I: The method and some applications. *Quart.J.Roy.Meteor.Soc.*, **123**(538), 467-489

Winker, D. M., M. A. Vaughan, A. Omar, Y. Hu, K. A. Powell, Z. Liu, W. H. Hunt, and S. A. Young, 2009: Overview of the CALIPSO mission and CALIOP data processing algorithms. *J.Atmos.Oceanic Technol.*, **26**(11), 2310–2323.

Wood, R. (2005). Drizzle in stratiform boundary layer clouds. Part I: Vertical and horizontal structure. *J.atmos.sci.*, **62**(9), 3011-3033. https://doi.org/10.1175/JAS3529.1

Verlinden, K. L., Thompson, D. W., Stephens, G. L. (2011). The three-dimensional distribution of clouds over the Southern Hemisphere high latitudes. *J.Climate*, **24**(22), 5799-5811.

Young, M. V., Monk, G. A., Browning, K. A. (1987). Interpretation of satellite imagery of a rapidly deepening cyclone. *Quart. J. Roy. Meteor. Soc.*, **113**(478), 1089-1115.

	MERRA-2 ($1.25° \times 1°$)	MERRA-2 ($2.5° \times 2°$)	NCEP-NCAR ($2.5° \times 2.5°$)
F_{max}	-10^{-9} m^{-1}	-0.5×10^{-9} m^{-1}	-0.5×10^{-9} m^{-1}
N_{min}	8	4	4
$StdSurf_{max}$	300 m	150 m	150 m
D_{max}	300 km	300 km	300 km

TABLE 2.1: Parameter values for each data set and grid resolution used in this study.

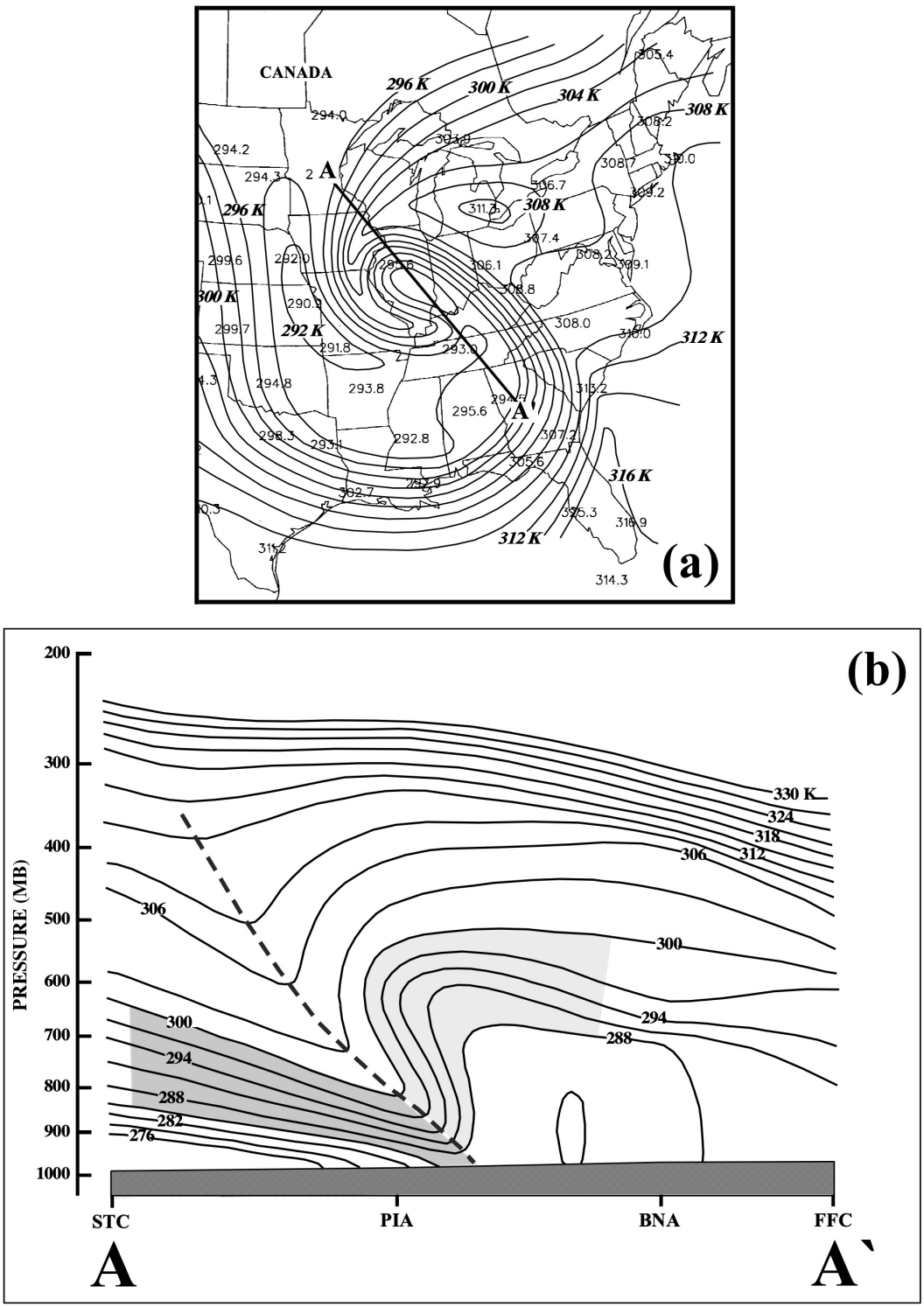

FIGURE 1.1: Occluded thermal structure observed over the central United States on 0000 UTC 20 January 1995. (a) 700 hPa equivalent potential temperature (θ_e) at this analysis time. θ_e (K) is contoured every 2 K. Cross-section along line A-A' shown in Fig. 1.1b. (b) Vertical cross-section of θ_e along line A-A' in Fig. 1.1a (from St. Cloud, MN (STC)), to Peachtree City,GA (FFC) at the aforementioned time. Solid lines are moist isentropes labeled in K and contoured every 3 K. Dashed line indicates the canonical axis of maximum θ_e that slopes upward and poleward in a warm occlusion. Light (dark) shading represents the cold (warm) frontal baroclinic zone involved in this occluded structure. Adapted from Martin (1998a)

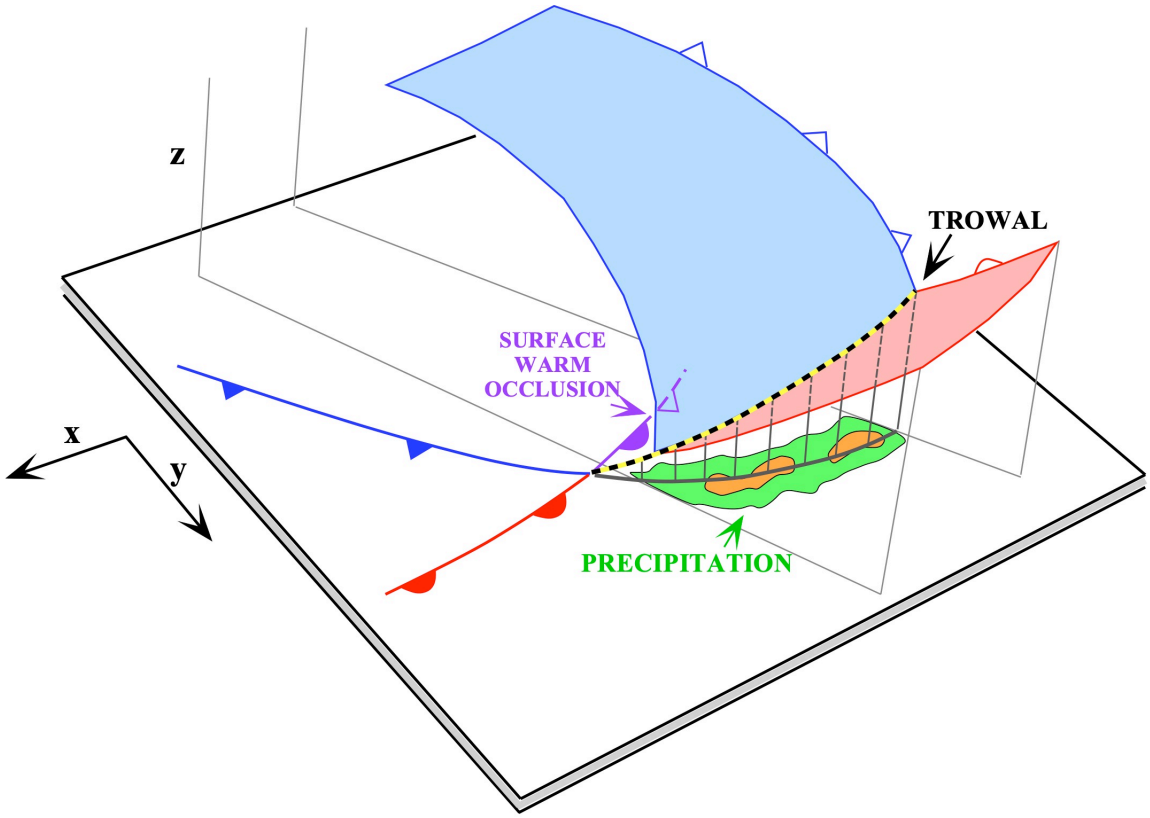

FIGURE 1.2: Schematic illustration of the trowal conceptual model. The blue shaded surface represents the warm edge of the cold frontal baroclinic zone. The pink shaded surface represents the warm edge of the warm frontal baroclinic zone. The thick dashed line (marked "TROWAL") represents the 3-D sloping intersection between the cold and warm frontal zones characteristic of warm occlusions. Schematic precipitation band is indicated as are the positions of the surface warm, cold and occluded fronts. Dark solid line through the precipitation band represents the projection of the trowal to the surface. Adapted from Martin (1999a)

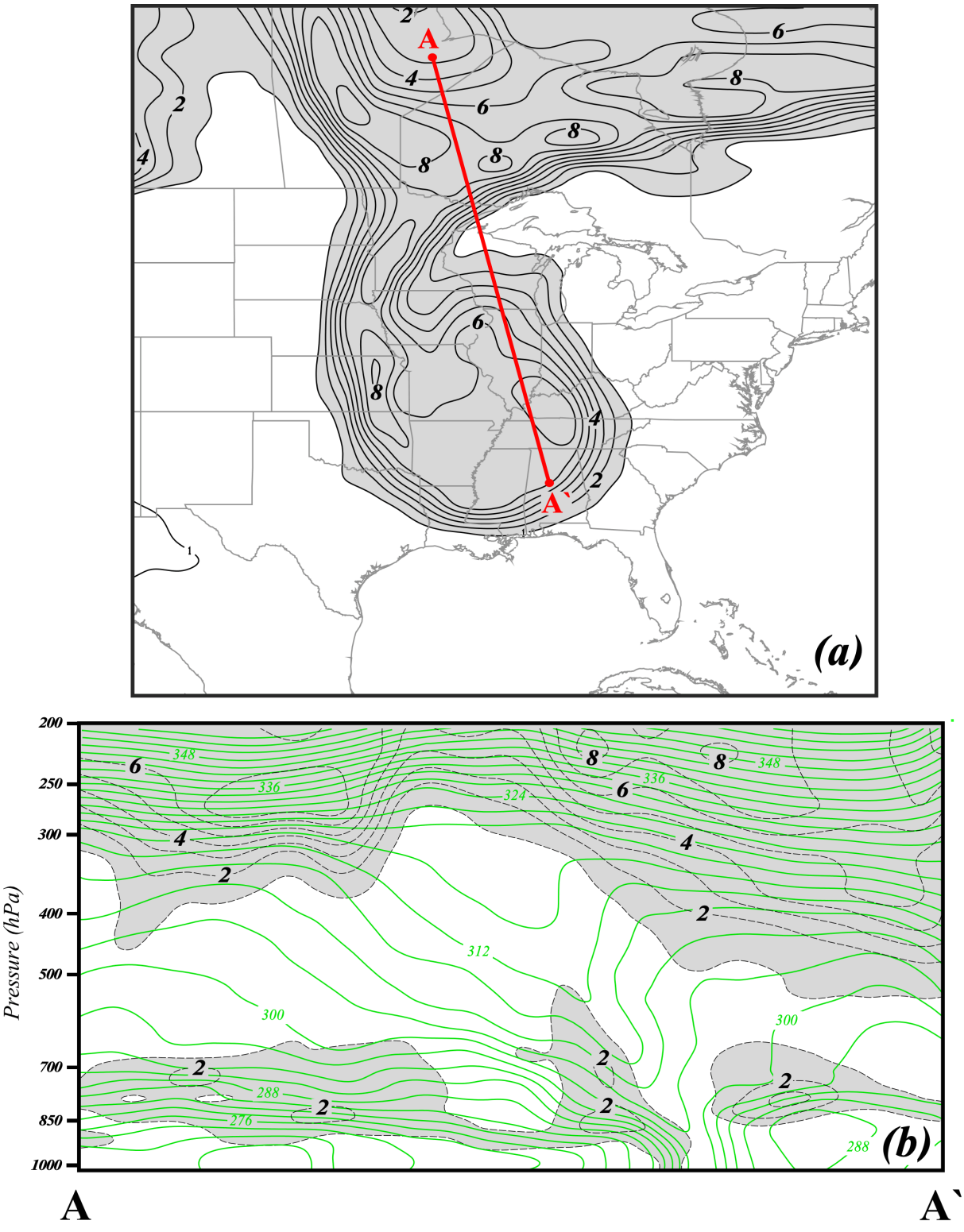

FIGURE 1.3: Illustration of the relationship between the treble clef tropopause-level potential vorticity (PV) and the warm-occluded thermal structure in the underlying troposphere. (a) Tropopause-level (250-300 hPa) PV from the CFSR valid at 1800 UTC 19 January 1995. PV is labeled in potential vorticity units (PVU) (1 PVU = 10^{-6} m^2 s^{-1} K kg^{-1}) and shaded every 1 PVU starting at 1 PVU. Cross-section along A-A' is shown in Fig. 3b. (b) Cross-section along A-A' in Figure 3a of θ_e (thin green lines) labeled in K and contoured every 3 K. Gray shading is PV labeled in PVU and shaded every 1 PVU beginning at 1 PVU.

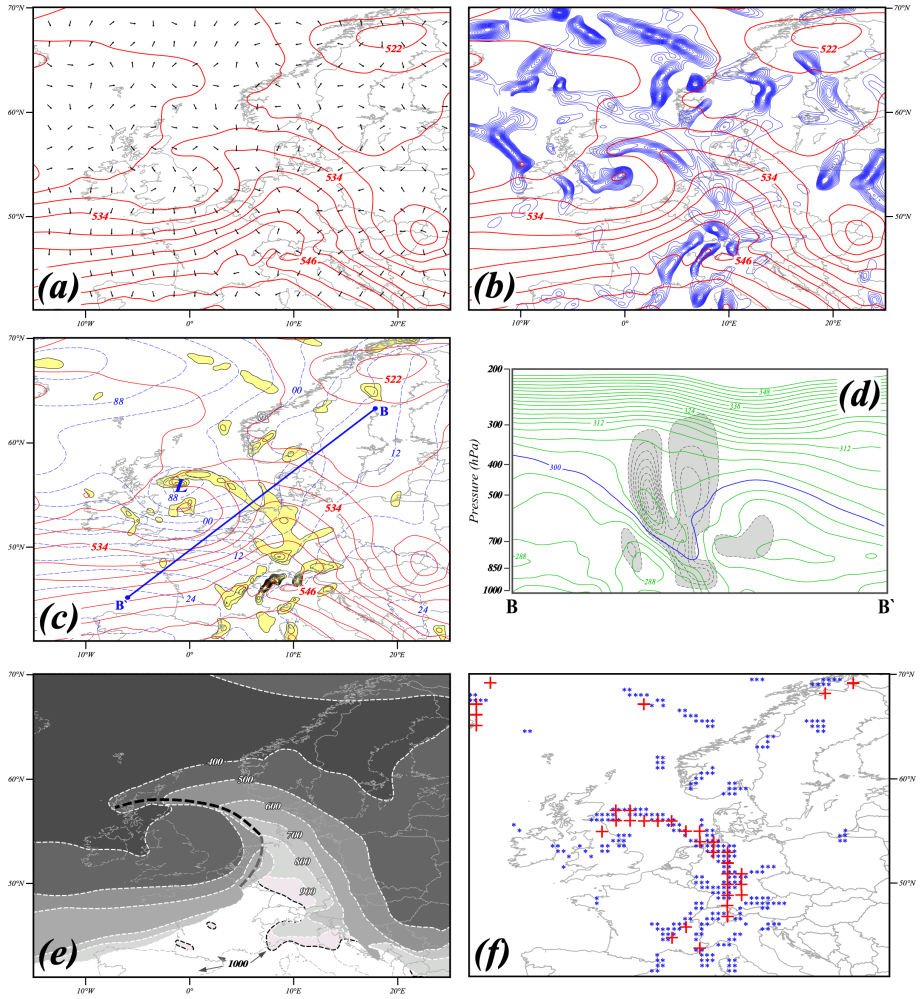

FIGURE 2.1: (a) 1000-500 hPa thickness (solid red) and $\hat{n}$, the unit vector in the direction of $\nabla\phi'$, from the CFSR valid at 0600 UTC 7 January 2008. Thickness is labeled in dam and contoured every 6 dam. Unit vectors are portrayed at every 5^{th} grid point for clarity of presentation. (b) 1000-500 hPa thickness (solid red) labeled and contoured as in Fig. 2.1a. Convergence of $\hat{n}$ (thin blue lines) contoured every -1×10^{-5} m^{-1} starting at -1×10^{-5} m^{-1}. (c) Sea-level isobars (dashed blue) and 1000-500 hPa thickness (solid red) from the CFSR valid as in (a). Isobars labeled in hPa (with leading "9" or "10" dropped) and contoured every 4 hPa. Thickness labeled and contoured as in Fig. 2.1a. Negative **F** parameter (see text) shaded in yellow and contoured every -1×10^{-9} m^{-1} starting at -1×10^{-9} m^{-1}. Vertical cross-section along B-B' is shown in Fig. 2.1d. (d) Vertical cross-section of θ_e and ω along line B-B' in Fig. 2.1c. θ_e labeled in K and contoured every 3 K with the 300 K isoline colored in blue. Upward vertical motion (gray shading) labeled in dPa s^{-1} and contoured every -2 dPa s^{-1} starting at -2 dPa s^{-1}. (e) Isobaric topography of the 300-K θ_e surface from the CFSR dataset. Thin white dashed lines are isobars on that surface and the thick dashed line is the location of the TROWAL (see text). (f) Blue asterisks identify CFSR grid points at which $\mathbf{F} < \mathbf{-1 \times 10^{-9}}$ m^{-1} at 0600 UTC 7 January 2008. Red crosses identify points on the coarsened MERRA-2 grid at which $\mathbf{F} < \mathbf{-1 \times 10^{-9}}$ m^{-1} at the same time. These grid points are highlighted as black crosses in gray squares in Fig. 2.2e.

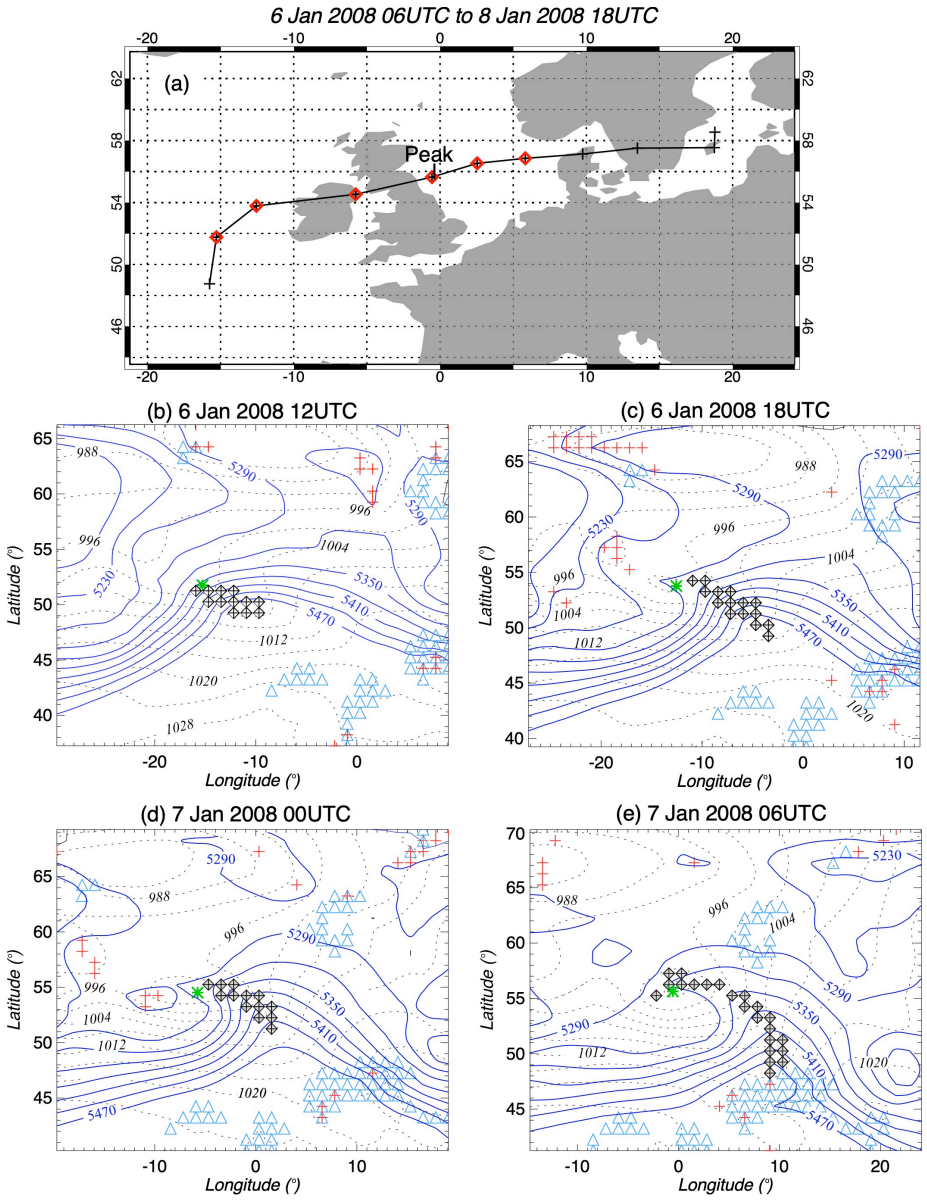

FIGURE 2.2: Illustration of the cluster tracking method. (a) Track of a cyclone in the north Atlantic from 0600 UTC to 1800 UTC 8 January 2008 from the MERRA-2 reanalysis data. Crosses represent the position of the cyclone center at each 6-hr time, red squares indicate times at which a qualifying cluster deemed the storm occluded, and "Peak" indicates the time and location of the storm's peak intensity. (b) 1000-500 hPa thickness (blue solid lines) and sea-level isobars (SLP, dotted black lines) at 1200 UTC 6 January 2008 from the MERRA-2 data. Thickness (m) is contoured every 60 m. SLP (hPa) is contoured every 4 hPa. Red and black crosses are grid points at which $F < F_{max}$. Blue triangles are grid points at which $STDSurf_{max}$ exceeds 300 m. Green star is the location of the SLP minimum. Black crosses with gray shaded squares represent grid points in a qualifying cluster (see text for explanation). (c) As in Fig.2.2b but for 1800 UTC 6 January 2008. (d) As in Fig.2.2b but for 0000 UTC 7 January 2008. (e) As in Fig.2.2b but for 0600 UTC 7 January 2008, time of peak intensity.

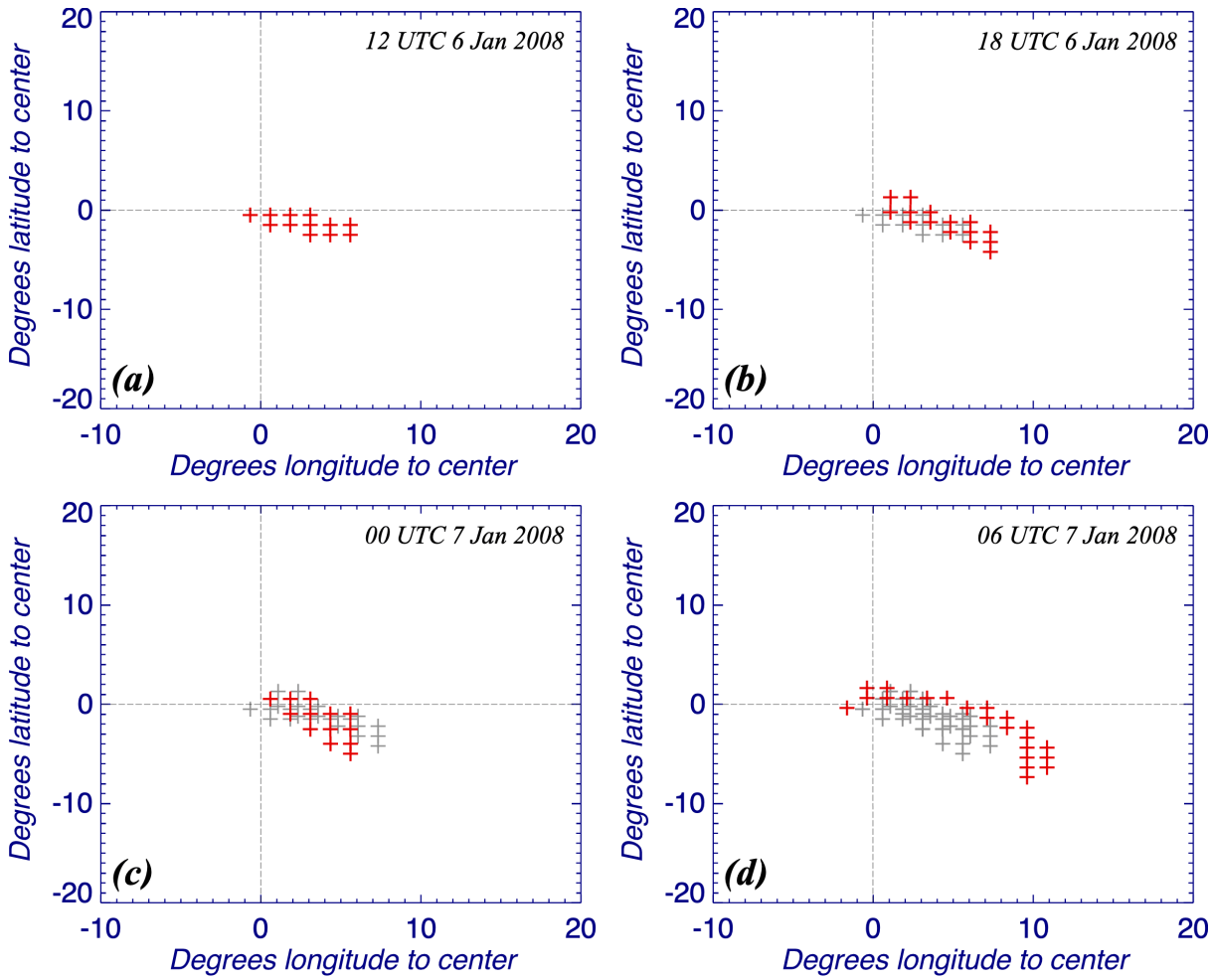

FIGURE 2.3: Cyclone-relative grid with SLP minimum at (0,0). (a) Red crosses indicate the qualifying cluster identified at 1200 UTC 6 January 2008 for the cyclone whose track is considered in Fig. 2.2. (b) As in 2.3, but with red crosses indicating the qualifying cluster identified at 1800 UTC 6 January 2008 and the gray crosses indicating qualifying clusters identified at all prior 6-hr snapshots of the cyclone depicted in Fig. 2.2. (c) As in Fig. 2.3b but with red crosses indicating the qualifying cluster at 0000 UTC 7 January 2008. (d) As in Fig. 2.3b but with red crosses indicating the qualifying cluster at 0600 UTC 7 January 2008.

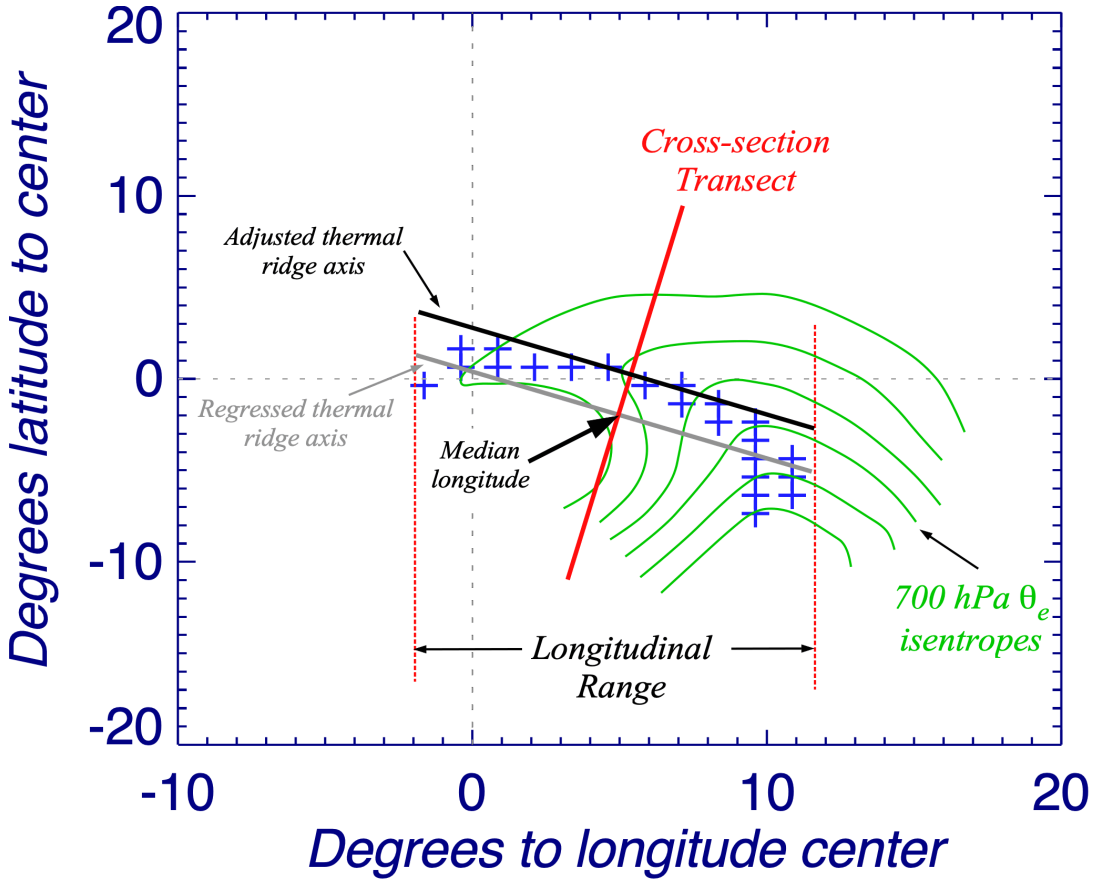

FIGURE 2.4: Illustration of the method by which the composite cross-section transect line is determined for the objective occlusion identification. Blue crosses are schematic grid points constituting a qualifying cluster. Green solid lines are 700 hPa θ_e isentropes. Red solid line is the cross-section transect line.

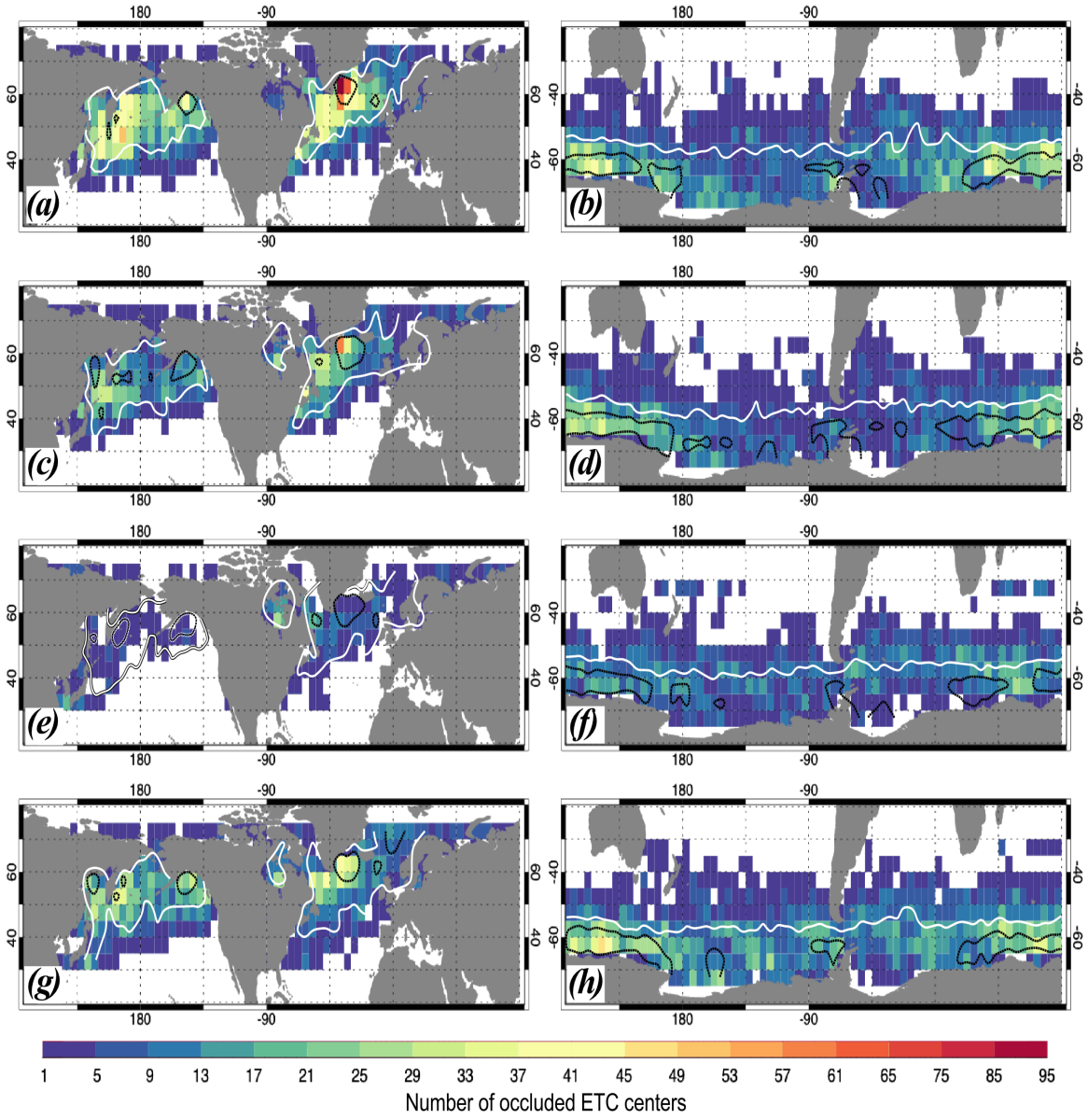

FIGURE 3.1: Distribution of all (6-hr) ETC centers that are occluded organized by hemisphere and season. Color bar refers to the number of occlusion identifications per 5°×5° box in (a) Northern Hemisphere (NH) winter (DJF), (b) Southern Hemisphere (SH) winter (JJA), (c) NH spring (MAM), (d) SH spring (SON), (e) NH summer (JJA) (f) SH summer (DJF), (g) NH autumn (SON), and (h) SH autumn (MAM). SOlid white (dashed black) lines in each panel indicate the 100 (150) cyclones per grid box contour for the given season.

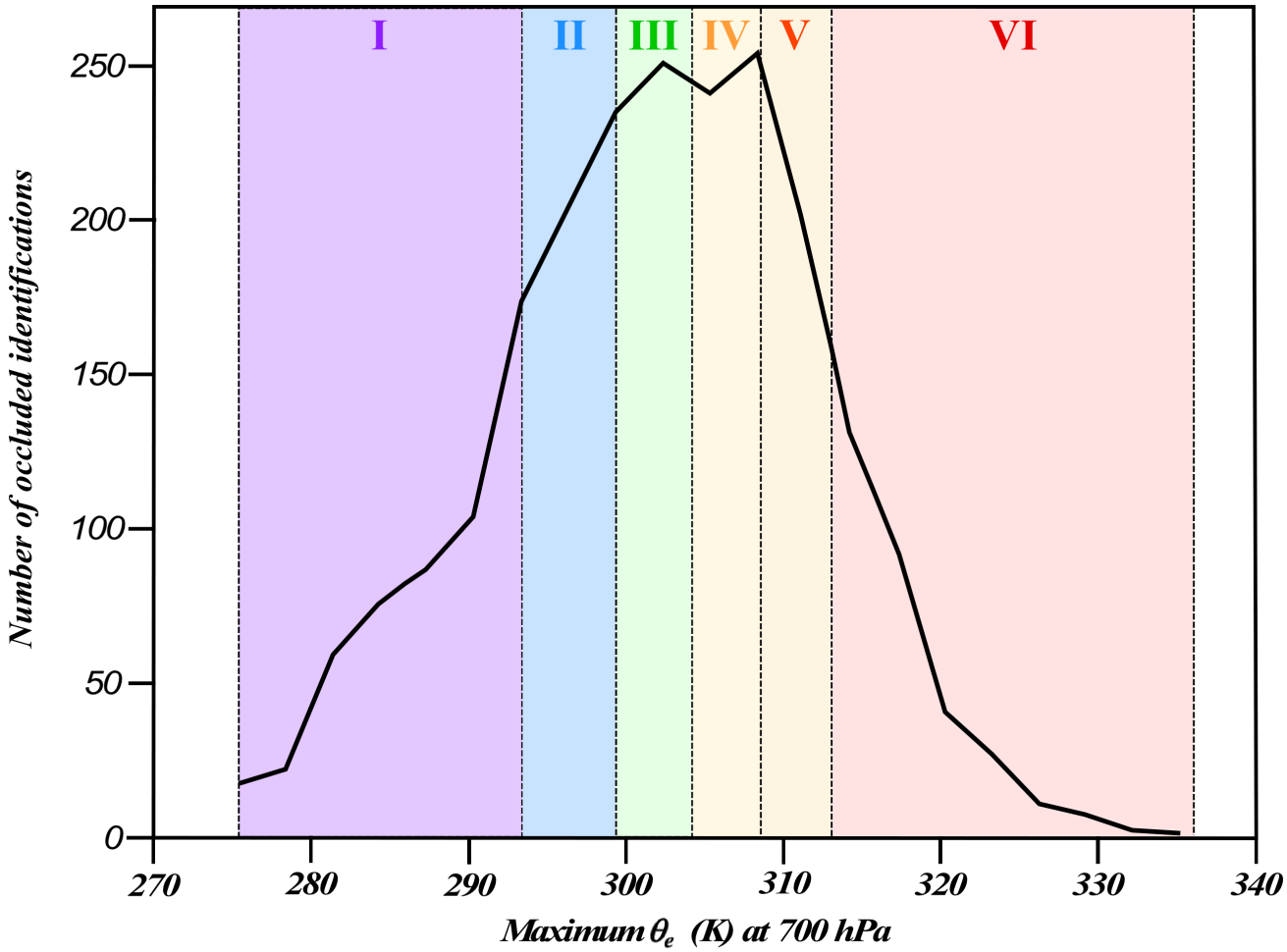

FIGURE 3.2: Cumulative distribution function of all NH wintertime occluded identifications stratified by the 700 hPa θ_e maximum along their respective thermal ridge axes. The 6 categories are referred to as Bins I-VI in the text.

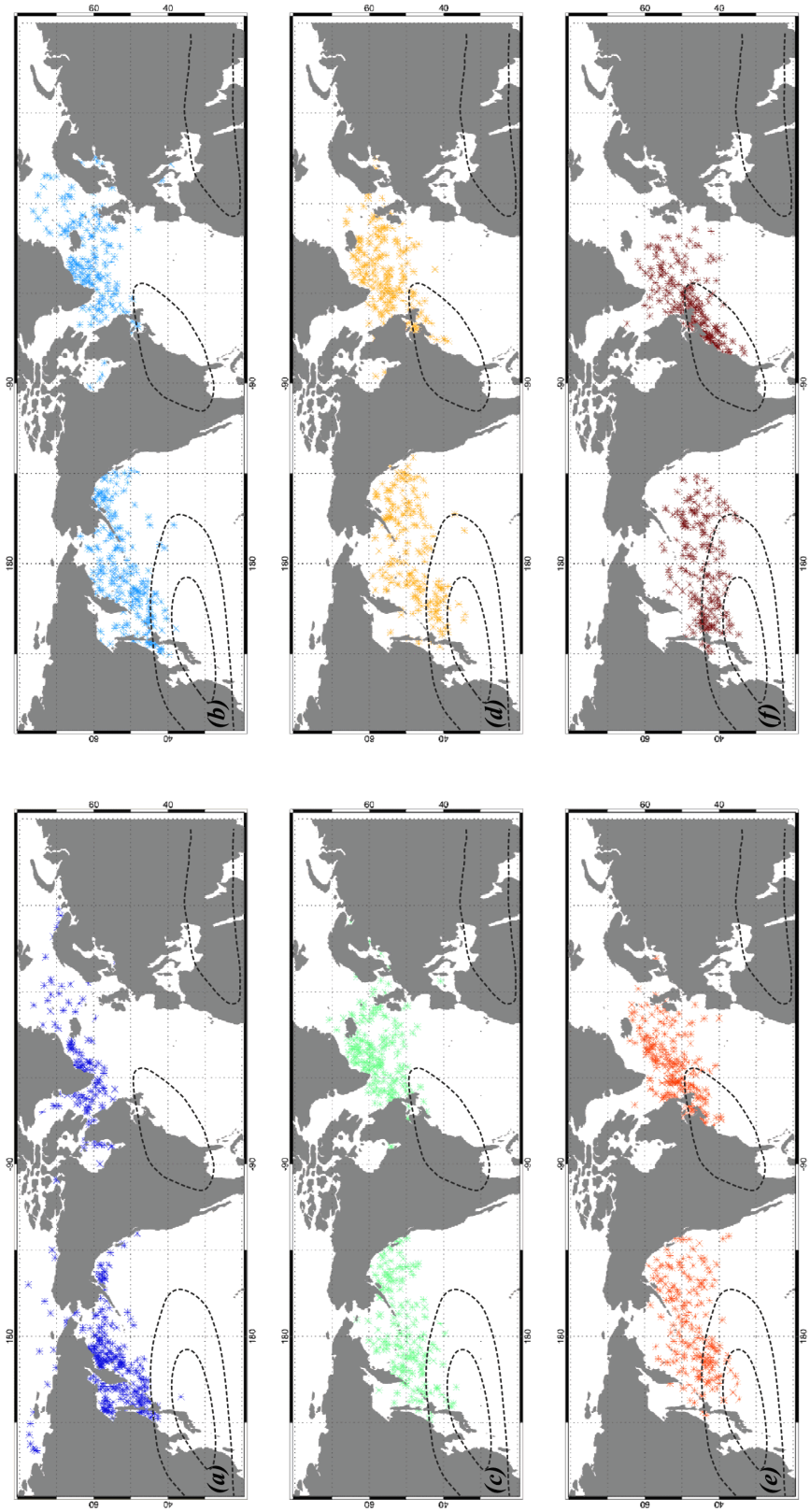

FIGURE 3.3: Geographic distribution of ETC centers that are occluded in (a) Bin I, (b) Bin II, (c) Bin III, (d) Bin IV, (e) Bin V, and (f) Bin VI as identified in Fig. 3.2. Dashed lines are the DJF average 30 and 50 m/s isotachs at 300 hPa from 2006-2017 from the MERRA-2 dataset.

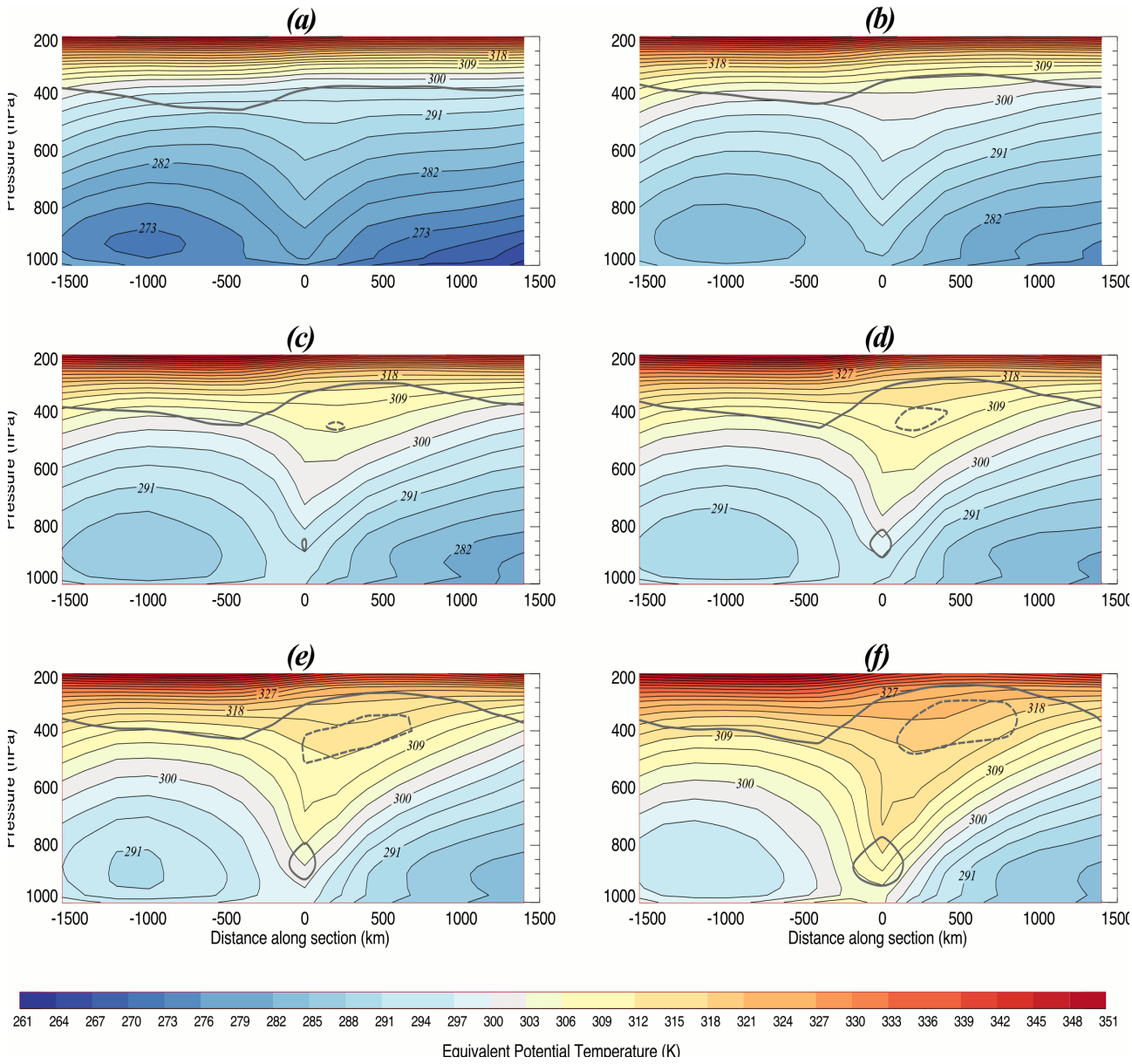

FIGURE 3.4: Composite vertical cross-sections of θ_e through the OTR in NH occlusions comprising (a) Bin I, (b) Bin II, (c) Bin III, (d) Bin IV, (e) Bin V, (f) Bin VI as identified in Fig. 3.2. Black solid lines are θ_e isentropes labeled in K and contoured and shaded (according to legend) every 3 K. Thick solid (dashed) line is the 1.5 potential vorticity units (PVU) (0.5 PVU) isertel. Thin dotted line at $x = 0$ in each cross-section identifies the intersection of the composite transect line and the adjusted thermal ridge axis. Distance along the cross-section is indicated in km; positive for poleward and negative for equatorward.

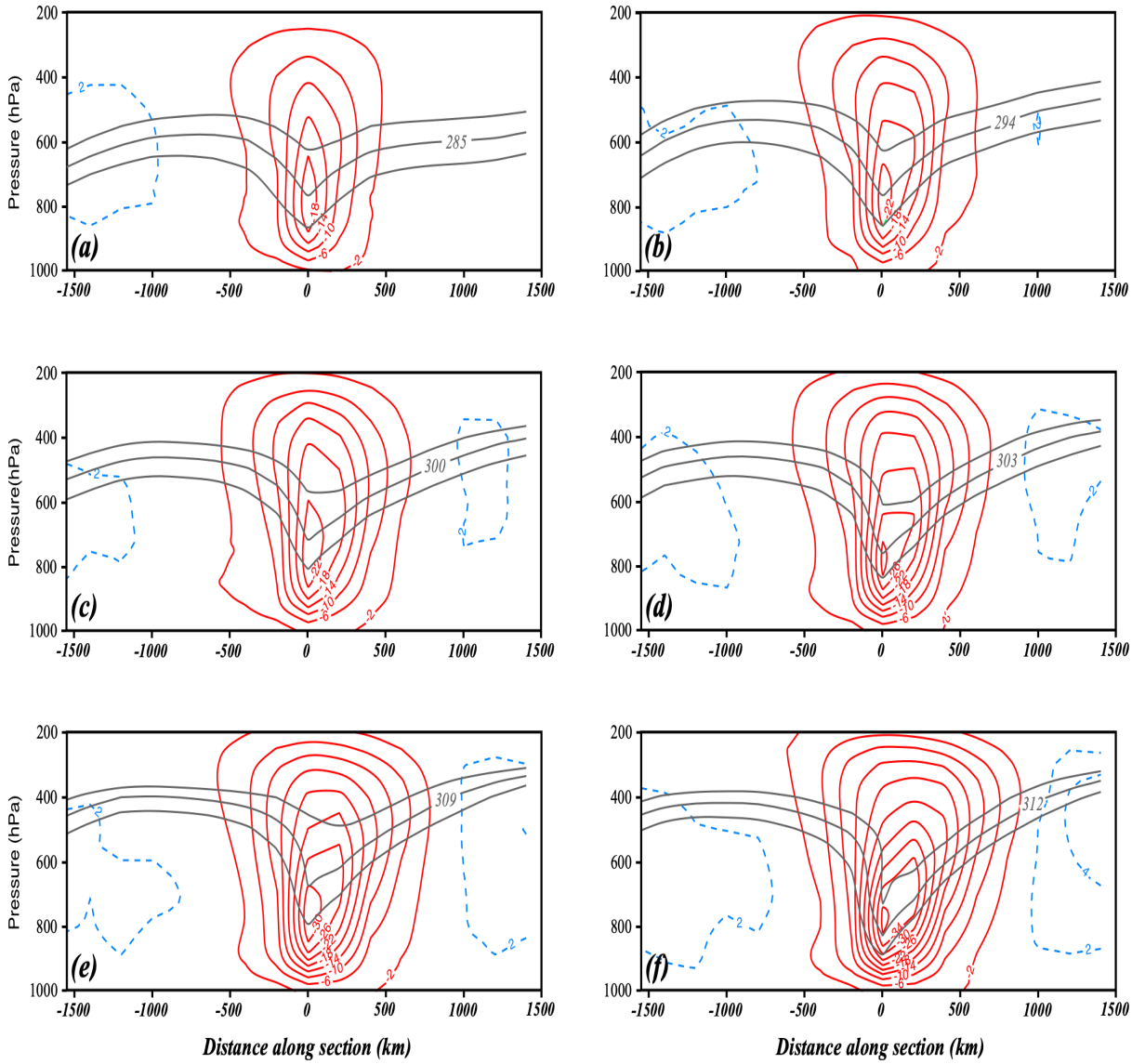

FIGURE 3.5: Composite vertical motions through the OTR in NH occlusions comprising (a) Bin I, (b) Bin II, (c) Bin III, (d) Bin IV, (e) Bin V, (f) Bin VI as identified in Fig. 3.2. Thin solid (dashed) lines are upward (downward) vertical motion labeled in units of dPa s^{-1} and contoured every 4 dPa s^{-1} starting at -2 (2) dPa s^{-1}. Thicker gray lines in each panel are three consecutive θ_e isentropes from the respective panels in Fig. 3.4, each centered on the isentrope that straddles the 0-point along the x-axis at 700 hPa.

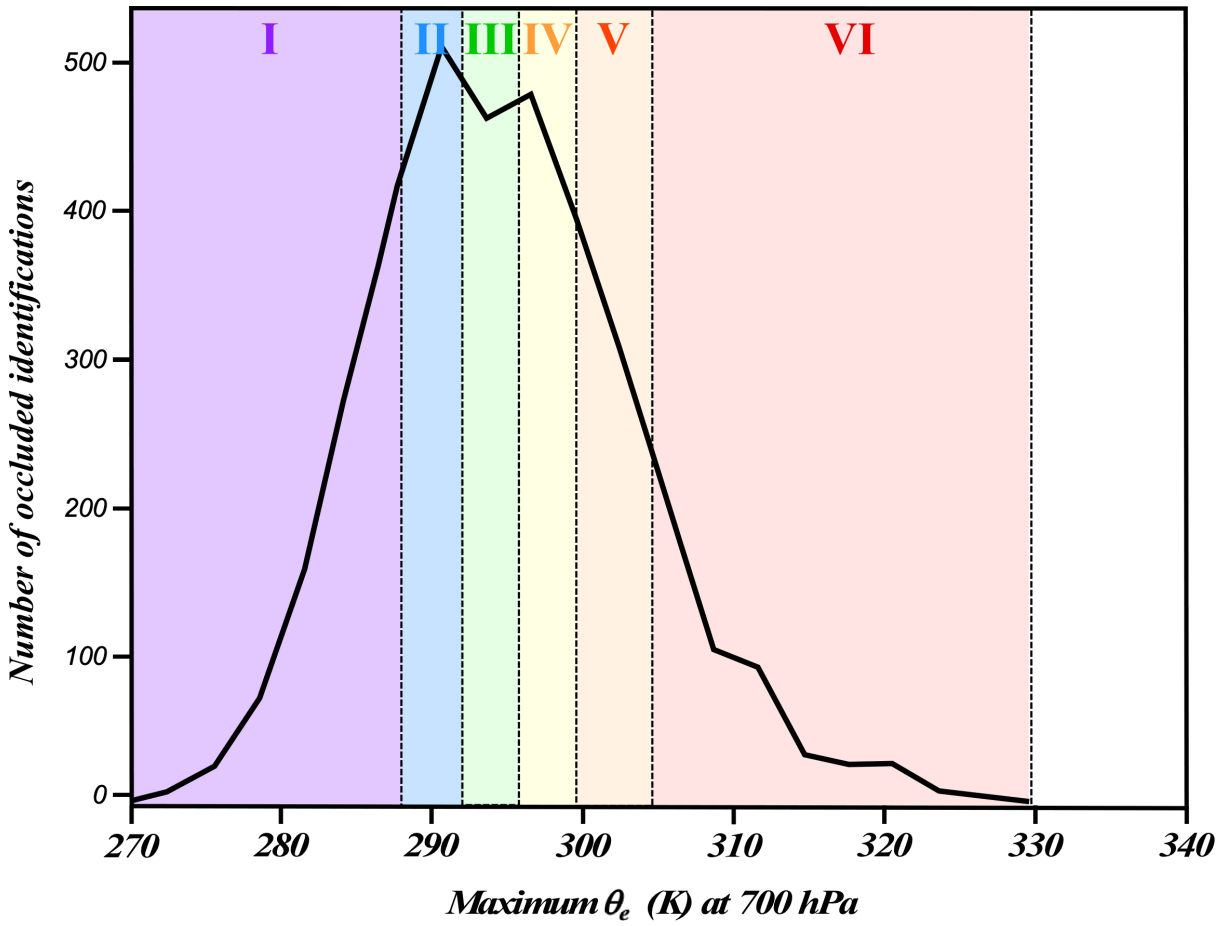

FIGURE 3.6: Cumulative distribution function of all SH wintertime occluded identifications stratified by the 700 hPa θ_e maximum along their respective thermal ridge axes. The 6 categories are referred to as Bins I-VI in the text.

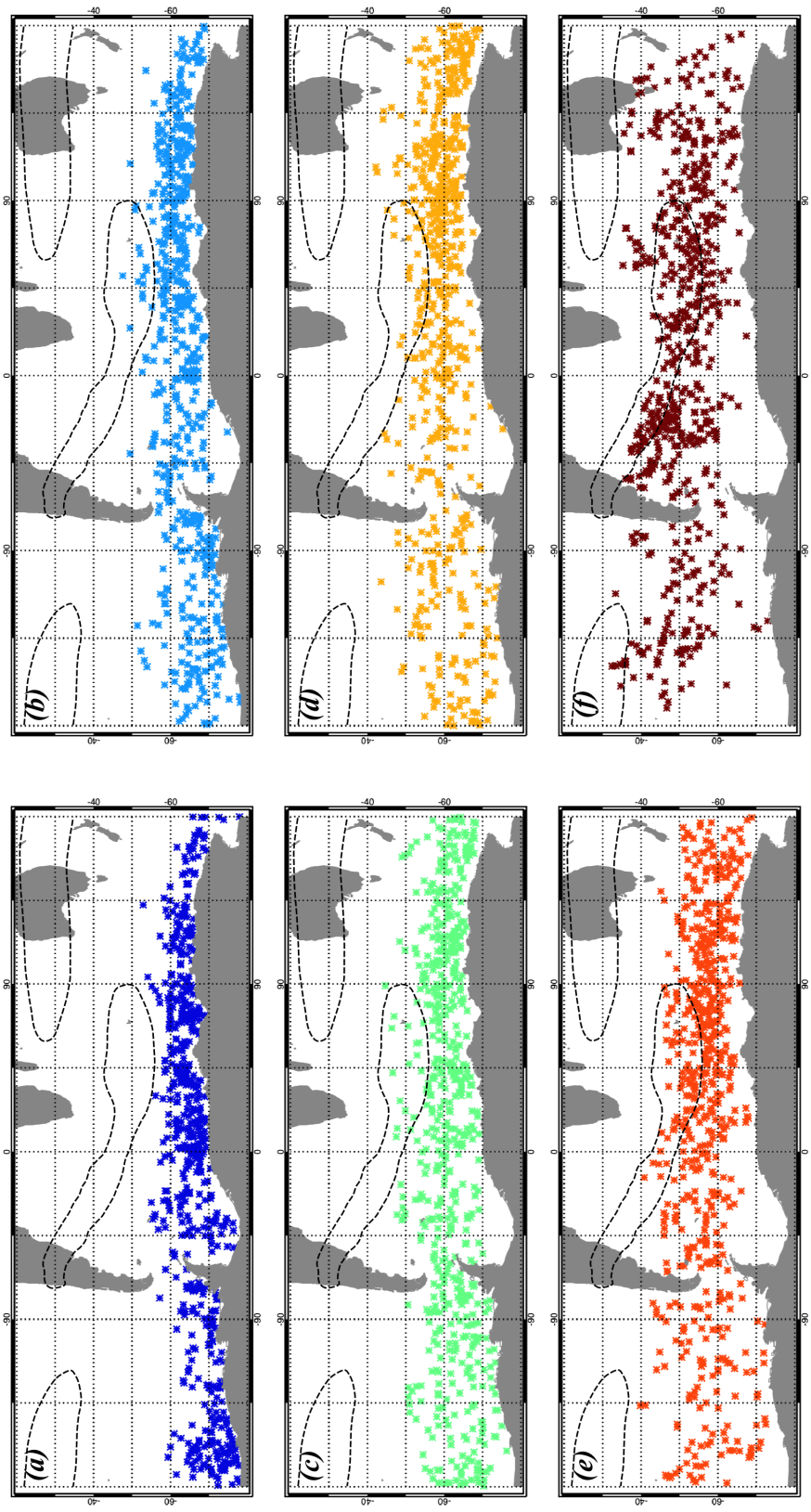

FIGURE 3.7: Geographic distribution of SH ETC centers that are occluded in (a) Bin I, (b) Bin II, (c) Bin III, (d) Bin IV, (e) Bin V, and (f) Bin VI as identified in Fig. 3.6. Dashed lines are the JJA average 30 m/s isotachs at 300 hPa from 2006-2017 from the MERRA-2 dataset.

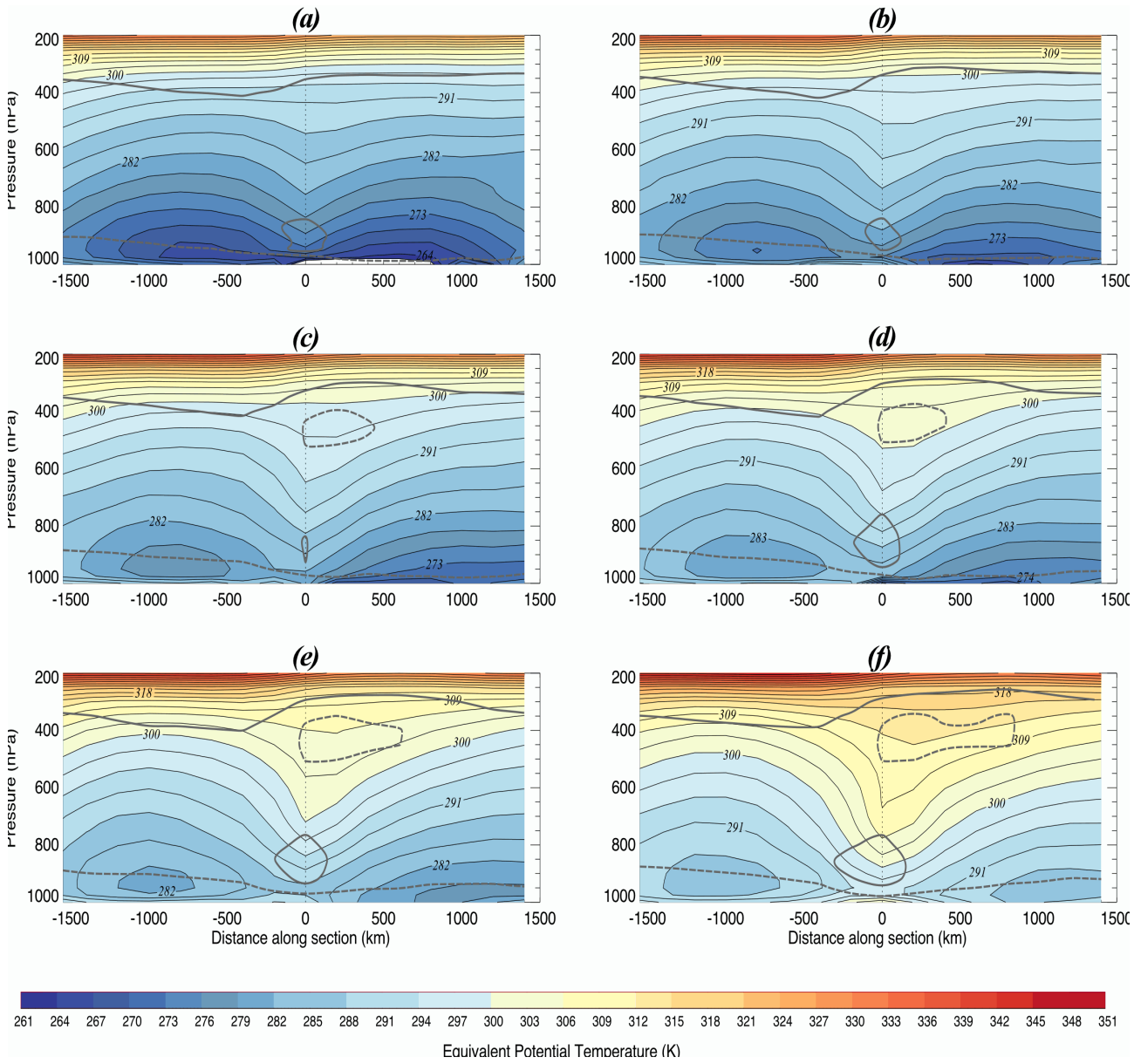

FIGURE 3.8: Composite vertical cross-sections of θ_e through the OTR in SH occlusions comprising (a) Bin I, (b) Bin II, (c) Bin III, (d) Bin IV, (e) Bin V, (f) Bin VI as identified in Fig. 3.6. Black solid lines are θ_e isentropes labeled in K and contoured and shaded (according to legend) every 3 K. Thick solid (dashed) line is the 1.5 potential vorticity units (PVU) (0.5 PVU) isertel. Thin dotted line at $x = 0$ in each cross-section identifies the intersection of the composite transect line and the adjusted thermal ridge axis. Distance along the cross-section is indicated in km; positive for poleward and negative for equatorward.

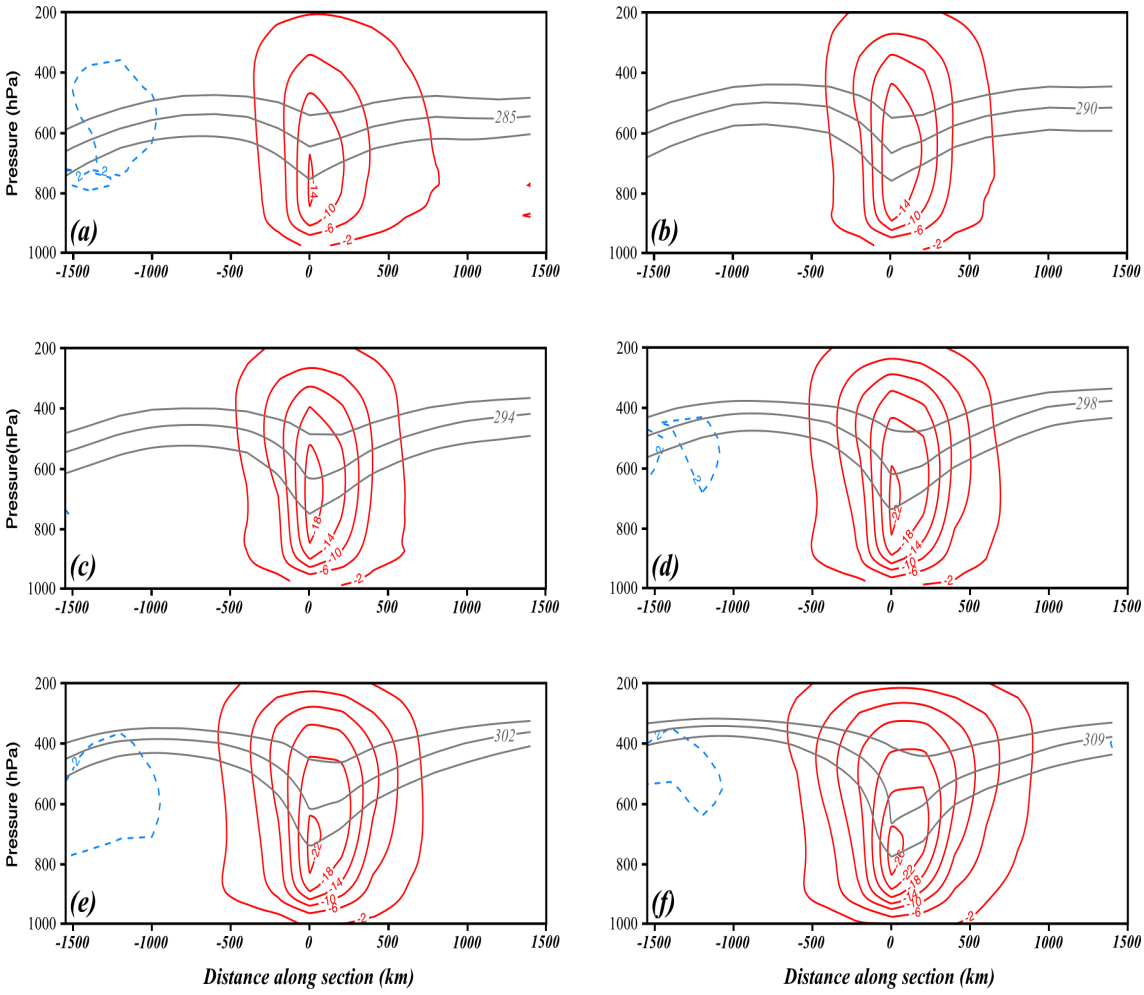

FIGURE 3.9: Composite vertical motions through the OTR in SH occlusions comprising (a) Bin I, (b) Bin II, (c) Bin III, (d) Bin IV, (e) Bin V, (f) Bin VI as identified in Fig. 3.6. Thin solid (dashed) lines are upward (downward) vertical motion labeled in units of dPa s^{-1} and contoured every 4 dPa s^{-1} starting at -2 (2) dPa s^{-1}. Thicker gray lines in each panel are three consecutive θ_e isentropes from the respective panels in Fig. 3.8, each centered on the isentrope that straddles the 0-point along the x-axis at 700 hPa.

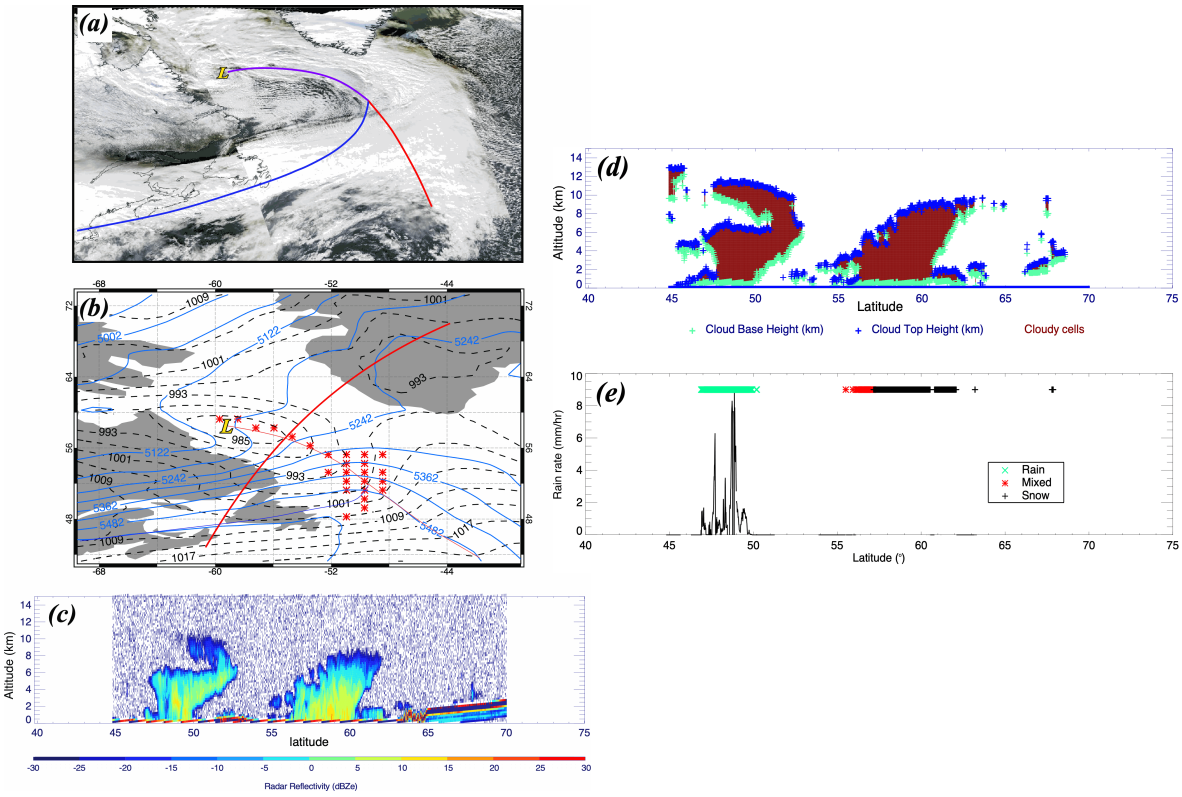

FIGURE 4.1: Occluded cyclone in the Labrador Sea on 1 December 2006, with a center at 58.25°N, 59.21°W. (a) MODIS visible imagery mosaic from EOSDIS worldview, Aqua overpass at center at 1550 UTC 1 December 2006. "L" indicates the SLP minimum position while red, blue and purple lines indicate the surface warm, cold and occluded front positions, respectively, as determined by 900 hPa vorticity and θ_e analysis using MERRA-2 data from 1200 UTC 1 December 2006. (b) SLP (dashed black) and 1000-500 hPa thickness (blue) analysis from MERRA-2 valid at 0600 UTC 1 December. SLP is labeled in hPa and contoured every 4 hPa starting at 985 hPa. Thickness is labeled in m and contoured every 60m starting at 4942m. Red line marks the CloudSat-CALIPSO orbit path through the OTR at 0500 UTC 1 December. (c) CloudSat reflectivity transect along the orbit between 45°N and 70°N. (d) 2B-GEOPROF-LIDAR derived cloud mask (maroon for cloudy), between the cloud base (green) and cloud top heights (blue) from the same orbit path. (e) Along-orbit precipitation-type identifications according to the legend. Solid black line shows rain rates where a retrieval was available.

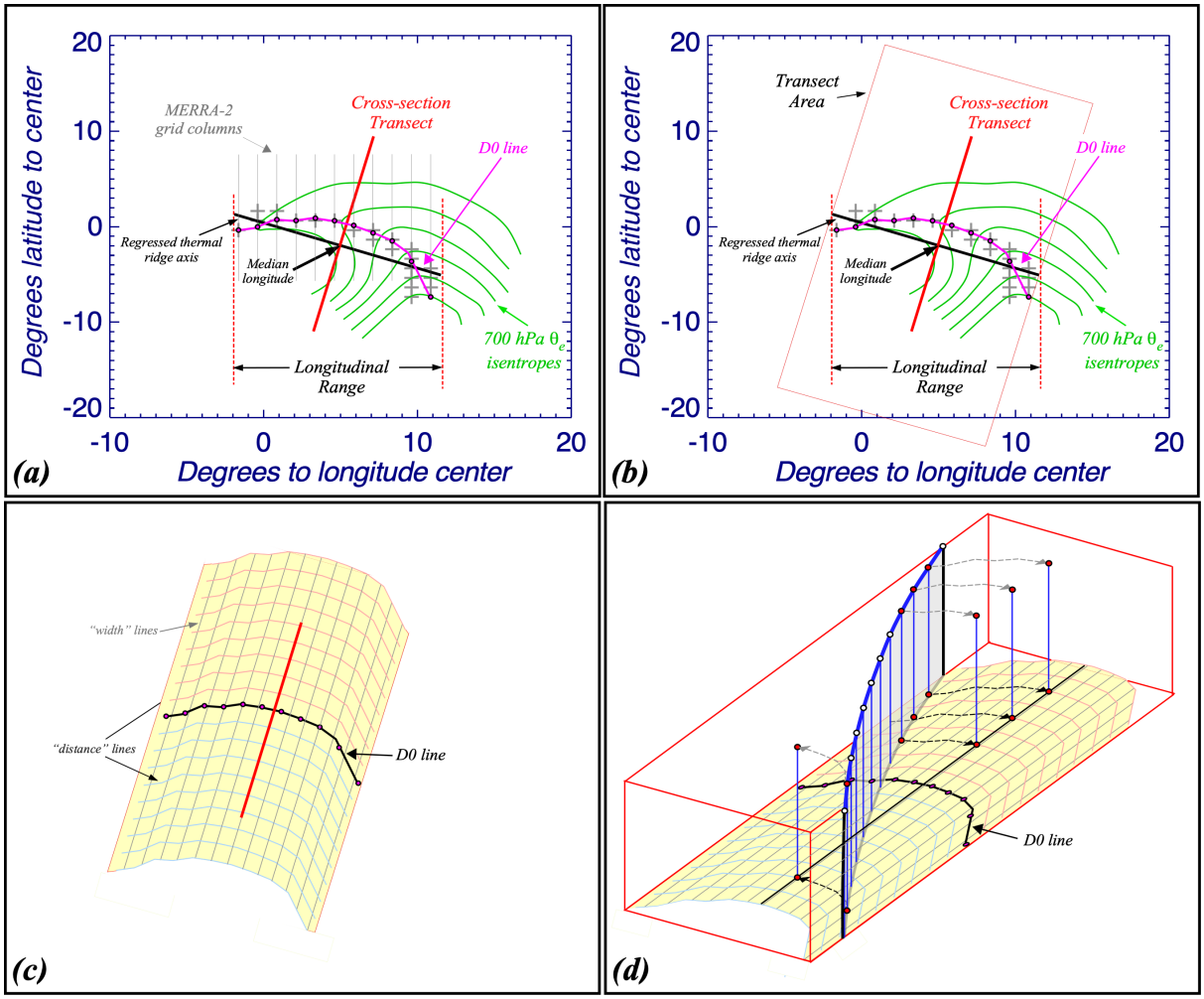

FIGURE 4.2: Illustration of the automated method to estimate the distance of each CloudSat profile along the orbit to the OTR. The OTR shown that which is displayed in Fig. **??** for an identification on 06 UTC on 1 December 2006. (a) As in Fig. 2.4, but with the adjusted D0 line (pink curve) depicting the 700 hPa θ_e ridge axis. Gray lines show the MERRA-2 grid columns at each grid point. (b) As in 4.2a but with the "transect area" outlined in red. (c) Grid created with "distance" lines parallel to the D0 line (solid black) corresponding to 100 km increments and colors representing either side of the ridge (blue-cold frontal side; red -warm frontal side). (d) as (c) with the vertical CloudSat transect across the "transect area", with the dashed line showing the projection of each profile onto the transect line.

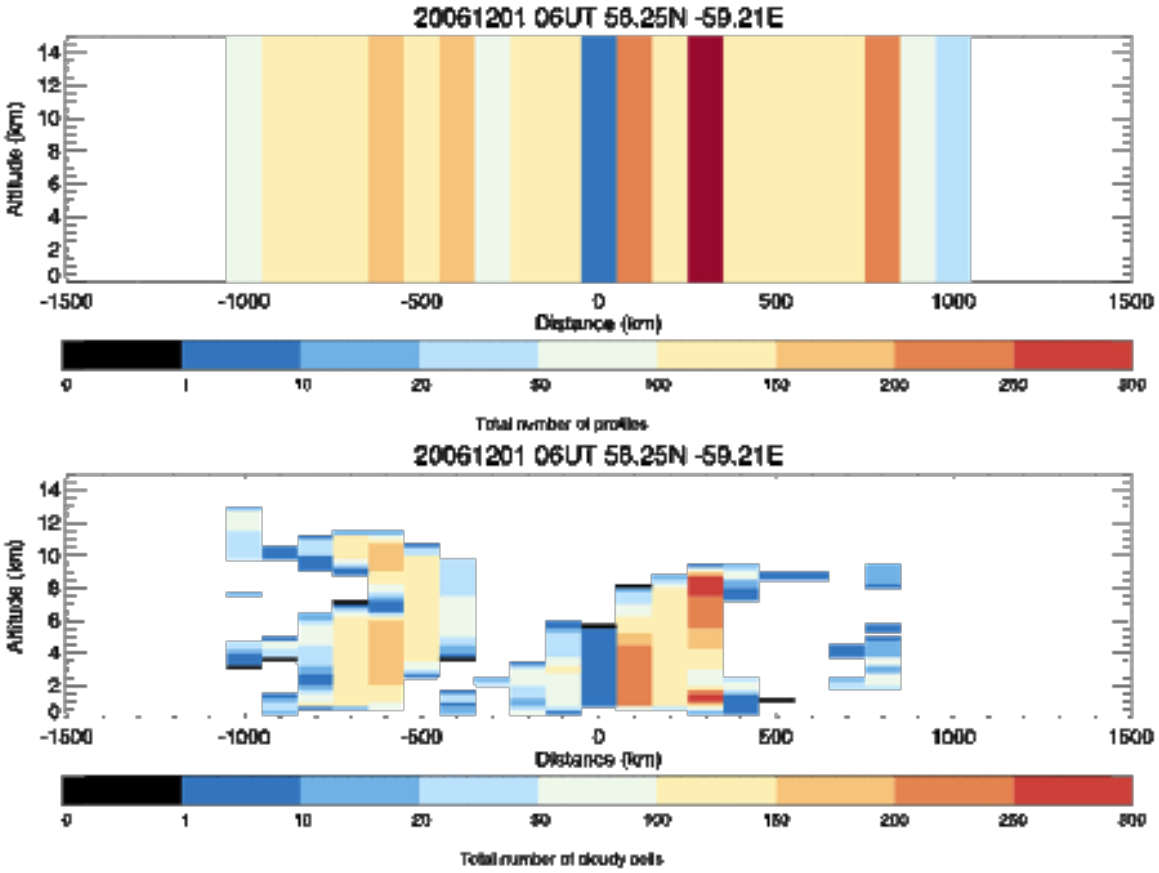

FIGURE 4.3: Illustration of individual steps of cloud compositing method. (a) Histogram showing the distance of profiles from the OTR with 100 km wide bins for the identification at 06 UTC on 1 December 2006. (b) Accumulated number of "cloudy" cells per 100 km distance bin and 250 m thick "altitude bin" (see text) at same analysis time as in (a).

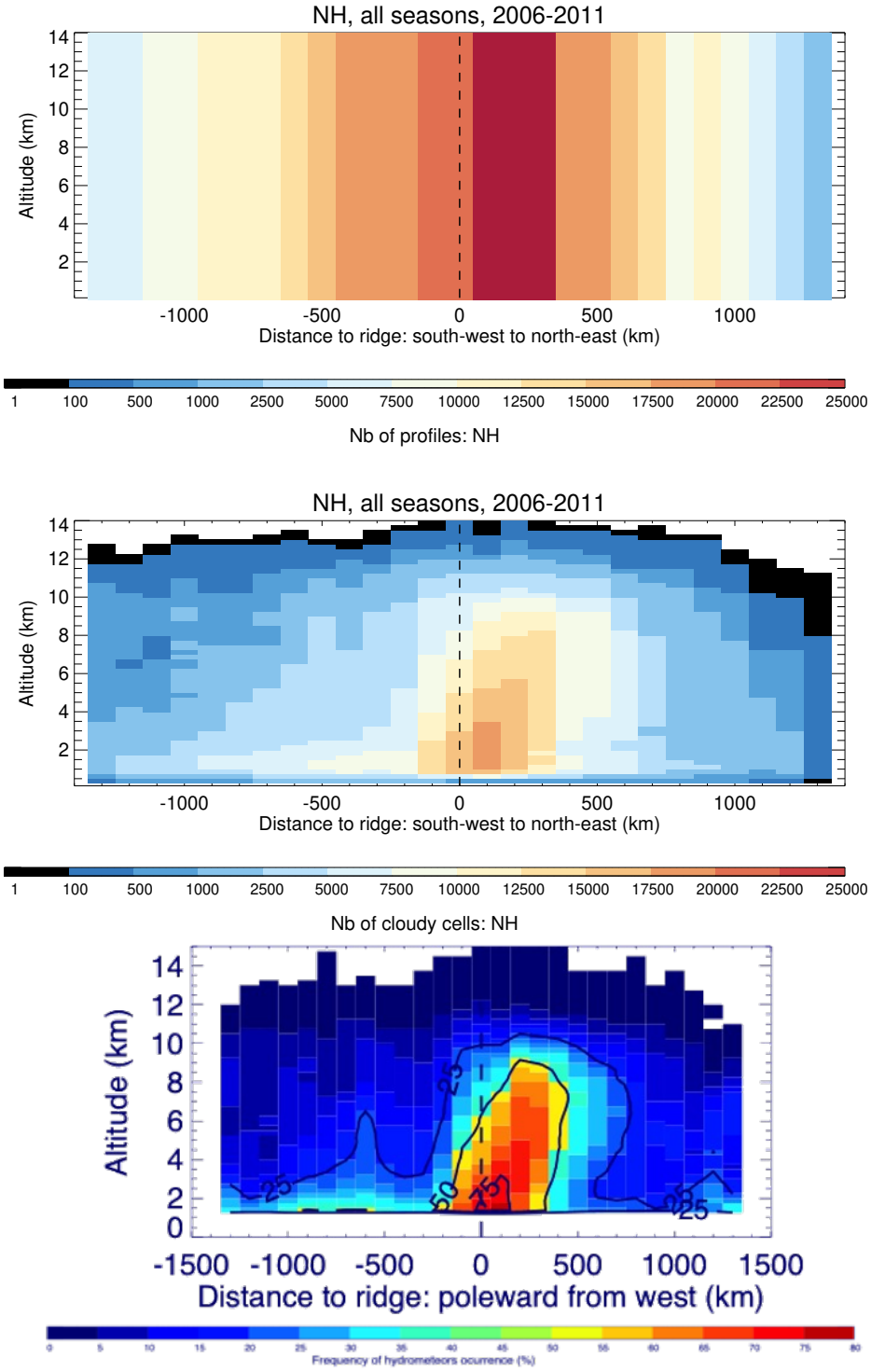

FIGURE 4.4: (a) Composite histogram showing the distance of all CloudSat-CALIPSO profiles through OTRs in the NH (2006-2011) from their respective grid clusters. (b) Composite histogram showing the accumulated number of "cloudy" cells per 100 km distance bin and 250 m thick "altitude" bin for all 2B-GEOPROF-LIDAR hydrometeor masks through OTRs in the NH (2006-2011). (c) Grand composite of hydrometeor frequency across all identified OTRs in the NH (2006-2017) with <25%, <50% and <75% frequency of occurrence areas outlined in black lines.

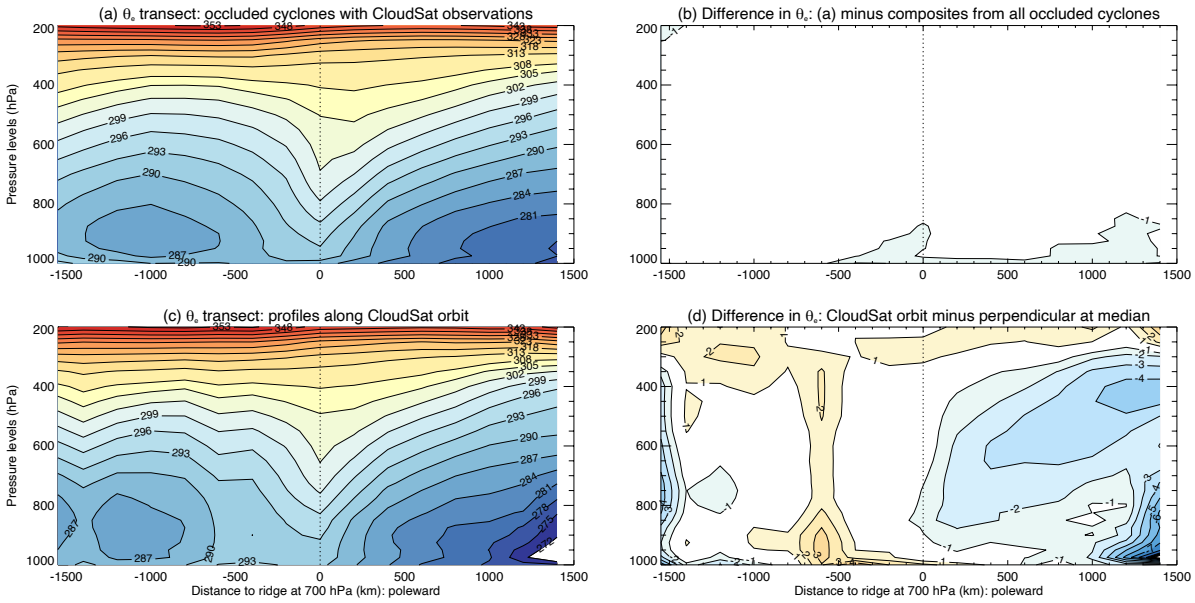

FIGURE 5.1: (a) MERRA-2 θ_e composite transect across all NH winter (DJF) occluded identifications (2006-2017) with CloudSat-CALIPSO observations using the methodology outlined in 2.4. (b) θ_e difference composite cross-section between (a) and the composite cross-section constructed with all occluded identifications in the database from 2006-2017. (c) As in (a), but using the the full 3D data volume provided by CloudSat-CALIPSO observations collapsed onto a vertical cross-section using the method illustrated in 4.2. (d)f θ_e composite difference cross-section between (a) and (c).

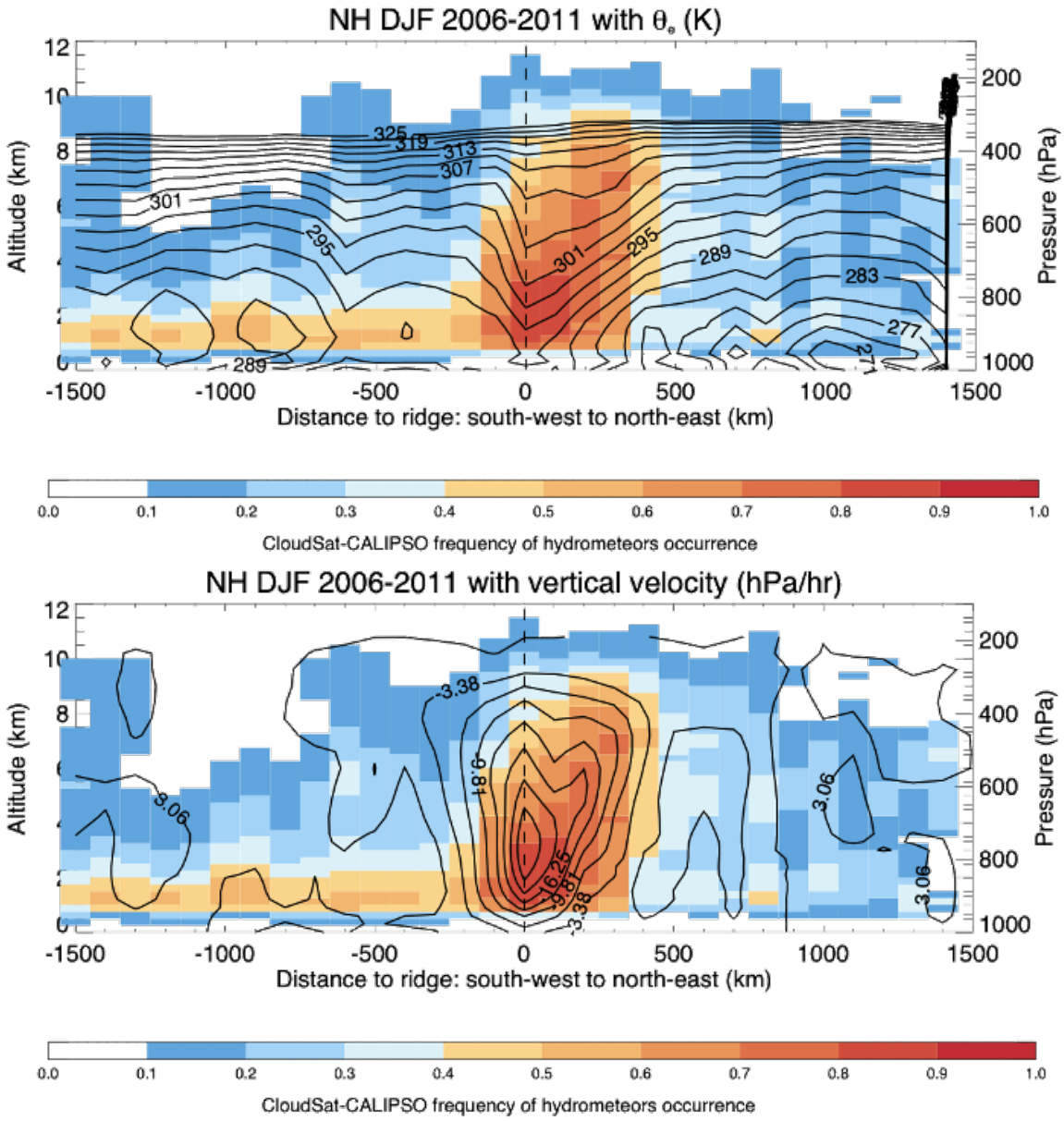

FIGURE 5.2: Composite transects of hydrometeor frequency of occurrence (shading) using CloudSat-CALIPSO observations through NH winter (DJF) occluded identifications (shaded pixels) and MERRA-2 variables from 2006-2011. (a) Composite cross-section of hydrometeor frequency of occurrence with thermodynamic structure overlaid. Black contours depict MERRA-2 θ_e (K) contoured every 3 K starting at 271 K. (b) Composite cross-section of hydrometeor frequency with kinematic structure overlaid. Black contours depict MERRA-2 column ω (hPa/hr).

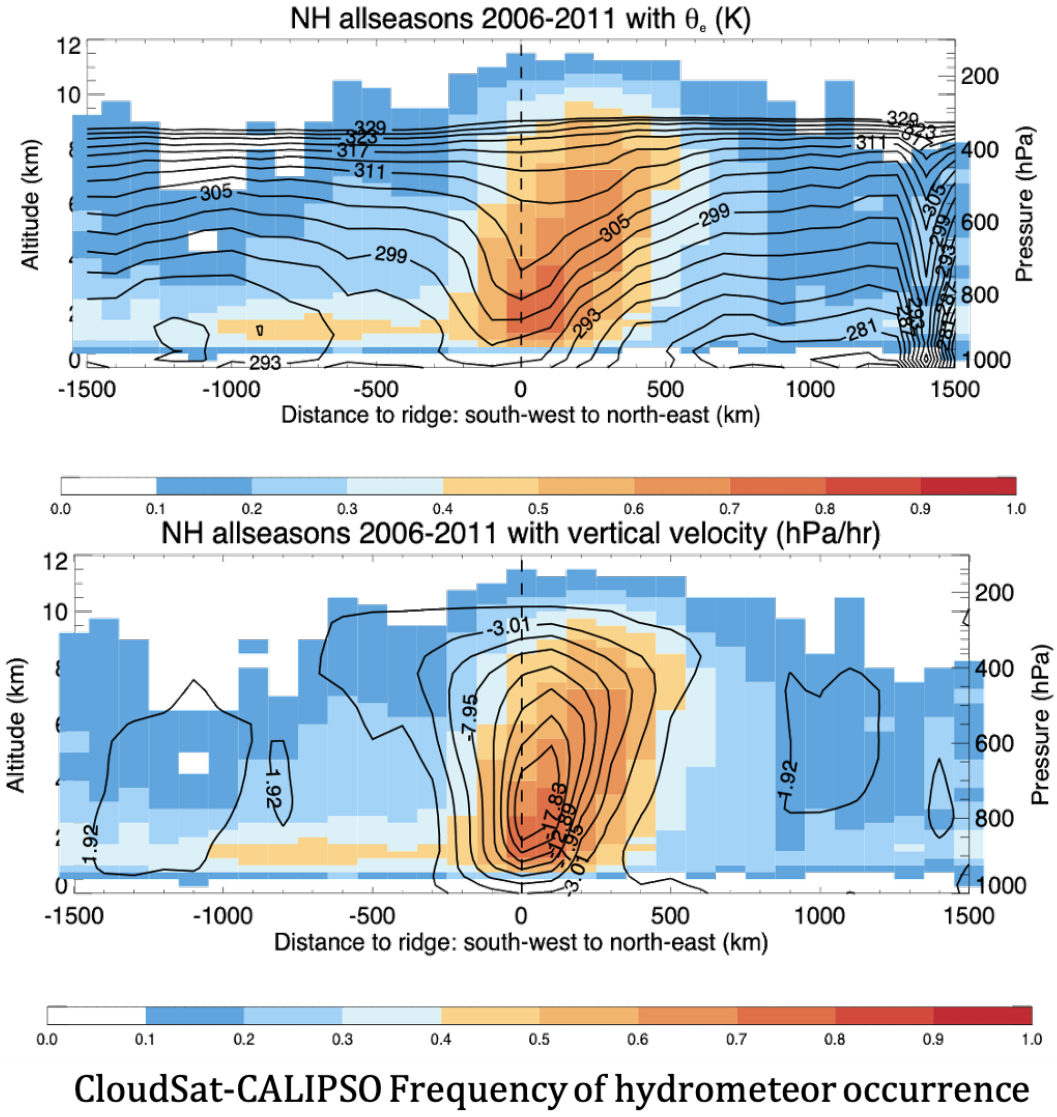

FIGURE 5.3: Composite transects of hydrometeor frequency of occurrence (shading) using CloudSat-CALIPSO observations through NH occluded identifications (shaded pixels) and MERRA-2 variables from 2006-2011. (a) Composite cross-section of hydrometeor frequency of occurrence with thermodynamic structure overlaid. Black contours depict MERRA-2 θ_e (K) contoured every 3 K starting at 278 K. (b) Composite cross-section of hydrometeor frequency with kinematic structure overlaid. Black contours depict MERRA-2 column ω in hPa/hr.

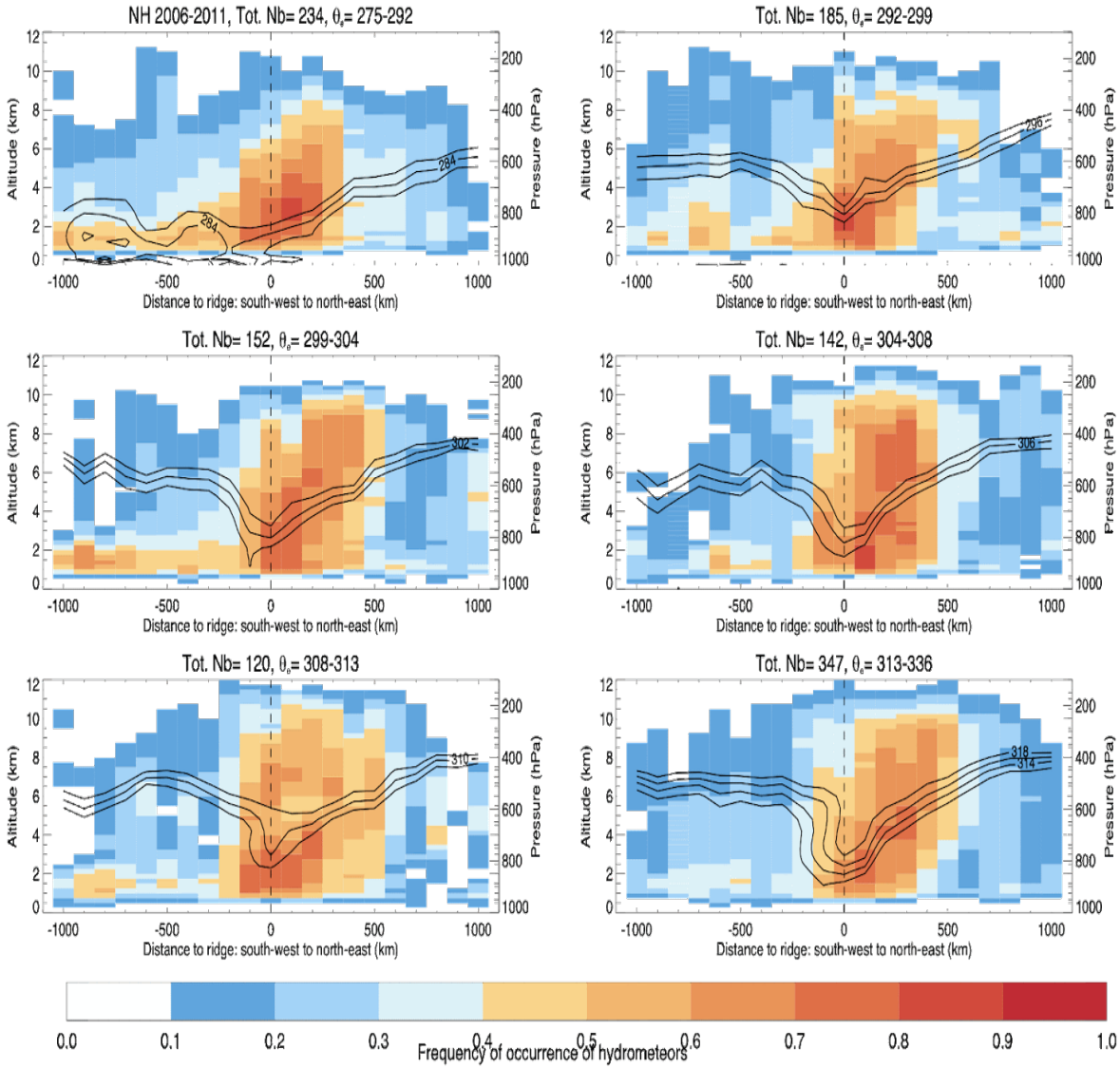

FIGURE 5.4: Composite transects of hydrometeor frequency of occurrence (shading) across all NH occluded identifications (2006-2011) comprising (a) Bin I (b) Bin II (c) Bin III (d) Bin IV (e) Bin V (f) Bin VI as identified in Fig 3.2. Black solid lines are 3 consecutive and representative isentropes from MERRA-2 data in K, contoured every 3 K.

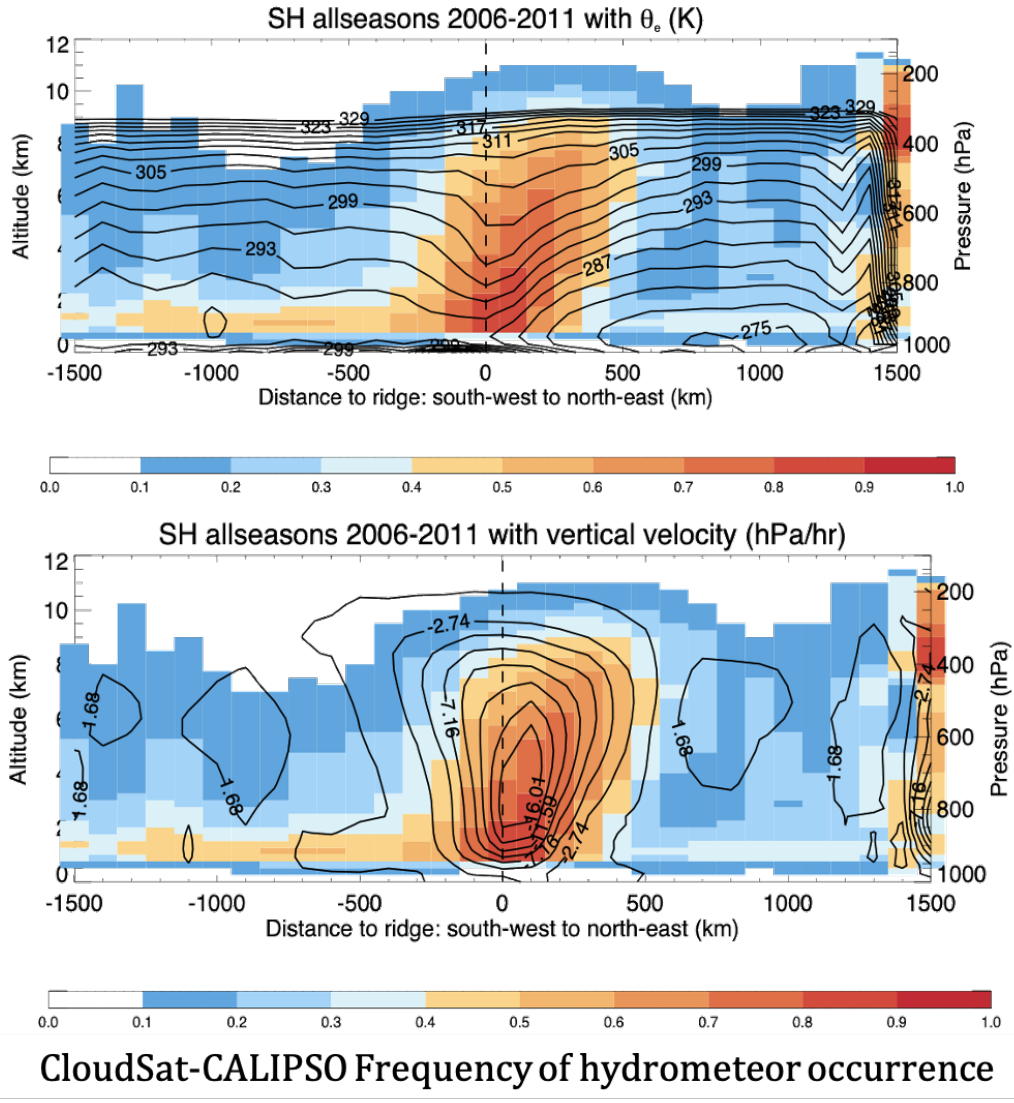

FIGURE 5.5: Composite transects of hydrometeor frequency of occurrence (shading) using CloudSat-CALIPSO observations through SH occluded identifications (shaded pixels) and MERRA-2 variables from 2006-2011. (a) Composite cross-section of hydrometeor frequency of occurrence with thermodynamic structure overlaid. Black contours depict MERRA-2 θ_e (K) contoured every 3 K starting at 275 K. (b) Composite cross-section of hydrometeor frequency with kinematic structure overlaid. Black contours depict MERRA-2 column ω in hPa/hr.

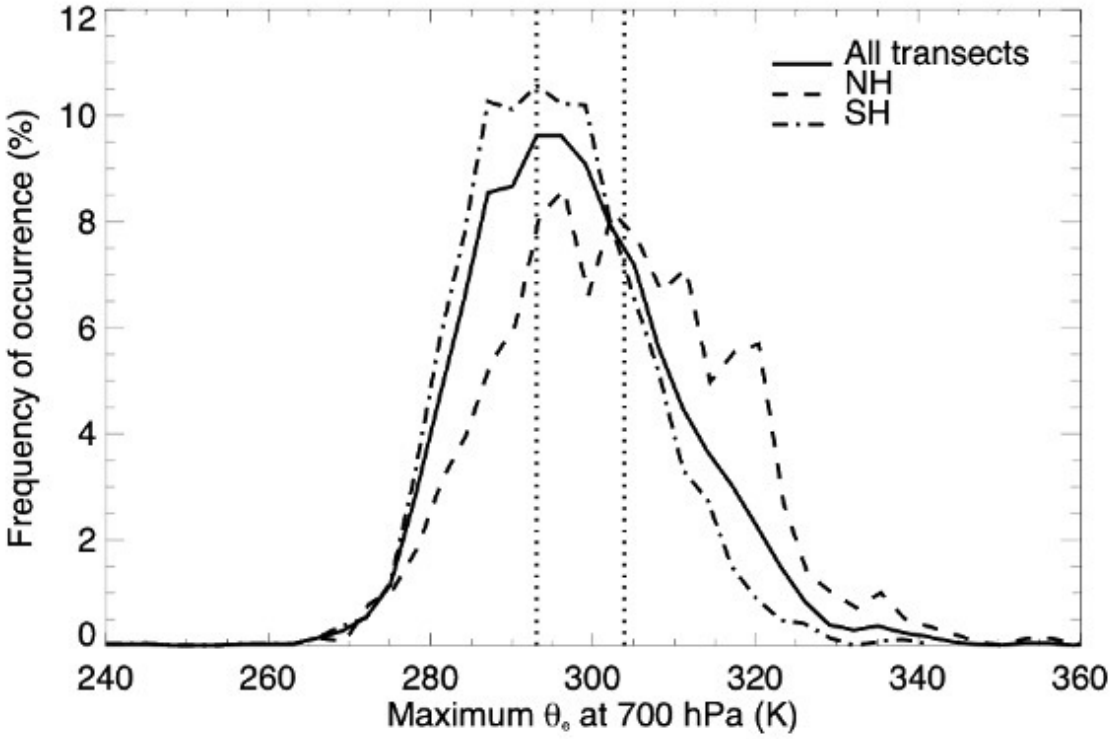

FIGURE 5.6: Cumulative distribution function of hydrometeor frequency of occurrence across all transects through OTRs in the NH (dashed line), SH (dot-dashed line) and globally (solid line) stratified by their maximum 700 hPa θ_e from 2006-2017. The whole population is divided into 3 equal subsets of maximum θ_e separated by the vertical dotted lines at 293 K and 304 K.

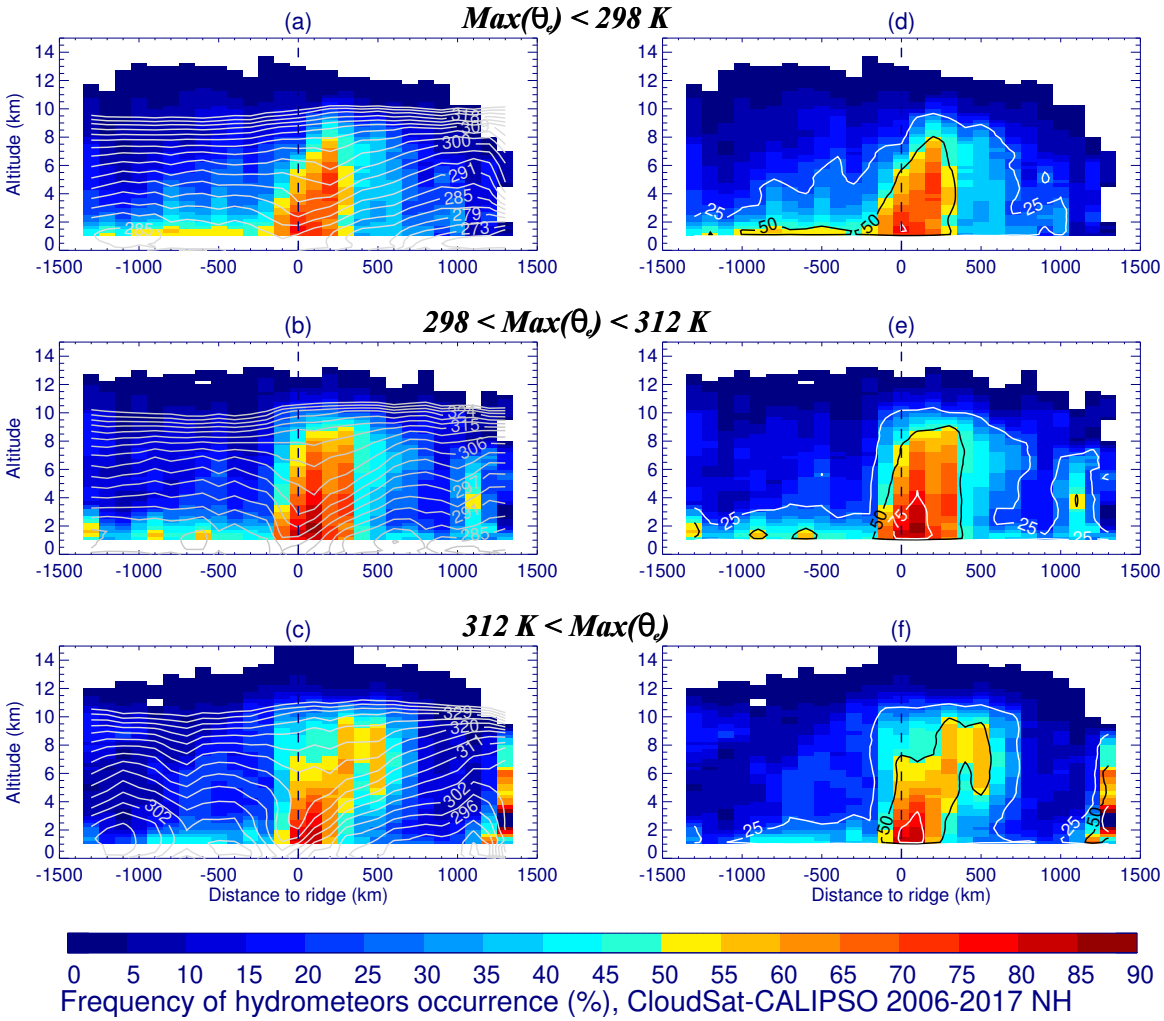

FIGURE 5.7: Composite transects of hydrometeor frequency of occurrence (shading) for all NH occluded identifications (2006-2017) with a (a) 700 hPa maximum θ_e < 298 K, (b) 298 K < 700 hPa maximum θ_e < 312 K and (c) 700 hPa maximum θ_e ¿ 312 K. Grey lines in (a-c) depict MERRA-2 θ_e composited from the cases in those respective bins. Gray lines in (d-f) outline areas with <25%, <50% and <75% frequency of hydrometeor occurrence.

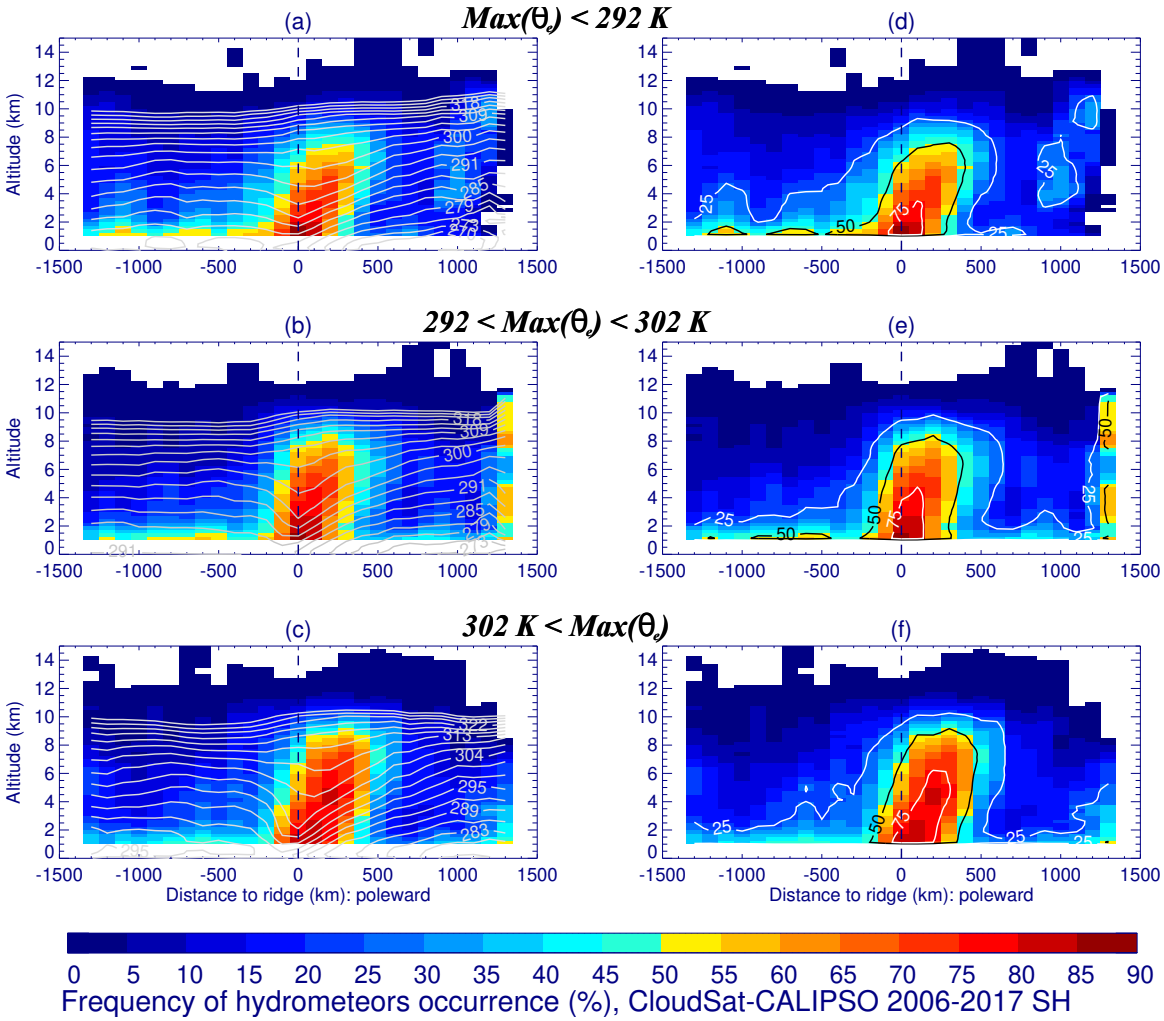

FIGURE 5.8: Composite transects of hydrometeor frequency of occurrence (shading) for all SH occluded identifications (2006-2017) with a (a) 700 hPa maximum θ_e < 291 K, (b) 291 K < 700 hPa maximum θ_e < 301 K and (c) 700 hPa maximum θ_e > 301 K. Grey lines in (a-c) depict MERRA-2 θ_e composited from the cases in those respective bins. Gray lines in (d-f) outline areas with <25%, <50% and <75% frequency of hydrometeor occurrence.

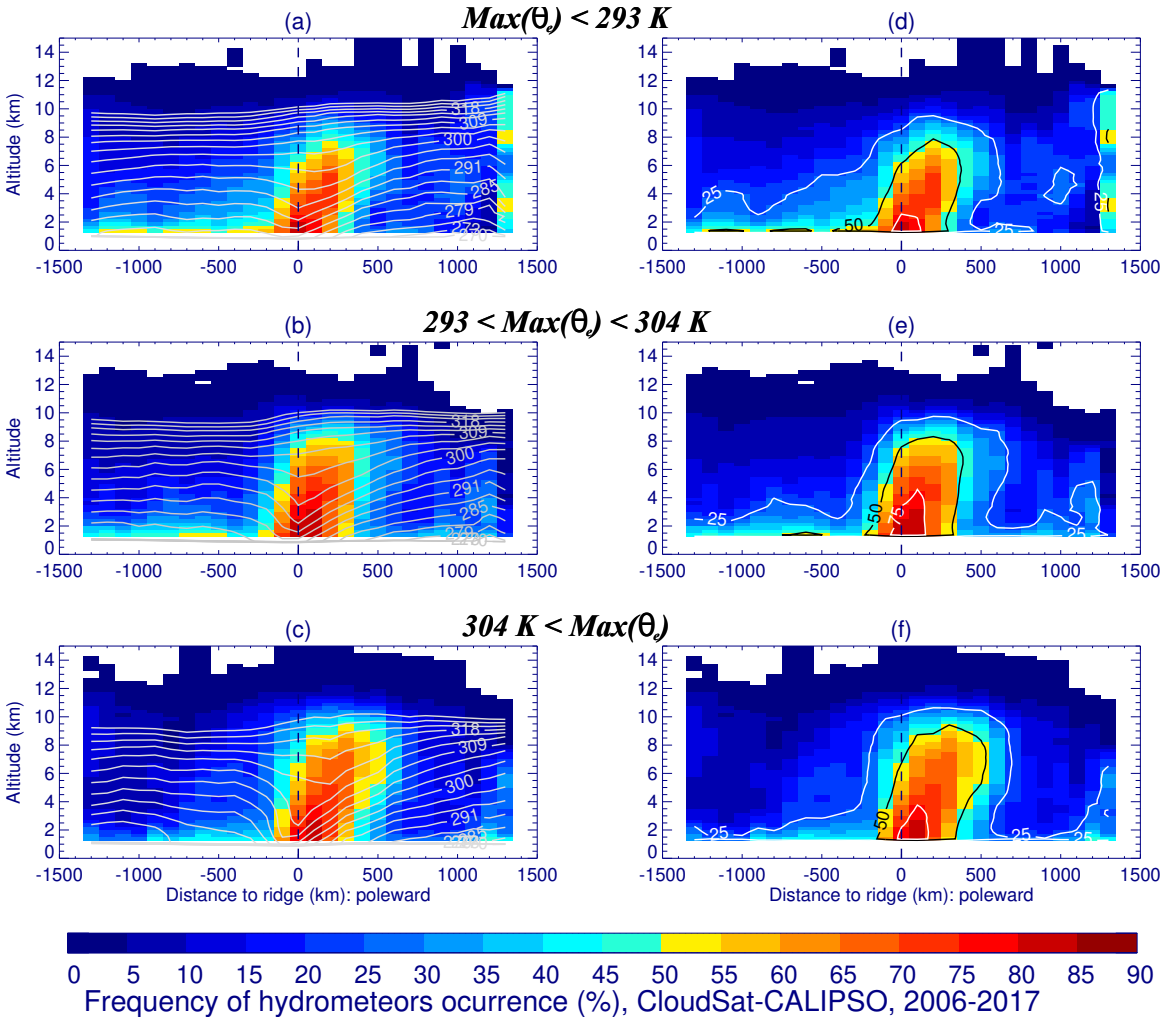

FIGURE 5.9: Composite transects of hydrometeor frequency of occurrence (shading) for all OTRs identified globally (2006-2017) with a (a) 700 hPa maximum θ_e < 293 K, (b) 293 K < 700 hPa maximum θ_e > 304 K and (c) 700 hPa maximum θ_e < 304 K. Grey lines in (a-c) depict MERRA-2 θ_e composited from the cases in those respective bins. Gray lines in (d-f) outline areas with < 25%, < 50% and < 75% frequency of hydrometeor occurrence.

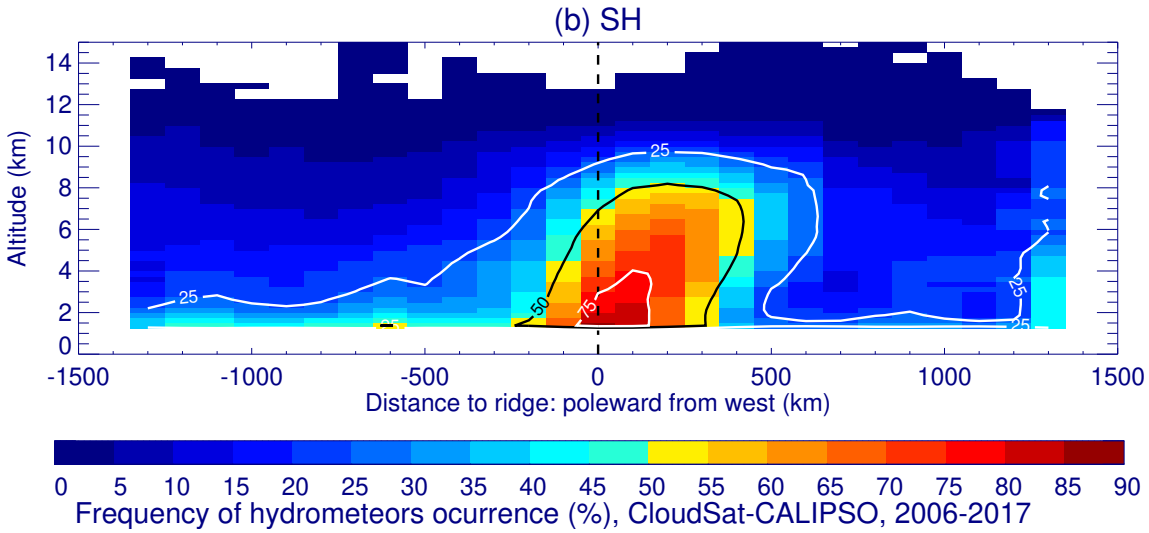

FIGURE 5.10: As in Fig. 4.4c, but for all SH occluded identifications throughout 2006-2017.

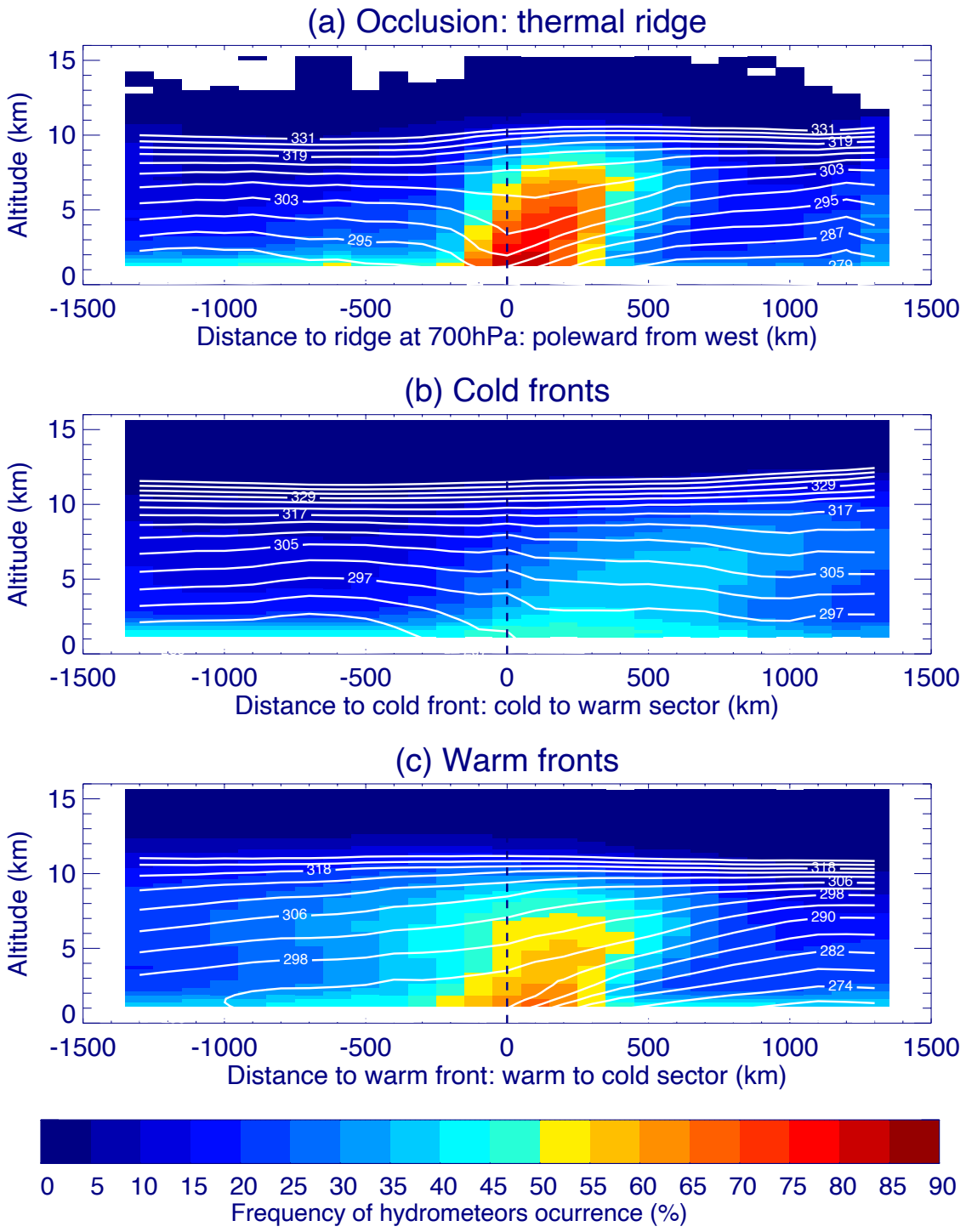

FIGURE 5.11: Composite transects of hydrometeor frequency of occurrence (shading) as obtained for all seasons globally from 2006-2017, across (a) OTRs, (b) cold fronts, and (c) warm fronts.